VORTEX DYNAMICS IN CARDIOVASCULAR FLOWS

A Dissertation

by

HOSSEIN ASADI

Submitted to the Graduate and Professional School of
Texas A&M University
in partial fulfillment of the requirements for the degree of

DOCTOR OF PHILOSOPHY

Chair of Committee,	Iman Borazjani
Committee Members,	J. N. Reddy
	Dorrin Jarrahbashi
	John C. Criscione
Head of Department,	Guillermo Aguilar

May 2022

Major Subject: Mechanical engineering

ABSTRACT

The vortex dynamics in cardiovascular flows play an important role in imposing flow features and forces acting on blood cells. Proper modeling and analysis of vortex dynamics in cardiovascular flows can shed light on the underlying reasons for various cardiovascular diseases. Numerical simulations of cardiovascular flows are challenging because they involve complex geometries with contacting deformable bodies undergoing high deformations and require fluid-structure interaction (FSI) for realistic results. In this work, a numerical framework is developed to study vortex dynamics of cardiovascular flows with FSI such as artificial heart valves. It consists of a rotation-free, high-deformation, thin shell finite element (FE) framework based on Loop's subdivision surfaces. In order to model the response of bio-prosthetic heart valves (BHVs), a nonlinear and anisotropic material model is implemented that accounts for membrane and bending responses with a Fung-elastic model. A novel physic-based contact model is incorporated into the framework to prevent the inter-leaflet penetration of the BHV leaflets during the closing phase. A series of benchmark problems are performed to validate and verify the thin shell elements, the material model, and the contact modeling, separately. The FE framework is then coupled with overset curvilinear immersed boundary (overset-CURVIB) framework using FSI with under-relaxation and Aitkin acceleration technique. The FSI FE-CURVIB framework is validated against experimental results of an inverted flapping flag using large eddy simulation (LES) modeling. Before the investigation of the effects of different heart valves, in a simplified setup, the vortex dynamics and propagation of periodically generated vortex rings are studied. A scaling law based on cycle-averaged Reynolds number and non-dimensional period is proposed for the propagation of vortex rings to predict their location. To test the findings in cardiovascular flows, the vortex dynamics of two main categories of heart valves, i.e., bi-leaflet mechanical heart valve (BMHV) and BHV, are studied. First, the vortex dynamics of BMHVs and their effects on the platelet activation are studied in a left ventricle-aorta configuration, incorporating a beating left ventricle (LV). In this study, three different implantation orientations are compared for multiple cycles. The results show symmetrical leaflet kinematics

during the opening, while significant cycle-to-cycle variations are observed for the closing phase, which are due to the presence of small-scale vortical structures. The results show that the proposed scaling law with good precision can predict the location of the mitral vortex ring in the LV before the vortex breakdown. Furthermore, our results show that the valve orientation does not have a significant effect on the distribution of viscous shear stress and total platelet activation in the ascending aorta. Then, the kinematics, vortex dynamics, and platelet activation of a BHV are investigated. The comparison of the BHV leaflet kinematics of FSI and dynamic simulations shows significant differences in the opening phase of valves. The FSI results show a displacement starting from the belly and developing to the free edges due to the hydrodynamic pressure distribution, in stark contrast to dynamic results; however, the closing phase is relatively similar. The vortical structures in the straight aorta with the implanted BHV are visualized and studied for the complete cycle. The propagation of the complex three-lobed vortex ring during the opening phase was predicted using the scaling law with an acceptable margin. In addition to the previously observed vortex rings during the opening, two vortex rings during the closing phase are detected for the first time, due to the kinematics of the leaflets. In conclusion, while the results of different heart valves show high complexities in both structural and flow features, they illustrate similar physics/scaling in terms of the location and interaction of the vortical structures.

DEDICATION

To my parents and my sister for their support and affection.

ACKNOWLEDGMENTS

I would like to express my sincere gratitude to my Ph.D. advisor, Professor Iman Borazjani for his excellent guidance, support, and patience through this endeavor, without whom this work would have not been possible. I am grateful to the members of my doctoral committee, Professors J.N. Reddy, Dorrin Jarrahbashi, and John C. Criscione whose comments have greatly improved this work.

I owe a great deal of gratitude to my parents for devoting their lives to me, to my sister for her kind support. Their love and encouragement had a significant influence on my life.

This work was supported by American Heart Association (AHA) grant 13SDG17220022, National Institute of Health (NIH) grant R03EB014860, National Science Foundation (NSF) award CBET 1453982, and computational resources were provided by Texas A&M High-Performance Research Computing Center (HPRC).

CONTRIBUTORS AND FUNDING SOURCES

Contributors

This work was supported by a thesis committee consisting of Professors Iman Borazjani, J.N. Reddy, and Dorrin Jarrahbashi of the J. Mike Walker '66 Department of Mechanical Engineering and Professor John C. Criscione of the Department of Biomedical Engineering.

Funding Sources

This work was supported by American Heart Association (AHA) grant 13SDG17220022, National Institute of Health (NIH) grant R03EB014860, National Science Foundation (NSF) award CBET 1453982 and computational resources were provided by Texas A&M High-Performance Research Computing Center (HPRC).

NOMENCLATURE

CVD	Cardiovascular diseases
LV	Left ventricle
CURVIB	Curvilinear immersed boundary
GMRES	Generalized minimal residual
FSI	Fluid-structure interaction
SC	Strong coupling
FEM	Finite element method
BHV	Bio-prosthetic heart valve
MHV	Mechanical heart valve
LES	Large eddy simulation
BMHV	Bi-leaflet mechanical heart valve
PDF	Probability density function
MIPE	Major in-plane Green-Lagrange strain
FE	Formation excluded
FI	Formation included
TMHV	Tilting disk mechanical heart valve
WSS	Wall shear stress
LC	Left coronary cusp
RC	Right coronary cusp
NC	Non-coronary cusp
ODE	Ordinary differential equations
HV	Heart valve

DCR	Decomposition contact response
CFD	Computational fluid dynamics
SM	Structural mechanics
ALE	Arbitrary Lagrangian Eulerian
IBM	Immersed boundary method

TABLE OF CONTENTS

Page

LIST OF FIGURES

FIGURE Page

LIST OF TABLES

TABLE Page

1. INTRODUCTION AND MOTIVATIONS

Cardiovascular system is responsible for delivering nutrients and oxygen to the cells by circulating blood flow throughout the body. Any diseases related to the heart or blood vessels are categorized as cardiovascular diseases (CVD) [11], which is the main cause of death in the US [12]. One of the main features of any cardiovascular flow is the creation and propagation of vortex rings, which are vortical flow structures created when the upcoming flow rolls over into expansion areas such as the left ventricle (LV), sinuses, and aneurysms. Vortex ring formation plays an important role in the health and performance of the heart. Healthy LV moves in tandem with expanding vortex ring to accommodate vortex ring formation [13]. The major aspects of cardiac function can be reflected uniquely in the optimization of vortex formation in the blood flow during early diastole [14]. Vortex formation can be affected by the movement of the heart valves, which are located between heart chambers and major blood vessels to ensure unidirectional blood flow. Consequently, the replacement of defective heart valves with artificial ones due to diseases with more than 100,000 cases annually in the US [15] can significantly affect the flow and the vortex propagation. This can change the distribution of vortical structures in the vicinity of the valve, which can alter the hemodynamic forces acting on the blood cells and the leaflets of the valve. The changes in forces applied on the blood cells can lead to thrombus generation, i.e., blood clotting, which can cause fatal strokes. On the other hand, the alteration of the hemodynamic forces acting on the leaflets of the valves can lead to unwanted changes in leaflet kinematics, which can potentially cause regurgitation, i.e., backward flow into the heart, increasing heart workload. Therefore, numerical investigation of vortex dynamics of cardiovascular flows is regarded as an important tool in improving prosthetic heart valves performance noninvasively.

1.1 Numerical methods in cardiovascular flows

In order to study the flow patterns and performance of the artificial heart valves several in-vitro and in-vivo investigations have been performed [16, 17, 18, 19]. Due to the lack of spatial/temporal

resolution of measurement techniques utilized, these studies were not capable of capturing the 3D complicated flow features involved with artificial heart valves. The 3D feature of heart valve simulations is of great importance since by resolving the 3D flows, the distribution of shear stress can be computed. Shear stress is the main parameter in determining the mechanical forces acting on blood cells [20], which leads to platelet activation. With the advent of new computational methods and with the rapid increase in computational capabilities of new machines, the computational fluid dynamics (CFD) [21, 22] and finite element method (FEM) [23, 24, 25] were used in the simulations of different cardiovascular flows and the deformable bodies involved. The computational methods give leverage for the scientific community to study the 3D complex flow features in more detail. Additionally, they provide the option of isolating the effects of different parameters more easily compared to the experimental approach. Consequently, numerical frameworks specifically developed for cardiovascular flows can be used as a tool for optimizing various medical devices.

Cardiovascular flows involve complex geometries [26], which mostly undergo high deformations [27]. One of the numerical approaches to handle these challenges is the arbitrary Lagrangian-Eulerian (ALE) method, which employs a conforming grid that moves with the moving boundary [28]. In this approach, the grid conforms with the shape of the domain at each time, and therefore, in the governing equations, the grid movements are considered [29, 30, 31]. In this method, the complexity of the domain and the high deformation of bodies may lead to grid skewness. There have been studies that attempted to resolve the grid smoothness problem by interpolating the previously generated meshes [32] using elliptic solvers [33] but obtaining a proper mesh is not trivial. Consequently, the ALE method is restricted to problems with relatively simple geometries, which undergo mild deformations.

Using a fixed grid is another approach for the simulation of cardiovascular flows. The cut-cell method [34], fictitious domain [35, 36], and immersed boundary method (IBM) [37, 38] are the three main categories of fixed grid approach. Among these categories IBM method has been established as a efficient and capable method [39], which can be categorized into diffuse [40, 41] and sharp interface methods [42]. In order to model the interface for the diffuse interface

method, a forcing term is added to the continuous Navier-Stokes equations [43], which creates a diffuse boundary, where the boundary conditions are not satisfied in their actual location; therefore, typically require higher grid resolution near the boundary.

To remedy the diffuse boundary problem, the sharp interface method applies a discrete forcing to the discretized Navier-Stokes equations [44]. The sharp-interface IBM is further developed by introducing a curvilinear, body-fitted grid (CURVIB) [45] and was employed to simulate the first direct numerical simulation of a bi-leaflet mechanical heart valve (BMHV) in a straight aorta [45]. Later, the CURVIB method was coupled with a fluid-structure interaction (FSI) formulation to simulate multiple, moving, rigid bodies that undergo arbitrary large deformations in complex geometry [46]. The FSI CURVIB framework was further developed by incorporating overset grids (overset-CURVIB) to efficiently handle several inter-connected geometries [47]. In order to simulate the heart valves with deformable structures, e.g., native and bio-prosthetic heart valves (BHV), a membrane FEM was coupled with the CURVIB method and used to compare the flow features of BHV and BMHV during systole [48].

In this work, a thin shell FE framework is developed, which incorporates the membrane and bending responses and is coupled with overset-CURVIB using the FSI algorithm of Borazjani [48]. This framework is enhanced with a non-linear and anisotropic material model and a novel physic-based contact model to simulate the cardiovascular flows for a BHV during a complete cardiac cycle. In chapter §2 the equations governing both fluid and structure are explained. Then, the validations and verification studies of different aspects of the implemented framework are presented in §3. In §4, the dynamics and scaling of periodic vortex rings are discussed in a simplified configuration. Then, we turn to cardiovascular flows involving replacement heart valves and investigate flow features and vortex dynamics of BMHV and BHV in §5 and §6, respectively. Finally, the summary and outlook are presented in §7. In the remaining sections of this chapter, an overview of different types of replacement heart valves is discussed. Then, the objectives and significance of this work are clarified. Finally, the state-of-the-art and novelties of the present study are addressed.

1.2 Artificial heart valves

Currently, the prevalence of mitral or aortic valvular malfunction is approximately 2.5% for the general public and 10% among the elderly population of age over 75 in the United States [49]. Surgical valve replacement is a standard practice to remedy valvular diseases for patients with low to medium risk of surgery; however, with the advent of transcatheter technologies in recent years, transcatheter valve therapies offer an alternative for patients with high risk for surgery [50]. Whether used in conventional surgery or by transcatheter therapies, the artificial heart valves can be categorized into two main types based on the leaflet material [51]: mechanical heart valve (MHV) and bio-prosthetic heart valve (BHV). These two types of valves are used in both mitral and aortic positions and have shown significant differences in terms of thrombus generation [52].

1.2.1 Mechanical heart valves

The MHVs account for 30% of implantation [53] and are more durable but more prone to thrombus generation, which can cause disabling and fatal strokes and therefore require life-long use of anticogulant drugs. The production of these valves started with the introduction of caged-ball valve (figure 1.1(a)) as the first artificial valve commercialized. It consists of three arches, a ball, and a ring. During the systole, the ventricular pressure pushes the ball against the arches, while during diastole, the ball falls back onto the ring and seals the valve. The later versions of MHV had a monoleaflet configuration, where a graphite disk is placed between two struts and is tilted from 60^o to 80^o relative to the annulus (figure 1.1(b)). The caged-ball and tilting-disk valve's production was discontinued by the emergence of bileaflet mechanical heart valves (BMHV). As shown in figure 1.1(c), BMHV consists of two semicircular leaflets that are hinged with an angel of 75^o to 90^0 to a ring. These valves are the most popular of the mechanical valves and are still considered one of the top options among the younger patients [54]. The BMHVs show lower quality relative to BHVs in term hemodynamics, which stems from the generated non-physiological flow. To address this, a new class of MHV is introduced that has triradial symmetry similar to native heart valves (figure 1.1(d)). The trileaflet valves include the durability of the MHVs and may have the superior

hemodynamic performance of a native valve [55].

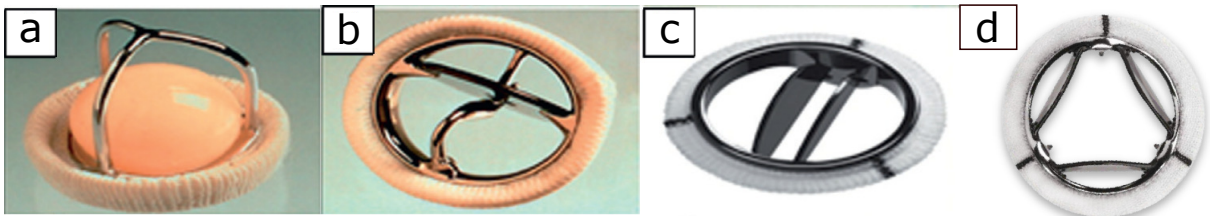

Figure 1.1: Mechanical heart valves; (a) caged-ball valve, (b) tilting-disk valve, (c) bileaflet valve, and (d) trileaflet valve.

1.2.2 Bio-prosthetic heart valves

The BHVs are generally categorized into porcine and bovine pericardium based on their leaflet material. Due to the similarities of these valves, they show hemodynamics similar to native heart valves; therefore, they are less thrombogenic. On the other hand, their lifetime is limited to 10-15 years, thus BHVs are considered mostly for elderly patients. Figure 1.2 shows several different types of BHVs. The porcine and bovine BHVs are geometrically similar and are sewed to a fabric-covered ring but constructed from different animal tissues. The bovine BHVs (figure 1.2(b)) showed better hemodynamics performance and higher orifice area [56] compared to the porcine BHVs (figure 1.2(a)); therefore, most newer BHV designs are made of bovine pericardium. In recent years, a new class of BHV is introduced that consists of bovine or porcine trileaflet valves mounted on a self-expandable or balloon-expandable metallic frame. Two types of these valves are shown in Figure 1.2(c,d). These types of valves are less invasive and do not require removing the old ones; therefore are more favorable for people with a high risk of surgery.

1.3 Objectives and significance

The main objective of this work is to create an inclusive numerical framework incorporating fluid and structure solvers to study the vortex dynamics of cardiovascular flows and their effects on thrombus generation and valve kinematics. More specifically, we aim to analyze vortex rings

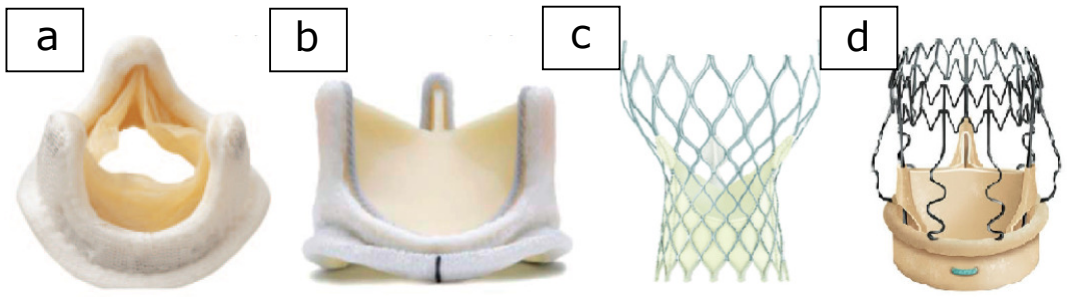

Figure 1.2: bio-prosthetic heart valves; (a) procine, (b) bovine, (c) transcatheter, and (d) sutureless.

propagation and dynamics in the flows with implanted prosthetic heart valves. These complex flows include vortical structures that can affect the hemodynamic forces acting on the blood cells and valves. The changes in hemodynamic forces applied on the platelets can activate them, which could lead to thrombus generation. The altered leaflet kinematics and their delayed closure can lead to regurgitation. Both of these effects can potentially lead to major CVDs. Therefore, in this work, we strive to shed more light on the effects of vortex dynamics on the kinematics and thrombus generation of two main categories of heart valves, i.e., BMHV and BHV. In addition, the implemented numerical framework and the findings of this study can potentially pave the wave for future virtual surgery practices and help the optimization process of prosthetic heart valves.

1.4 State-of-the-art and novelties

The numerical investigation of cardiovascular flows imposes several challenges even to the most advanced computational tools. In this work, we strive to overcome these challenges by finding and implementing novel solutions. Incorporating realistic models, such as the LV as inflow, FSI of the valves, and their contact, are essential to obtain physiologically relevant results. Simplifying assumptions such as fixed leaflets, steady flow, or unrealistic contact, will drastically change the hemodynamics, which prevents making biologically sound conclusions.

The first step for a systematic study of vortex dynamics is to investigate the propagation and dynamics of periodic vortex rings in a simplified setup that could be generalized for a wide range of cardiovascular flows. This will give us a tool to analyze the vortex dynamics for cardiovascular

flows. While non-periodic vortex rings are studied for several decades [57, 58, 59], there is not a systematic study that addresses the dynamics and propagation of periodic vortex rings as a function of governing parameters [60]. In this study, for the first time, we investigate the transient and steady-state dynamics of period vortex rings and propose a scaling law for the location of the vortex rings core centers for a range of non-dimensional numbers.

The numerical investigations of flows around BMHVs have been performed previously [61, 62]. However, the state-of-the-art of BMHV simulations lacks realistic modeling of patient-specific left heart, i.e., LV and aorta, incorporating a contracting LV. Adding the LV to the aorta creates an asymmetric inflow into the aortic orifice, as opposed to a prescribed symmetric inflow [63], which could change the vortex dynamics of the ascending aorta. In this work, we perform a set of multi-block FSI simulations for multiple BMHV implantation orientations and study the vortex dynamics in the anatomic aorta and LV and their effects on the leaflet kinematics and platelet activation for multiple cycles for the first time.

For the simulation of BHVs, a high-deformation thin shell FE framework is implemented, which includes a non-linear and anisotropic material model. During the closing phase, the proper modeling of the contact of the leaflets is of significant importance due to its effects on the coaptation of the valve, which is an indicator of a functioning valve [64]. In previous work, the contact of the leaflets was modeled using the penalty methods [10, 65, 66, 67], which imposed a predefined and ad hoc contact force [24] to avoid inter-penetration of the leaflets. In this work, a novel, efficient, and physic-based contact model is proposed using the coefficient of restitution that does not need numerical experimentation. The proper modeling of the BHV leaflet dynamics makes this framework capable of observing vortex rings during the closing phase for the first time.

2. NUMERICAL METHODS

This chapter is organized as follows: In §2.1, an overview of the overset-curvilinear immersed boundary (overset-CURVIB) method is presented, which is used as the flow solver framework for this work. In §2.2, the governing equations and discretization methods of the thin shell finite element used in this work are introduced, which is utilized as the framework for computing the dynamics of deformable bodies. In §2.3, the proposed contact modeling method is presented, which is integrated into the thin shell framework, making it capable of handling multi-body contact.

2.1 Overview of the Overset-CURVIB

The governing equations for the flow domain are the three-dimensional, unsteady, incompressible Navier-Stokes equations. These equations are solved for a Newtonian fluid in generalized curvilinear coordinates. The Navier-Stokes equations in Cartesian coordinates, using Einstein's notation ($r, q = 1, 2, 3$), can be formulated as

$$\frac{\partial u_r}{\partial x_r} = 0 \tag{2.1}$$

$$\frac{\partial u_q}{\partial t} + \frac{\partial}{\partial x_r}(u_r u_q) = -\frac{\partial p}{\partial x_q} + \frac{1}{Re}\frac{\partial^2 u_q}{\partial x_r \partial x_r} \tag{2.2}$$

where x_r, u_r, p, and Re are the Cartesian coordinates, the Cartesian velocity components, the static pressure divided by density, and the Reynolds number of the flow, respectively.

In order to use body-fitted curvilinear grids, a coordinate transformation is needed to transform the equations 2.1 and 2.2 from Cartesian (x_1, x_2, x_3) to curvilinear coordinates (ξ^1, ξ^2, ξ^3). In this work, a partial transformation approach is used, where the dependent variables are kept in Cartesian coordinates while the independent variables are transformed [45]. This method, known as the hybrid staggered/non-staggered approach, not only machines the continuity equation (equation 2.1) to zero but also rules out the need for using the Christoffel symbols. The transformed form of

the equations 2.1 and 2.2 are [45]

$$J\frac{\partial}{\partial\xi^r}(\frac{U^r}{J}) = 0 \tag{2.3}$$

$$\frac{\partial u_q}{\partial t} + J\frac{\partial}{\partial\xi^r}(\frac{U^r}{J}u_q) + J\frac{\partial}{\partial\xi^r}(\frac{g^{rm}}{J}\frac{\partial p}{\partial\xi^m}) - \frac{1}{Re}J\frac{\partial}{\partial\xi^r}(\frac{\xi^r_{x_q}}{J}u_q) = 0 \tag{2.4}$$

where J is the determinant of the Jacobian of the transformation $J = |\partial(\xi^1, \xi^2, \xi^3)/\partial(x_1, x_2, x_3)|$, $g^{rm} = \xi^r_{x_q}\xi^m_{x_q}$ is the contravariant metric of the transformation, and U^q are the contravariant velocity components in curvilinear coordinates, relating to the velocity components of Cartesian coordinates as

$$U^q = u_r\xi^q_{x_r} \tag{2.5}$$

The Cartesian velocity components on the other way are related to the contravariant velocity components in curvilinear coordinates as

$$u_q = U^r x_r^{\xi^q} \tag{2.6}$$

where $\xi^q_{x_r} = \partial\xi^q/\partial x_r$ and $x_r^{\xi^q} = \partial x_r/\partial\xi^q$. In this approach, the Cartesian velocity components and pressure are stored at center of control volume, while the contravariant velocity components are kept at the faces of the control volume [45].

In this framework, curvilinear grids are used to efficiently discretize the fluid domain as a background grid, in which the immersed bodies are placed. The sharp-interface immersed boundary method is shown to be second-order accurate in space and time [42, 68]. Furthermore, an efficient ray-tracing algorithm is augmented to classify the grid nodes into fluid, solid, and immersed boundary nodes, which can handle large movements of multiple immersed bodies [46]. The fluid domain equations are integrated in time using an efficient, second-order fractional step method coupled with implicit Runge-Kutta solver for the momentum equation (equation 2.4) and generalized minimal residual (GMRES) solver enhanced with multigrid as a preconditioner for the

Poisson equation (see Ref. [45] for more details)

$$-\frac{\partial}{\partial \xi^r}\left(\frac{\xi_q^r}{J}G^q(\phi)\right) = \frac{3}{2\Delta t}\frac{\partial U^*}{\partial \xi^r} \tag{2.7}$$

where $\phi = p^{(n+1)} - p^{(n)}$, U^* are the intermediate fluxes, and $G^q(\phi) = -\frac{\partial}{\partial \xi^k}(\frac{1}{J}\phi\xi^k_{x_q})$ is the gradient operator.

The partitioned fluid-structure interaction (FSI) solver employed in this work partitions the domain into two separate fluid and structure domains, in which a coupling algorithm is applied at their interface. We employed a strong coupling FSI strategy (SC-FSI), in which the boundary conditions at the interface are updated from the solution at the current time level [46]. Due to unconditionally unstable FSI iterations during the opening phase of the valve, observed in numerical experiments and theoretical analysis, SC-FSI is supplemented with under-relaxation in conjunction with Aitken acceleration technique to improve the stability of the simulations [46].

2.2 Shell Element Governing Equations and Boundary Conditions

Heart valves are thin shell structures with complicated strain-stress relations that undergo large deformations. We have implemented a large deformation, rotation-free, thin shell finite element (FE) framework based on Loop's subdivision surfaces [69] on unstructured triangular mesh that incorporated a nonlinear and anisotropic material model and is capable of handling the contact of leaflets efficiently. In §2.2.1, a brief description of the classical Kirchhoff-Love theory [70] based on stress-resultant formulation is presented. In §2.2.2, the discretization of the equations of motion is addressed. For the sake of completeness, the constitutive equations of two material models [6, 71] implemented in the framework are addressed in §2.2.3. Then, a brief overview of FE discretization of Loop's subdivision surfaces [69] with short notes on different boundary conditions tailored for subdivision surfaces [72] are given in §2.2.4 and 2.2.5, respectively.

The following notation is used throughout this section: The Greek indices α and β take the values of 1 and 2 and Latin indices i and j take values from 1 to 3 and refer to spatial dimensions. Here, a comma is used to denote partial differentiation.

2.2.1 The Kirchhoff-Love Theory

The position vector of a material point of the shell with thickness h in reference and deformed configurations may be parameterized in a curvilinear coordinate system of $\{\theta^1, \theta^2, \theta^3\}$, respectively, as

$$\bar{\mathbf{r}}(\theta^1, \theta^2, \theta^3) = \bar{\mathbf{x}}(\theta^1, \theta^2) + \theta^3 \bar{\mathbf{a}}_3(\theta^1, \theta^2), \quad -\frac{h}{2} \leq \theta^3 \leq \frac{h}{2} \tag{2.8}$$

$$\mathbf{r}(\theta^1, \theta^2, \theta^3) = \mathbf{x}(\theta^1, \theta^2) + \theta^3 \mathbf{a}_3(\theta^1, \theta^2), \quad -\frac{h}{2} \leq \theta^3 \leq \frac{h}{2} \tag{2.9}$$

The vectors $\bar{\mathbf{x}}(\theta^1, \theta^2)$ and $\mathbf{x}(\theta^1, \theta^2)$ are parametric representations of the middle surface of the shell in reference and deformed configurations, respectively. The middle surface basis vectors are

$$\bar{\mathbf{a}}_\alpha = \bar{\mathbf{x}}_{,\alpha}, \quad \mathbf{a}_\alpha = \mathbf{x}_{,\alpha} \tag{2.10}$$

and based on Kirchhoff-Love theory, the material orientation in the thickness direction of the shell $\bar{\mathbf{a}}_3$ and $\mathbf{a}_3$ are the shell directors in reference and deformed configurations, respectively. The covariant basis vectors for a generic point within the shell are given by

$$\bar{\mathbf{g}}_\alpha = \frac{\partial \bar{\mathbf{r}}}{\partial \theta^\alpha} = \bar{\mathbf{a}}_\alpha + \theta^3 \bar{\mathbf{a}}_{3,\alpha}, \quad \bar{\mathbf{g}}_3 = \frac{\partial \bar{\mathbf{r}}}{\partial \theta^3} = \bar{\mathbf{a}}_3 \tag{2.11}$$

$$\mathbf{g}_\alpha = \frac{\partial \mathbf{r}}{\partial \theta^\alpha} = \mathbf{a}_\alpha + \theta^3 \mathbf{a}_{3,\alpha} \qquad \mathbf{g}_3 = \frac{\partial \mathbf{r}}{\partial \theta^3} = \mathbf{a}_3 \tag{2.12}$$

The covariant components of the corresponding metric tensors in both configurations are

$$\bar{g}_{ij} = \bar{\mathbf{g}}_i . \bar{\mathbf{g}}_j, \quad g_{ij} = \mathbf{g}_i . \mathbf{g}_j \tag{2.13}$$

The Green-Lagrange strain tensor is given as

$$E_{ij} = \frac{1}{2}(g_{ij} - \bar{g}_{ij}) \tag{2.14}$$

By substituting equations 2.11-2.13 into equation 2.14 and taking into account the thin shell Kirchhoff-Love theory assumptions [69], the Green-Lagrange strain tensor takes the form of

$$E_{\alpha\beta} = E^m_{\alpha\beta} + \theta^3 E^b_{\alpha\beta} \tag{2.15}$$

where $E^m_{\alpha\beta}$ and $E^b_{\alpha\beta}$ are the membrane and bending strain tensors, respectively and are defined in local curvilinear coordinates as

$$E^m_{\alpha\beta} = \frac{1}{2}(\mathbf{a}_\alpha.\mathbf{a}_\beta - \bar{\mathbf{a}}_\alpha.\bar{\mathbf{a}}_\beta) \tag{2.16}$$

$$E^b_{\alpha\beta} = \mathbf{a}_\alpha.\mathbf{a}_{3,\beta} - \bar{\mathbf{a}}_\alpha.\bar{\mathbf{a}}_{3,\beta} \tag{2.17}$$

Equations 2.16 and 2.17 are used in §2.2.2 to calculate the variation of membrane and bending strains and the internal forces of the elements.

2.2.2 Equations of Motion

The dynamic equations of motion for each node can be written in the residual (**R**) form as

$$\mathbf{R} = M\ddot{\mathbf{x}} + C\dot{\mathbf{x}} + \mathbf{F}_{int} + \mathbf{F}_{cnt} - \mathbf{F}_{ext} = 0 \tag{2.18}$$

where $\ddot{\mathbf{x}}$, $\dot{\mathbf{x}}$, $\mathbf{F}_{int}$, $\mathbf{F}_{cnt}$, and $\mathbf{F}_{ext}$ are acceleration, velocity, the internal, contact, and external forces, respectively. Mass (M) and damping (C) properties at each node are obtained by adding equal shares of each neighboring element. Equation 2.18 is discretized using the Newmark constant average acceleration method [73] with $\beta = 0.25$ and $\gamma = 0.5$

$$\mathbf{R}(\mathbf{x}^{n+1}) = \frac{M}{\beta\Delta t^2}\mathbf{x}^{n+1} - \mathbf{F}^n_{acc} + \frac{C\gamma}{\beta\Delta t}\mathbf{x}^{n+1} - \mathbf{F}^n_{dmp} + \mathbf{F}^{n+1}_{int} + \mathbf{F}^{n+1}_{cnt} - \mathbf{F}^{n+1}_{ext} = 0 \tag{2.19}$$

where the acceleration and damping forces at time level n are

$$\mathbf{F}^n_{acc} = M[\frac{1}{\beta\Delta t^2}\mathbf{x}^n + \frac{1}{\beta\Delta t}\dot{\mathbf{x}}^n + (\frac{1}{2\beta} - 1)\ddot{\mathbf{x}}^n] \tag{2.20}$$

$$\mathbf{F}^n_{dmp} = C[\frac{\gamma}{\beta\Delta t}\mathbf{x}^n + (\frac{\gamma}{\beta} - 1)\dot{\mathbf{x}}^n + \Delta t(\frac{\gamma}{2\beta} - 1)\ddot{\mathbf{x}}^n] \tag{2.21}$$

The nonlinear equations of motion (equation 2.19) are solved using a Jacobian-free Newton-Krylov method [74], which is known to have quadratic convergence.

The internal force of each element after integration using one-point quadrature rule at the barycenter of the element is given as

$$\mathbf{F}^{n+1}_{int} = A_0(\frac{h^3}{12}[\mathbf{B}^b]^T\mathbf{S}^b + h[\mathbf{B}^m]^T\mathbf{S}^m) \tag{2.22}$$

where A_0, h, $\mathbf{S}^b$, and $\mathbf{S}^m$ are the area of the element and the thickness of the shell at reference configuration, the bending and membrane second Piola-Kirchhoff stress tensors, respectively. The strain-displacement matrices for membrane ($\mathbf{B}^m$) and bending ($\mathbf{B}^b$) strains, which provides the variation of strains, are given as

$$\mathbf{B}^m = \frac{\partial E^m_{\alpha\beta}}{\partial \mathbf{u}}, \quad \mathbf{B}^b = \frac{\partial E^b_{\alpha\beta}}{\partial \mathbf{u}} \tag{2.23}$$

where $\mathbf{u}$ is the nodal displacement. The calculation of stresses and displacements will be discussed in subsections 2.2.3 and 2.2.4, respectively.

After solving equation 2.19 and obtaining the solution ($\mathbf{x}^{n+1}$), the acceleration and velocity at time level $n+1$ according to Newmark method are

$$\ddot{\mathbf{x}}^{n+1} = \frac{1}{\beta\Delta t^2}(\mathbf{x}^{n+1} - \mathbf{x}^n) - \frac{1}{\beta\Delta t}\dot{\mathbf{x}}^n - (\frac{1}{2\beta} - 1)\ddot{\mathbf{x}}^n \tag{2.24}$$

$$\dot{\mathbf{x}}^{n+1} = \frac{\gamma}{\beta\Delta t}(\mathbf{x}^{n+1} - \mathbf{x}^n) - (\frac{\gamma}{\beta} - 1)\dot{\mathbf{x}}^n - \Delta t(\frac{\gamma}{2\beta} - 1)\ddot{\mathbf{x}}^n \tag{2.25}$$

2.2.3 Constitutive Models

In this work, two sets of constitutive equations have been implemented in a local Cartesian system. The well-known Neo-Hookean [71] constitutive equations are used to simulate linear and isotropic materials for the simulation of the thin shell benchmarks in §3.2.1, §3.2.3, §3.2.4, §3.2.6,

and §3.2.7 and the impact benchmarks in §3.3.1-§3.3.3.

For the BHV simulations, the full experiment-based shell element model of Kim et al. [6] has been implemented, which is used in biaxial loading tests of a BHV patch in §3.2.2 and compared against experimental results of a BHV in a static simulation in §3.3.4 as well as used in dynamic simulations in §3.3.5. This model which accounts for fiber directions, uses a Fung-type constitutive equations for membrane, which gives the membrane second Piola-Kirchhoff stress tensor components ($S^m_{\alpha\beta}$) as

$$\begin{aligned} S^m_{11} &= ce^Q(A_1E^m_{11} + A_3E^m_{22} + A_5E^m_{12}) \\ S^m_{22} &= ce^Q(A_3E^m_{11} + A_2E^m_{22} + A_6E^m_{12}) \\ S^m_{12} &= ce^Q(A_5E^m_{11} + A_6E^m_{22} + A_4E^m_{12}) \end{aligned} \tag{2.26}$$

where c and A_i are material constants and Q is of the form

$$\begin{aligned} Q =& A_1{E^m_{11}}^2 + A_2{E^m_{22}}^2 + 2A_3E^m_{11}E^m_{22} + A_4{E^m_{12}}^2 \\ &+ 2A_5E^m_{11}E^m_{12} + 2A_6E^m_{22}E^m_{12} \end{aligned} \tag{2.27}$$

Here we used the constant values of Kim et al. [6] which are taken from biaxial tests. These values are $c = 14.42\ kPa$ and A_1 to A_6 are equal to 61.27, 70.37, 5.11, 14.20, 3.10, and 2.01, respectively.

For the bending response, Kim et al. [6] obtained a quadratic moment-curvature relation from three-point tests that gives the bending second Poila-Kirchhoff stress tensor components ($S^b_{\alpha\beta}$) the form

$$\begin{aligned} S^b_{11} &= a_1E^b_{11} + b_1 sign(E^b_{11}){E^b_{11}}^2 + 0.25(a_1 + a_2)E^b_{22} \\ S^b_{22} &= 0.25(a_1 + a_2)E^b_{11} + a_2E^b_{22} + b_2 sign(E^b_{22}){E^b_{22}}^2 \\ S^b_{12} &= 0.25(a_1 + a_2)E^b_{12} \end{aligned} \tag{2.28}$$

where a_1 and a_2 are 0.443 and 0.620 N/mm^2 and b_1 and b_2 are equal to 4.302 and 6.023 N/mm, respectively. In equations 2.26 - 2.28, indices 1 and 2 refer to preferred and cross-preferred fiber

directions in reference configuration, respectively, which require a rotation of strains (equations 2.16 and 2.17) from local arbitrary Cartesian coordinates to preferred fiber direction [66].

2.2.4 Subdivision Surfaces

In order to generate a smooth interpolated displacement field possessing bounded energy within the framework of the Kirchhoff-Love thin shell theory, FE implementation of Loop's subdivision surfaces [69, 75] is employed and used for calculating strain tensors (equations 2.16 and 2.17) and strain-displacement matrices (equation 2.23) and applied to BHV simulations for the first time. The advantage of this method to traditional finite elements is that the subdivision surfaces method has C^1 continuity, or H^2 integrability to bound energy of a shell by using larger local support of the shape functions [72]. In other words, shape functions employed in this method are square-integrable whose first- and second-order derivatives are themselves square-integrable [69].

In this method, the vertices of the triangular mesh are divided into two categories based on their valence, i.e., the number of the edges attached to that vertex: (1) regular vertices, which have a valence of 6; and (2) irregular vertices, which have valence other than 6. For triangular elements with three regular vertices, a quartic box-spline patch with 12 control points are formed (regular patch), which enables efficient interpolation of a given field as

$$\mathbf{x}(\theta^1, \theta^2) = \sum_{I=1}^{12} N^I(\theta^1, \theta^2)\mathbf{x}_I \tag{2.29}$$

where index I refers to the local numbering of the nodes and N is the shape function [69].

For elements with one irregular vertex, a subdivision of the element is performed in two steps of refinement and smoothing. In the refinement step, each triangle is divided into four finer ones by quadrisecting. Then, the coordinates of all the vertices, including the vertices of the coarse mesh, are recalculated with a weighted average of the coarse mesh [76]. After these steps, three regular finer patches are available for interpolation of the desired variable field, of which the central one is chosen due to the one-point quadrature rule. Therefore, for irregular patches, equation 2.29 takes

the form of

$$\mathbf{x}(\theta^1, \theta^2) = \sum_{I=1}^{12} N^I(\theta^1, \theta^2)\mathbf{P}_I\mathbf{A}\mathbf{x}^0 \tag{2.30}$$

where $\mathbf{P}_I$ extracts the control nodes, $\mathbf{A}$ is the subdivision matrix, and $\mathbf{x}^0$ is the location of the original coarse patch (see Cirak et al.[69] for more details). The interpolation equations of 2.29 and 2.30 are used in calculating basis vectors and their derivatives to form strain tensors and strain-displacement matrices.

2.2.5 Boundary Conditions

The implementation of boundary conditions for subdivision surfaces requires adding one layer of ghost nodes to the unstructured triangular grid as the elements on the boundary lack a complete 1-ring patch in order to use the shape functions [72] introduced in §2.2.4. The ghost nodes are positioned according to figure 2.1 as $\mathbf{x}_4 = \mathbf{x}_2 + \mathbf{x}_3 - \mathbf{x}_1$ for all the usual boundary conditions. For clamped boundaries, the position of all the nodes near and on the boundary as well as ghost nodes are kept fix. For pinned boundaries, the position of nodes 2 and 3 are fixed, and therefore displacement $\mathbf{u}_4 = -\mathbf{u}_1$ is considered [69]. The locations of the ghost nodes for free boundaries are simply left unconstrained [77], i.e, their position would be updated at each time step based on forces exerted from neighboring elements.

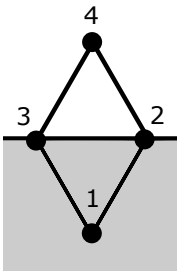

Figure 2.1: Boundary conditions are applied by adding ghost nodes (node 4) to the triangular mesh.

2.3 A New Contact Model for Shell Elements

The inter-leaflet collision can occur during the closing phase of a BHV dynamic. The first step of contact handling of two colliding bodies is to detect the contact, which needs to be implemented efficiently as it is called mesh-wide on each time step. We consider two bodies in contact if one node of one body penetrates an element of the other body, which happens when the signed normal distance of the node to the element is negative (in the opposite direction of the element normal). Here, we used the contact detection strategy of Borazjani [78]. For each triangular element, a bounding sphere is defined and the distance of the node to the element is checked only if the node lies inside the bounding sphere. Additionally, the number of triangles for which the distance is checked is reduced by creating bounding boxes and control cells. The bounding box does not check for contact if the node is outside of the box bounding the other body. The control cells divide each bounding box into smaller cells and create a list of elements inside each of them; therefore, only the distance of the node is checked with elements inside the control cell. Note that utilizing the bounding spheres in the search algorithm makes the method capable of simulating a simple self-contact scenario, in which only the outer side (in direction of the element normal) of the shell surface contacts itself.

Once the contact is detected, the interpenetration prevention step is performed by applying two independent steps. In the first step, the impenetrability constraints are enforced by projecting the penetrating node back to the element surface. In figure 2.2(a), the contact of node A to the shaded element is detected and the constraint is applied by projecting it onto the element surface (node A' in figure 2.2 (b)). This step can alter the energy of the penetrating body by the amount of $(\mathbf{F}_{int\ A} - \mathbf{F}_{ext\ A}).(\mathbf{x}_A - \mathbf{x}_{A'})$.

The next step is to exchange the momenta of the impacting bodies, assuming that the contact is frictionless. In order to use simple particle-particle impact equations, the impact of node A is considered with its projection on the element surface (B) according to figure 2.2. The equations of conservation of momentum in normal to the element direction ($\mathbf{n}$) for velocities of points A and B

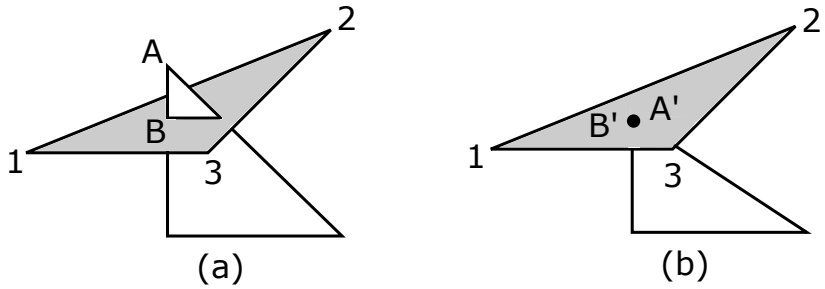

Figure 2.2: (a) Contact of node A with the shaded element is detected. (b) Impenetrability constraint is enforced by projecting node A back on the element surface (A').

based on the general equation of motion (equation 2.18) are given as

$$\frac{d}{dt}(m_A \dot{x}_{A\,n}) + F_{int\ A\,n} + F_{cnt} - F_{ext\ A\,n} = 0 \tag{2.31}$$

$$\frac{d}{dt}(m_B \dot{x}_{B\,n}) + F_{int\ B\,n} - F_{cnt} - F_{ext\ B\,n} = 0 \tag{2.32}$$

where $F_{int\ B\,n}$ and $F_{ext\ B\,n}$ are the sum of the internal and external forces of element vertices in the normal direction, respectively, and F_{cnt} for points A and B are opposite and equal. Note that the damping term is ignored in the above equations compared to equation 2.18 because it will be implicitly considered using the coefficient of restitution. By adding equations 2.31 and 2.32, integrating over time, e.g., using trapezoidal rule, and considering velocities of points A and B in normal to the element direction before ($\dot{x}_{A\,n}$ and $\dot{x}_{B\,n}$) and after the impact ($\dot{x}_{A'n}$ and $\dot{x}_{B'n}$), it is found that

$$\begin{aligned} m_A \dot{x}_{A\,n} + m_B \dot{x}_{B\,n} - \Delta t_{impact}(F_{int\ A\,n} + F_{int\ A'n} + F_{int\ B\,n} + F_{int\ B'n} \\ -F_{ext\ A\,n} - F_{ext\ A'n} - F_{ext\ B\,n} - F_{ext\ B'n})/2 = m_A \dot{x}_{A'n} + m_B \dot{x}_{B'n} \end{aligned} \tag{2.33}$$

The third term in the left-hand side of equation 2.33 is the impulse of internal and external forces (with Δt_{impact} being the time of impact) applied on the nodes involved in the contact. This impulse is negligible considering that the impact duration goes to zero in the limit for each time step.

According to the definition of restitution coefficient (e), the normal velocities before and after the impact are given as

$$(\dot{x}_{B'n} - \dot{x}_{A'n}) = e(\dot{x}_{A\,n} - \dot{x}_{B\,n}) \tag{2.34}$$

Combining equations 2.33 and 2.34 leads to

$$\begin{bmatrix} \dot{x}_{A'n} \\ \dot{x}_{B'n} \end{bmatrix} = \frac{1}{m_A + m_B} \begin{bmatrix} m_A - em_B & m_B(1+e) \\ m_A(1+e) & m_B - em_A \end{bmatrix} \begin{bmatrix} \dot{x}_{A\,n} \\ \dot{x}_{B\,n} \end{bmatrix} \tag{2.35}$$

where velocities in tangential direction remain the same due to the friction-less contact assumption. Using the above equation, the velocities of points A and B after contact can be found. Nevertheless, the relation of mass and velocity of point B with nodes 1-3 should be derived (figure 2.2). Such relation is derived by ensuring that the momentum can remain conserved during the contact, assuming that the impulse of internal and external forces is negligible.

The momentum before and after contact in the normal direction **n** globally remains the same

$$\sum_j m_j(\dot{x}_{j'n} - \dot{x}_{j\,n}) = 0 \tag{2.36}$$

where $'$ indicates the velocities after impact and the sum is over all nodes. Let's consider, to simplify the discussion and without the loss of generality, just the collision between point A with the element shown in figure 2.2. Consequently, only the momentum of nodes A and the nodes 1-3 of the element containing point B will be changed

$$m_A(\dot{x}_{A'n} - \dot{x}_{A\,n}) + [m_1(\dot{x}_{1'n} - \dot{x}_{1\,n}) + m_2(\dot{x}_{2'n} - \dot{x}_{2\,n}) + m_3(\dot{x}_{3'n} - \dot{x}_{3\,n})] = 0 \tag{2.37}$$

For the above equation to be consistent with the momentum exchange equation of points A and B (equation 2.33), the terms in the brackets should be equal to the change in momentum of point B

$$m_B\dot{x}_{B\,n} = m_1\dot{x}_{1\,n} + m_2\dot{x}_{2\,n} + m_3\dot{x}_{3\,n} \tag{2.38}$$

$$m_B \dot{x}_{B'n} = m_1 \dot{x}_{1'n} + m_2 \dot{x}_{2'n} + m_3 \dot{x}_{3'n} \tag{2.39}$$

In the above two equations, there are six unknowns, i.e., m_B, normal velocities of point B before and after contact, and normal velocities of nodes 1-3 after contact. A good assumption on the velocities of nodes 1-3 after contact is that they are equal to the velocity of point B, i.e., all the points on the shaded element in figure 2.2 move with the same velocity after contact

$$\dot{x}_{B'n} = \dot{x}_{1'n} = \dot{x}_{2'n} = \dot{x}_{3'n} \tag{2.40}$$

Substituting the above in equation 2.39, m_B is found to be the sum of masses of nodes 1-3

$$m_B = m_1 + m_2 + m_3 \tag{2.41}$$

With the known mass of point B, the normal velocity of point B before impact is obtained from equation 2.38 as

$$\dot{x}_{B\,n} = \frac{m_1}{m_B}\dot{x}_{1\,n} + \frac{m_2}{m_B}\dot{x}_{2\,n} + \frac{m_3}{m_B}\dot{x}_{3\,n} \tag{2.42}$$

Now the modeling for the exchange of momenta is complete. After computing mass (m_B) and normal velocity of point B before the impact ($\dot{x}_{B\,n}$) from equations 2.41 and 2.42, respectively, the normal velocities of point B and node A after impact will be computed using equation 2.35 based on the known coefficient of restitution e. Finally, using the computed velocity of point B after impact, the normal velocities of nodes 1-3 will be updated (equation 2.40).

In this method, the contact force is applied implicitly such that it satisfies the kinematic condition in contrast to the penalty method, where the location, velocity, and acceleration are calculated based on the exerted contact force. The main difference of this method with the penalty method is that this method is generic, while for the penalty method, the profile of the contact force might be different given different geometries and loading and needs numerical ad hoc experimentation to find the appropriate function form. The layout of the proposed method is similar to the DCR method [79], with a major difference in the momenta exchange step. The exchange of momenta in

the DCR method is performed by applying self-equilibrating impulses to the nodes participating in contact by using constraint functions, which has high computational cost for high-resolution simulations, while the proposed method simplifies the contact of a node-element to a particle-particle impact problem with simple considerations.

3. VALIDATIONS AND VERIFICATIONS

In this chapter, different aspects of the numerical framework are validated and verified separately, i.e., flow solver, structure solver, contact modeling, and FSI solver, respectively. First, an overview of the history of the validation studies of the overset-CURVIB method is provided in §3.1. In this section, an extra validation study is presented (§3.1.1) that specifically investigates the vortex ring propagation. Then, different aspects of the FE solver are validated against numerical, experimental, and analytical solutions in §3.2. The contact modeling validation and verification test cases are presented in §3.3. Finally, in §3.4, a challenging FSI benchmark including deformable body and large eddy simulation (LES) is discussed, which is solved using the FSI FE-CURVIB framework.

3.1 Overview of the Overset-CURVIB Validations

The overset-CURVIB framework used in this work has been extensively validated and verified against different benchmark solutions (see [80] for more details). The overset grid results are shown to have the same accuracy as a single grid for a rotationally oscillating cylinder. Furthermore, the overset CURVIB results was validated against experimental and other numerical data for a 90 deg pipe bend [80]. This framework has been shown to have second-order accuracy using the lid-driven cavity flow benchmark [80]. Furthermore, the flow features and computational time of the overset-CURVIB approach for a self-propelled mackerel are compared against the single grid CURVIB approach [80].

The FSI solver utilized here is extensively described and validated against experimental data of a BMHV in a straight axisymmetric aorta [46]. This solver has been employed to simulate the flow in an anatomically realistic aorta with an implanted BMHV [61] at different orientations [63]. Furthermore, it has been successfully applied to simulate the flow in a contracting LV [81] and for a BMHV implanted in an LV-aorta configuration [80]. Therefore, the governing equations, the numerical method, and validation studies are briefly described in this work and the reader is

referred to the previous publications for more details [46, 80, 61, 63, 81].

3.1.1 Vortex Detection and Validation[1]

In this subsection, the propagation of vortex rings is validated in which the imposing pulsed jet at the inlet of a cylinder create vortices exiting to a tank. We have validated our method against experimental data of [1] by simulating their exact setup (test cases 1 and 2 in table 4.1). It is noted that these test cases are non-periodic, in contrast to the rest of test cases (3 to 20). For numerical simulations, the location of the vortex ring core centers were detected by plotting the out-of-plane vorticity field on the mid-plane of the domain and locating the points with maximum vorticity magnitudes similar to what is done in experiments. The location of the vortex core centers (S) were measured with respect to the edge of the cylinder, as shown in figure 4.1(a). For test cases 1 and 2, the vortex cores were tracked after $tU_{jet}/D = 1$ (U_{jet} and D are the pulse nominal jet velocity and cylinder diameter, respectively), when the ring is fully formed and detached, similar to the experiments [1]. This is better demonstrated in figure 3.1, which shows the out-of-plane vorticity contours and velocity vectors for case 1 at three time instants. The plus sign denotes the location of highest vorticity, i.e., the vortex core center. The results are in good agreement with the visualizations of [1]. In figure 3.1, the thick green lines depict the vortex core boundaries identified by the Burgers' vortex model.

The Burgers' vortex model is the exact solution of Navier-Stokes equations for a steady viscous vortex where the stretching and viscous effects are in balance [82]; therefore, the total variation of enstrophy, $\Omega = \frac{1}{2}\omega_i\omega_i$, is zero, where ω_i is the i^{th} component of vorticity. The total variation of enstrophy for an incompressible flow with constant viscosity is [83]:

$$\frac{D\Omega}{Dt} = \omega_i\omega_j\frac{\partial u_i}{\partial x_j} + \frac{1}{Re}\frac{\partial^2\Omega}{\partial x_j\partial x_j} - \frac{1}{Re}\frac{\partial\omega_i}{\partial x_j}\frac{\partial\omega_i}{\partial x_j}. \tag{3.1}$$

Based on Burgers' model, the vortex center is located at the peak vorticity while the boundaries of vortex cores are defined as the locations around the core center at which the ratio of vorticity

[1]This subsection has been published as a part of "H. Asadi, H. Asgharzadeh, and I. Borazjani. "On the scaling of propagation of periodically generated vortex rings," *Journal of Fluid Mechanics*, vol. 853, pp. 150-170, 2018."

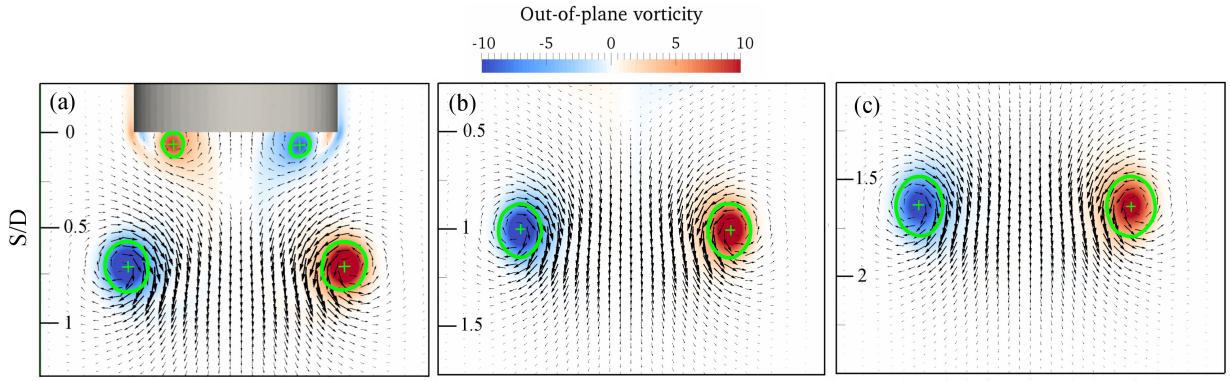

Figure 3.1: Out-of-plane vorticity contours and velocity vectors for test case 1 at times (*a*) $tU_{jet}/D = 2.62$, (*b*) $tU_{jet}/D = 3.68$, and (*c*) $tU_{jet}/D = 5.8$. The thick green lines and plus signs depict vortex ring core boundaries and their centers, respectively.

magnitude to peak vorticity equals to e^{-1} [84, 85]. The probability density functions (PDFs) of the absolute value of the total variation of enstrophy are concentrated around zero for all the test cases at different time instants. Consequently, the stretching and viscous effects are in balance. This justifies using Burgers' model for detecting vortical structures for this study.

The vortex core center locations for experimental data were extracted from the velocity field and flow visualization figures reported in [1] using WebPlotDigitizer software. The time history of location of vortex ring core centers are shown in figure 3.2. The numerical results follow the experimental ones closely for both low $Re_{jet} = 2800$ simulations (figure 3.2(*a*)) and high $Re_{jet} = 23000$ using LES (figure 3.2(*b*)). Here, the Reynolds number is defined as $Re_{jet} = U_{jet}D/\nu$. The experimental results for the first case (figure 3.2(*a*)) show an upward curvature, which is not observed in the numerical results for case 2, and might be due to our approximation of the core centers from the reported figures because such an increase in velocity is not expected after the rings are fully formed. In fact, the propagation speed is expected to slightly decay for long times [86]. To rule out that this is due to the resolution of our grid, a grid dependency study was also performed for case 1 (see figure 3.2(*a*)) with a finer grid, labeled Grid 2 with 54 million grid points, against the original grid, labeled Grid 1 with 15 million grid points. The resolution of Grid 2 is twice of Grid 1 in the region of interest. As can be observed in figure 3.2, the core center locations

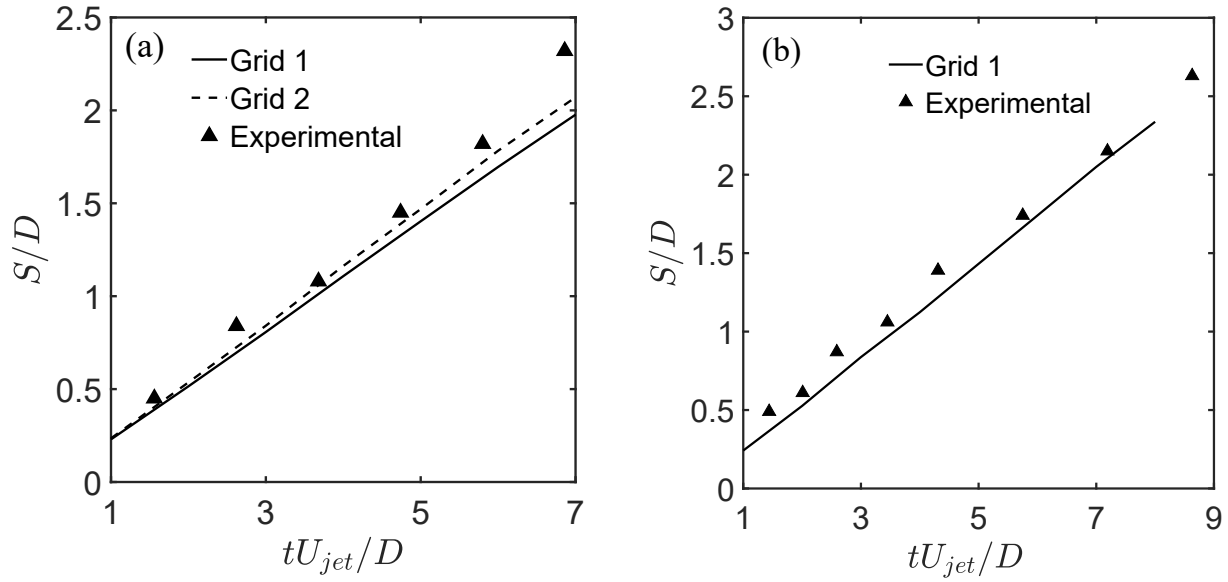

Figure 3.2: Comparisons of vortex core center locations of simulations on grids 1 and 2 with 15 and 54 million grid points, respectively, against experimental data [1]: (*a*) $Re_{jet} = 2800$ (case 1) and (*b*) $Re_{jet} = 23000$ (case 2).

of Grid 1 are within 4% of Grid 2 and show the same trend, i.e., the results are independent of the grid resolution.

3.2 Shell Element Validations

In this section, a series of standard test problems are performed for the validation of different aspects of the implemented thin shell FE framework. These problems are designated to test our framework for geometric and material non-linearity. The membrane patch tests are performed in §3.2.1 and §3.2.2 for Neo-Hookean and nonlinear material models of Kim et al. [6], respectively. In §3.2.3 and §3.2.4, a plate under pressure leading and a cantilever under tip loading are presented, respectively. The response of a cantilever under dynamic tip loading for a predefined material model is compared to the analytical solution in §3.2.5. Finally, the stretched cylindrical shell and pinched hemispherical shell benchmarks are studied in §3.2.6 and §3.2.7, respectively.

3.2.1 Membrane Patch Test

A patch consisting of 289 grid nodes, shown in figure 3.3 (a), is used to perform the membrane patch test for a Neo-Hookean material. A displacement equal to $\mathbf{u} = \mathbf{x}$ was applied to the boundary nodes of a square plate of side $1m$ (figure 3.3 (b)), which according to the analytical solution, should result in a constant Green-Lagrange strain of 1.5. Our result shows a maximum error of 4% for membrane strain distribution of internal elements (figure 3.3 (c)).

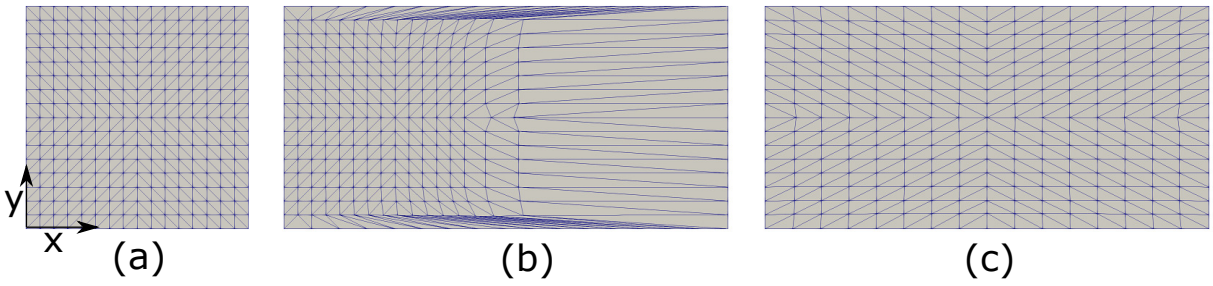

Figure 3.3: (a) Patch of elements used for a membrane patch test at reference configuration. (b) Displacement equal to **x** was applied on the boundary nodes of the patch. (c) The solution obtained for internal nodes.

3.2.2 Biaxial Loading of a BHV Patch

In order to check the implementation of the BHV material model, discussed in §2.2.3, in-plane distributed tensile external forces are applied at the edges of a square patch with 15 mm side corresponding to Lagrangian stress distribution of 20 and 60 kPa in x- and y-directions, respectively (figure 3.4). The responses of two patches with 149 grid points and fiber direction of 0 and 45^o orientations with respect to x-axis, are shown in figure 3.4 (b) and (c), respectively. We found that our results are qualitatively in good agreement with the results of Hammer et al.[66].

3.2.3 The plate under Static Uniformly Distributed Load

In this example, a square plate with 497 grid points is subjected to a uniformly distributed pressure loading perpendicular to the initial configuration. The plate has a side of $L = 20m$, the

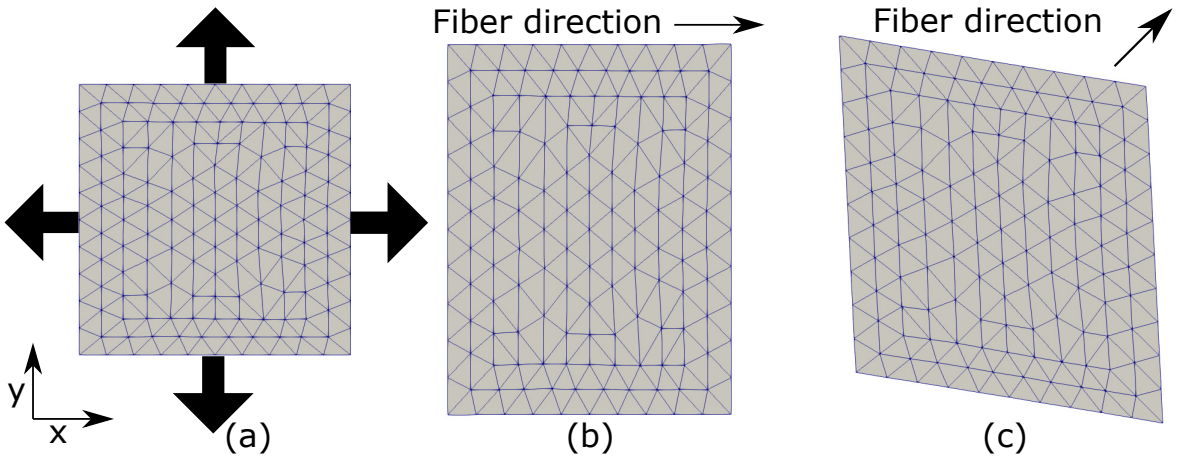

Figure 3.4: Biaxial loading ($P_x : P_y = 20 : 60\ kPa$) of a BHV membrane patch. (a) undeformed mesh showing the directions of applied stresses. (b) Deformed mesh with material fiber direction in x-axis. (c) Deformed mesh with material fiber direction oriented at 45^o to x-axis.

thickness of $h = 1m$, Young's moduli of $E = 12N/m^2$, and the Poisson ratio of $\nu = 0$. The displacement of the center of the plate is compared with FE results [2] for different pressure values in figure 3.5 (a), which shows good agreement with a maximum error of 3%. The smooth deformed shape of the plate under pressure loading of $P = 0.04N/m^2$ is illustrated in figure 3.5 (b).

3.2.4 Cantilever under Static Concentrated Tip Force

A rectangular cantilever with length, width, and thickness of $L = 0.04m$, $b = 0.004m$, and $h = 6 \times 10^{-4}m$, respectively, is subjected to a concentrated tip force. The cantilever is made of 133 grid points and has Young moduli of $E = 2 \times 10^5 N/m^2$ and a Poisson ratio of $\nu = 0$. The tip displacement for different values of tip force (F) is compared to the analytical solution [3] in figure 3.6 (a), which shows excellent agreement. Figure 3.6 (b) illustrates the reference and deformed shapes of the cantilever for a tip force of $F = 5.4 \times 10^{-5}N$.

3.2.5 Cantilever under Dynamic Force

In order to test the dynamic response of the shell formulation with a nonlinear material property, an initially straight and at rest cantilever is considered which is subjected to a dynamic force perpendicular to the initial configuration. The velocity and displacement at the initial condition

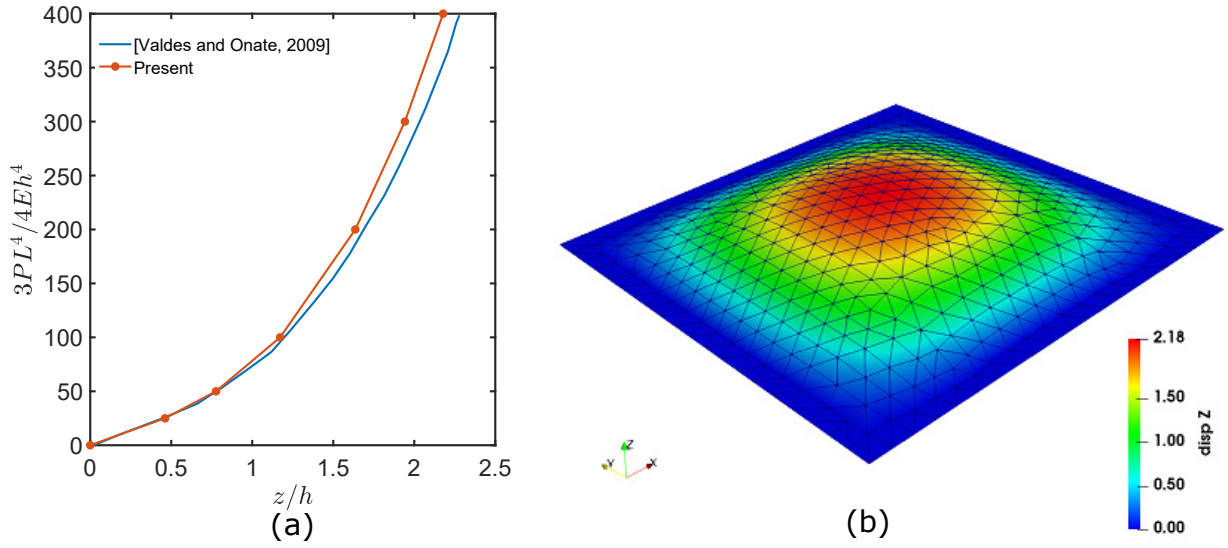

Figure 3.5: A plate under uniformly distributed static pressure loading with $L = 20m$, $h = 1m$, $E = 12N/m^2$, and $\nu = 0$; (a) comparison of central displacement under different pressure loading with FE solution [2] and (b) deformed shape of the plate for $P = 0.04N/m^2$.

are zero. One end of the beam is free while the opposite end is clamped. The dynamic force is manufactured and applied based on a given displacement and a nonlinear material property, i.e., manufactured solution method. Note that in this subsection, variables with tilde represent dimensional values. The elasticity of the beam is defined as a nonlinear function of the non-dimensional distance from the clamped end of the cantilever ($x = \tilde{x}/L$):

$$E(x) = E_0(1 + x^2) \tag{3.2}$$

where L is the length of the cantilever and E_0 is the elasticity at the clamped end ($x = 0$). A dynamic non-dimensional displacement of the cantilever ($W = \tilde{W}/L$) is assumed as:

$$W(x, t) = ax^2 cos(\eta t) \tag{3.3}$$

where a is constant and determines the size of the displacement, which is considered to be 0.5 here, and $t = \tilde{t}\omega$ is the non-dimensional time with $\omega = \sqrt{\frac{E_0 I}{\rho b h L^4}}$ and $\eta = \omega_f/\omega$ is the non-dimensional

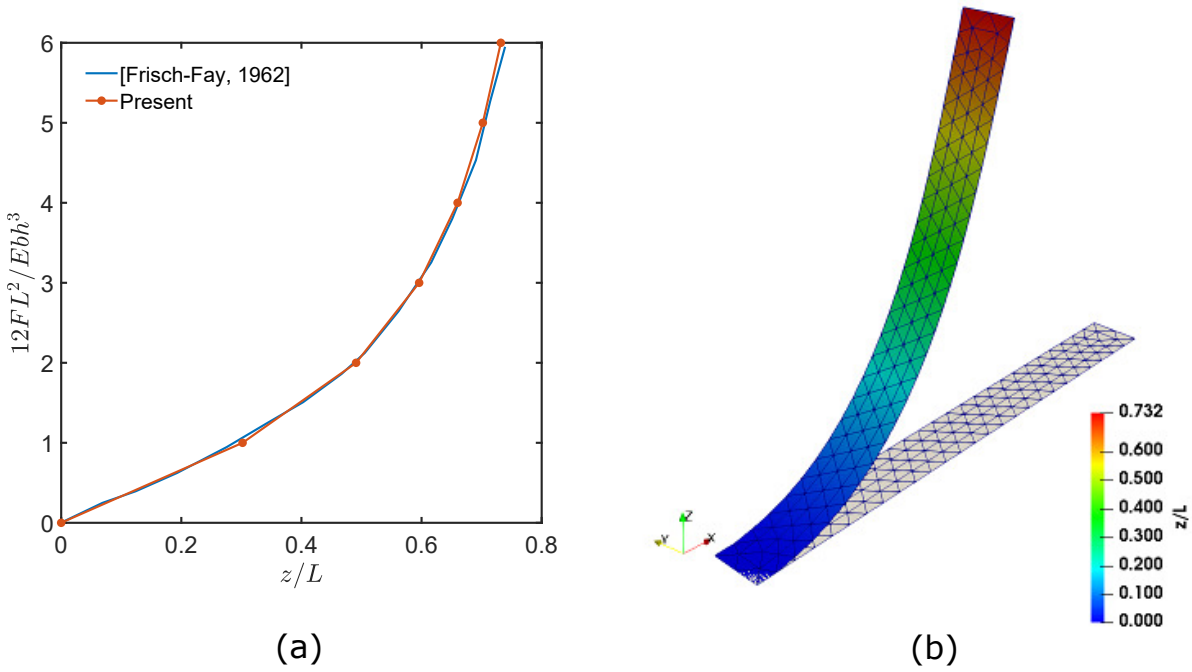

Figure 3.6: A cantilever under concentrated tip force with $L = 0.04m$, $b = 0.004m$, $h = 6 \times 10^{-4}m$, $E = 2 \times 10^5 N/m^2$, and $\nu = 0$; (a) comparison of tip displacement with analytical solution [3] and (b) reference and deformed shape of the cantilever for $F = 5.4 \times 10^{-5}N$.

frequency of the applied force. Here, I, ρ, b, and h are the second moment of area, density, width, and thickness of the beam, respectively. Therefore, the Euler-Bernoulli beam equation [87] in non-dimensional form for a beam with the aforementioned material property becomes:

$$\frac{\partial^2}{\partial x^2}[(1+x^2)\frac{\partial^2 W}{\partial x^2}] + \frac{\partial^2 W}{\partial t^2} = f(x,t) \tag{3.4}$$

The force is manufactured by substituting equations 3.2 and 3.3 into equation 3.4 as:

$$f(x,t) = a(4 - x^2\eta^2)cos(\eta t) \tag{3.5}$$

Consequently, the dynamic force (equation 3.5) with the given dynamic displacement (equation 3.3) and the non-linear material property (equation 3.2) satisfy the governing equation 3.4, i.e, the given displacement (equation 3.3) is the analytical solution when a dynamic force based on equa-

tion 3.5 is applied to a cantilever beam with a non-linear material property according to equation 3.2. To test our method, therefore, the dynamic force (equation 3.5) is exerted on a cantilever with non-linear material property (equation 3.2) and the displacements are calculated using our method and compared against the analytical solution (equation 3.3).

In this example, a small amount of dissipation was applied to stabilize the numerical simulation and a zero Poisson ratio was considered. The quasi-steady displacement of the tip of the cantilever, which is excited with a frequency of $\eta = 1.9$ is compared to the analytical solution in figure 3.7.

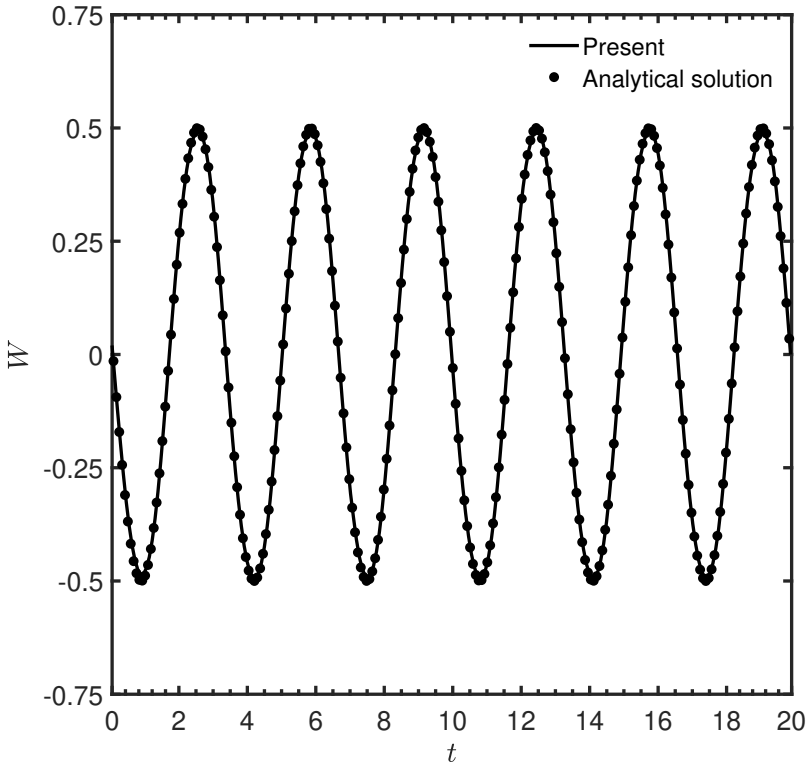

Figure 3.7: The displacement of the tip of the cantilever with nonlinear material property is subjected to dynamic force.

3.2.6 Stretched Cylindrical Shell with Free Ends

The pinched cylinder is a widely used benchmark that tests the framework's ability to simulate large bending deformations and complex membrane states. A cylindrical shell with the length of $L = 10.35m$, the radius of $R = 4.953m$, and thickness of $h = 0.094m$ is stretched with two opposite diametrical point loads P acting on the middle of the cylinder length. The cylinder is made of 1600 grid points and has Young moduli of $E = 10.5 \times 10^6 N/m^2$ and the Poisson ratio of $\nu = 0.3125$ and its edges are free. In figure 3.8 (a), the load-displacement curves for points A, B, and C (see figure 3.8 (b)) are compared against Abaqus S4R element results [4], which demonstrates good agreement. Figure 3.8 (c) shows the deformed shape of the cylinder for stretching forces of $P = 4 \times 10^4 N$.

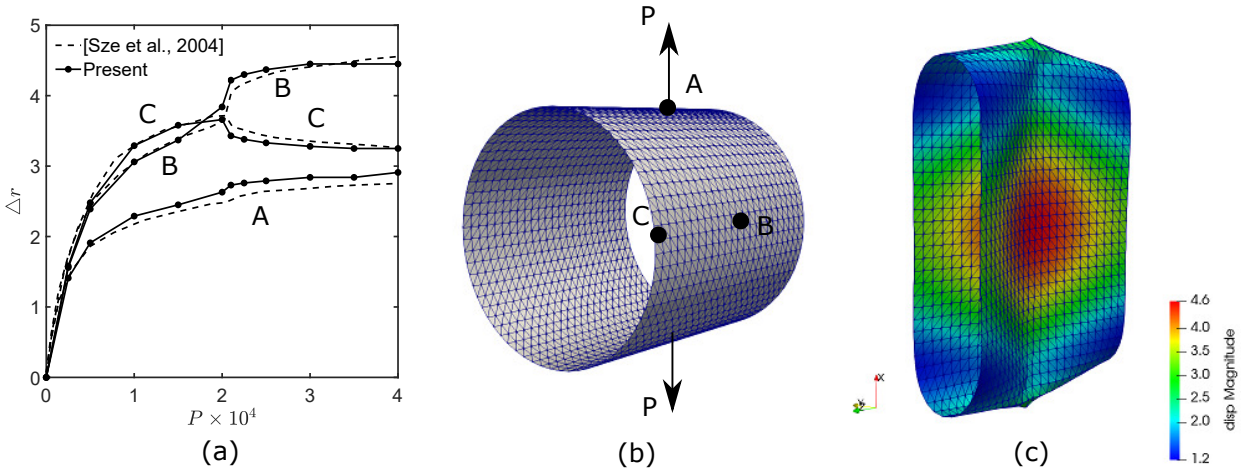

Figure 3.8: A cylinder under pinched loadings with $L = 10.35m$, $R = 4.953m$, $h = 0.094m$, $E = 10.5 \times 10^6 N/m^2$, and $\nu = 0.3125$; (a) comparison of the displacement of three points of the cylinder with numerical results [4], (b) the reference shape, and (c) deformed shape under stretching forces of $P = 4 \times 10^4 N$.

3.2.7 Pinched Hemispherical Shell

In order to test the framework's ability in simulating high bending-dominated deformations by forces applied on the boundaries, a hemispherical shell with a 18^o open hole and free boundaries,

discretized with 1224 grid points, is considered (figure 3.9 (b)). Two pairs of equal and opposing forces $2P$ are imposed diametrically on the equator. The shell has a radius of $R = 10m$, thickness of $h = 0.04m$, elastic moduli of $E = 6.825 \times 10^7 N/m^2$, and Poisson ratio of $\nu = 0.3$. The displacements of nodes A and B (see figure 3.9 (b)) under different loadings P are compared with the numerical results [5] in figure 3.9 (a). Note that since a quarter of the hemisphere is modeled in the simulations of Simov et al.[5], while we modeled it completely, we have applied $2P$ forces instead of P on the edges. The deformed shape of the shell for pinching forces of $P = 100N$ is illustrated in figure 3.9 (c).

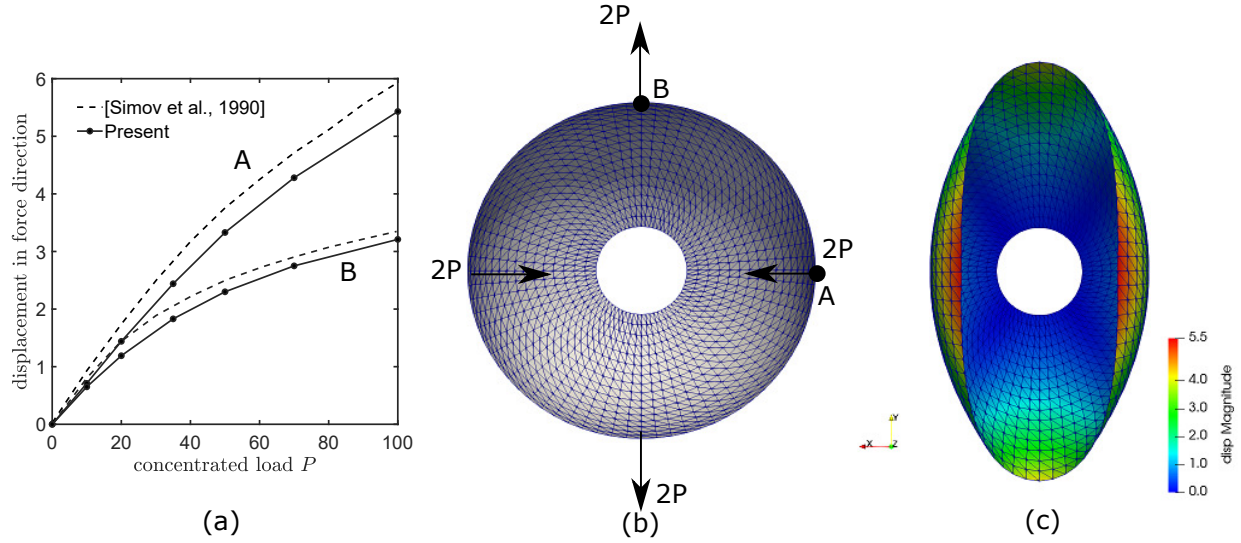

Figure 3.9: A hemispherical shell subjected to two pairs of pinching forces with $R = 10m$, $h = 0.04m$, $E = 6.825 \times 10^7 N/m^2$, and $\nu = 0.3$; (a) comparison of displacement of two points of the hemisphere with numerical results [5], (b) the reference shape, and (c) deformed shape under pinching forces of $P = 100N$.

3.3 Contact Model Validations and Verifications

In this section, a series of validation and verification studies are reported specifically for the proposed contact handling method, in addition to the standard thin shell benchmarks, which are presented in §3.2. In §3.3.1 and §3.3.2, sphere-plate impact under gravitational force and sphere-

sphere impact with initial velocities test cases are performed to investigate the contact area and energy conservation, respectively. The self-contact feature of the contact method is illustrated in §3.3.3 by simulating the collapse of a hemispherical shell under gravity. In §3.3.4, static simulations of a BHV with material nonlinearity and anisotropy are compared against experimental data, which verifies the proper contact modeling of leaflet free edges in the fully closed position. Finally, in §3.3.5, dynamic simulations of the same BHV under physiological pressure waveform are presented for two different fiber orientations.

3.3.1 Sphere-plate Impact under Gravitational Force

In this benchmark, two shell structures subjected to gravitational force impact on each other, with a gravitational acceleration of $980.665m/s^2$. A sphere with a radius $0.125m$ is initially positioned over a circular plate of radius $0.35m$ (figure 3.10(a)). The edges of the circular plate are pinned and the impact is assumed to be inelastic with restitution coefficient $e = 0$. Both of the shell structures have linear material properties with $E = 2.1 \times 10^5 N/m^2$ and $\nu = 0.3$. The sphere has density of $\rho = 10kg/m^3$ and thickness of $h = 0.03m$, while the plate density and thickness are $\rho = 1kg/m^3$ and $h = 0.003m$, respectively. As it is clear from figure 3.10(b), due to the higher density and thickness of the sphere, it is more resistant to bending and the plate undergoes high deformation when reaches to steady state.

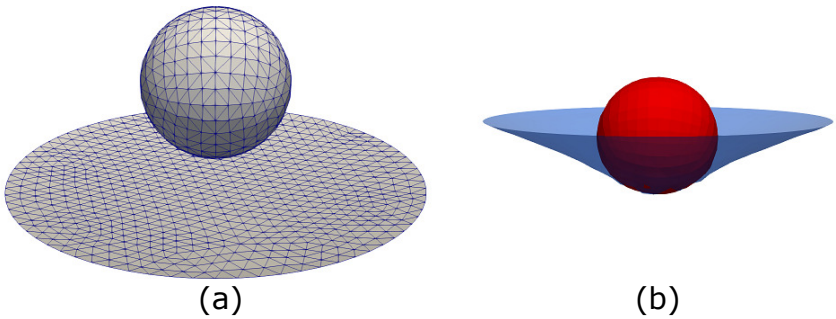

Figure 3.10: The sphere-plate shell structures are subjected to a gravitational force at (a) initial condition and (b) steady state.

Given the fact that the target application of the suggested contact model is in heart valve analysis, the coaptation area, i.e., the area of the contact, is an important parameter. Our calculations for a plate and sphere mesh of 761 and 386 grid points, respectively, show a coaptation area of $0.067m^2$ after reaching steady state, which is in $\%4$ difference with the numerical results of Kamensky et al. [88].

3.3.2 Sphere-sphere Impact with Initial Velocities

In order to investigate the energy conservation of the method, the elastic impact ($e = 1$) of two shell spheres are considered, each consisting of 1538 grid nodes (figure 3.11). Both spheres have radius of $R = 1m$, thickness of $h = 0.09m$, Young's modulus of $E = 10^5 N/m^2$, Poisson's ratio of $\nu = 0.3$, and density of $\rho = 0.1kg/m^3$. A time-step size of $5 \times 10^{-6}s$ has been used for this simulation. Prior to the impact, as a first test case, the spheres on the right and left are considered to have initial velocities of $-20m/s$ and $20m/s$ in the horizontal direction, respectively (identical momentum). In order to show the Independence of energy conservation from the momentum of the spheres, two additional test cases are studied. For the second case, the velocity of the right sphere is set to two times that of the left sphere ($u_2 = 2u_1$) such that the total initial energy of the system is kept similar to case 1. For the third case, the density of the right sphere is considered to be three times of that of the left sphere ($\rho_2 = 3\rho_1$) with the same velocities as test case 1, such that the total initial energy of the system remains the same as case 1.

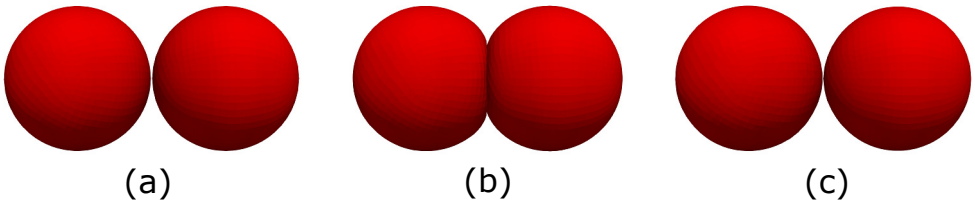

Figure 3.11: Sphere-sphere impact of test case 1 at times (a) 0, (b) 12.5, and (c) 25 ms .

The kinematic, internal, and total energies of the system of spheres are plotted during the

impact in figure 3.12 for all three test cases. It is clear that a significant ratio of kinetic energy is converted to internal energy during the impact, which is illustrated as the high deformation of spheres for test case 1 in figure 3.11(b). The total energy of the system remains constant during the impact with a slight change by $\%3$, which could be because of the application of impenetrability condition; therefore, the proposed contact method preserves the energy with acceptable precision.

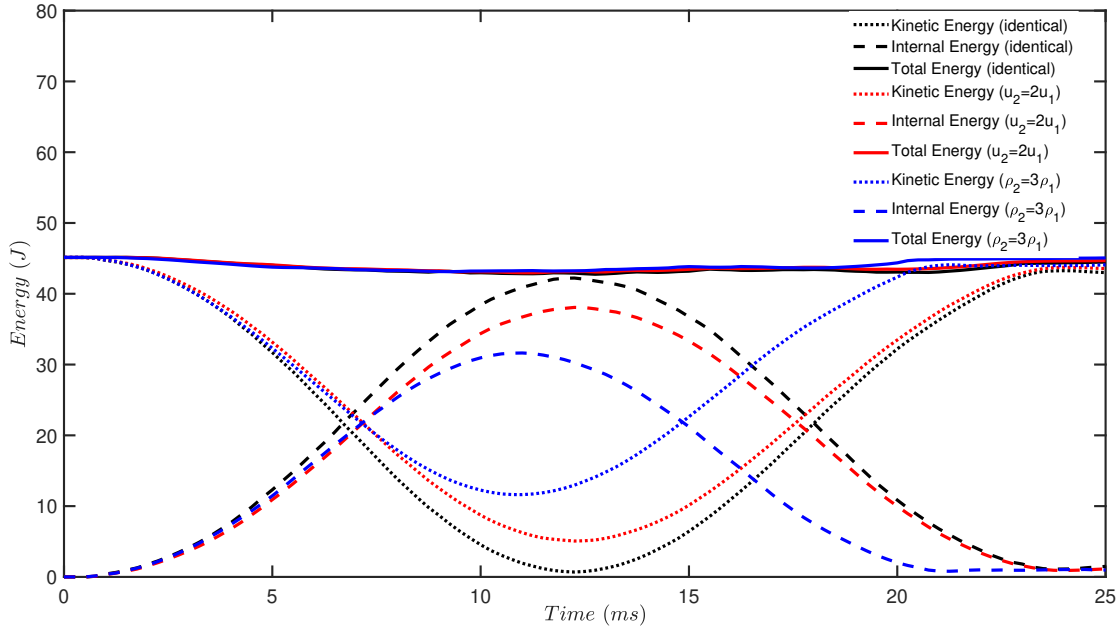

Figure 3.12: Energies of the system for elastic sphere-sphere impact.

3.3.3 Self-contact of Hemispherical Shell under Gravitational Force

The inclusion of the bounding spheres in the search algorithm makes the framework capable of simulating simple self-contact problems, where only the outer side of the shell surface comes to contact with itself in multiple locations. For this purpose, a hemispherical shell consisting of 5645 grid points with radius of $R = 1m$, thickness of $h = 0.03m$, Young's modulus of $E = 10^4 N/m^2$, Poisson's ratio of $\nu = 0.3$, and density of $\rho = 10kg/m^3$ is draped from its highest point (figure 3.13(a)), which falls under gravitational acceleration of $g = 9.81m/s^2$. Figures 3.13(b) and (c)

show the three-fold deformed shape of the shell after reaching steady state, illustrating three main contact areas of the shell with itself.

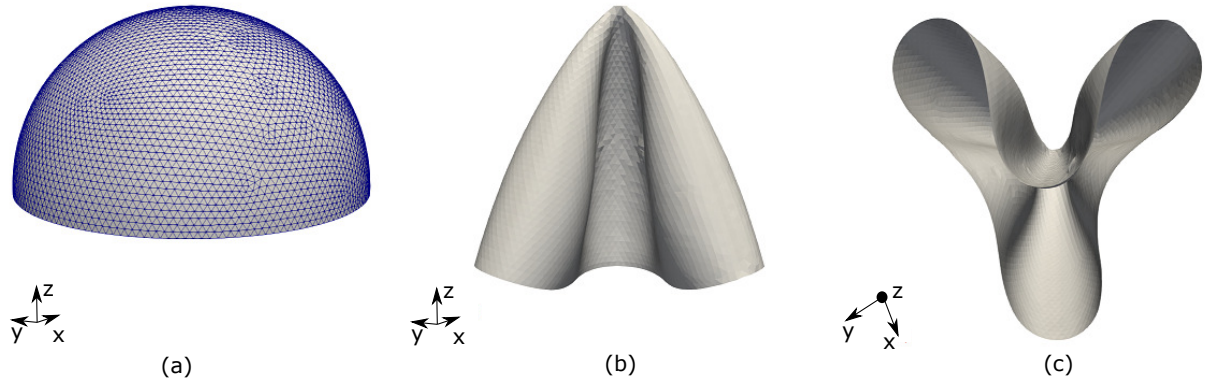

Figure 3.13: Self-contact of a hemispherical shell under gravity; (a) reference shape, (b) deformed shape from a side angle, and (c) deformed shape from the bottom view.

3.3.4 Static Pressure Loading of a Pericardial BHV

In this subsection, we have compared our results with the experimental results of the pericardial BHV of Kim et al. [6], geometry of which is shown in figure 3.14 (a), illustrating three regions of interest: (1) leaflet attachment boundary, (2) central free edge, and (3) belly. The thickness of the leaflets is 0.386 mm and the BHV has a radius and height of 11.5 and 10.9 mm, respectively. The surface of each leaflet is discretized using a triangular mesh with 1049 grid points. The material model of Kim et al. [6] (see §2.2.3) with a typical bovine pericardial asymmetrical preferred fiber direction [89] of 45^o relative to the cross product of $\mathbf{z}$ and $\mathbf{a}_3$ ($\mathbf{z}$ is the axial direction and $\mathbf{a}_3$ is the element normal) is utilized for the simulations (figure 3.14 (b)).

First, the deformation of the leaflets under static pressures of 40, 80, and 120 mmHg are considered. The results show that the displacement from the rest condition (zero pressure) to 40 mmHg is significantly larger than the 40 to 80 and 80 to 120 mmHg. The results are qualitatively similar to experimental data [6], which illustrates that the proposed contact modeling method provides phys-

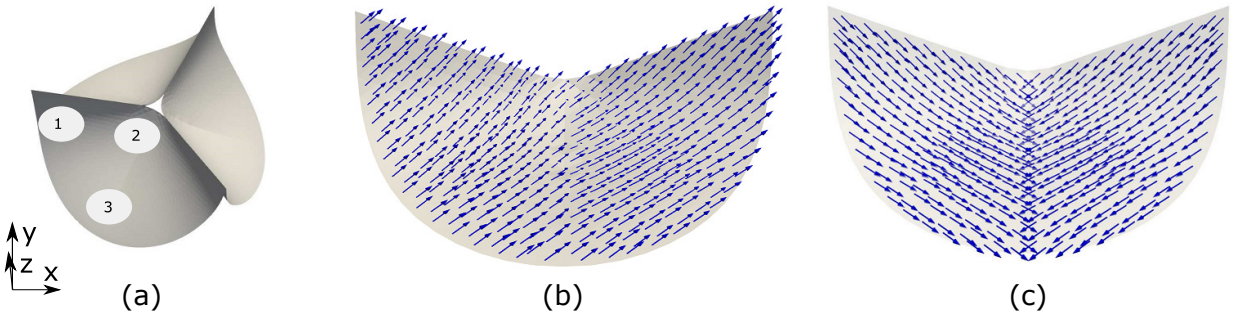

Figure 3.14: The pericardial BHV geometry. The reference shape with three regions of interest: (1) leaflet attachment boundary, (2) central free edge, and (3) belly. The fiber direction of leaflet, shown in arrows, for (b) asymmetrical and (c) symmetrical 45^o relative to the cross product of $\mathbf{z}$ and $\mathbf{a}_3$. Here $\mathbf{z}$ is the axial direction and $\mathbf{a}_3$ is the element normal.

ical results since proper modeling of the contact area is required for calculating the displacements of the free edges.

The average major and minor in-plane Green-Lagrange principal strains of three primary regions of leaflets (see figure 3.14(a)) with two grid resolutions are compared with experimental data in figure 3.15. The results show that by refining the grid from the coarse grid, with 277 grid points, to the fine grid, with 1049 grid points, the principal in-plane strains converge to the experimental values. Given the fact that there is no precise definition of the regions of the leaflet and possible discrepancy between the fiber direction in experiments and numerical simulations, the results with the fine mesh follow the experimental data with an acceptable margin.

3.3.5 Dynamic Simulation of a Pericardial BHV

Dynamic simulation of the BHV is performed by applying physiological transvalvular pressure difference between left ventricle and aorta for the complete human cardiac cycle [7] (figure 3.16). The same spatial discretization of §3.3.4 and material model of §2.2.3 are utilized with a material density of $1100\ kg/m^3$ and temporal time step size of $0.1\ ms$ over the full cardiac cycle of $760\ ms$. In order to investigate the effects of fiber orientation in the overall dynamic of the valves, two asymmetrical and symmetrical 45^o fiber directions are employed, which are shown in figures 3.14(b) and 3.14(c), respectively.

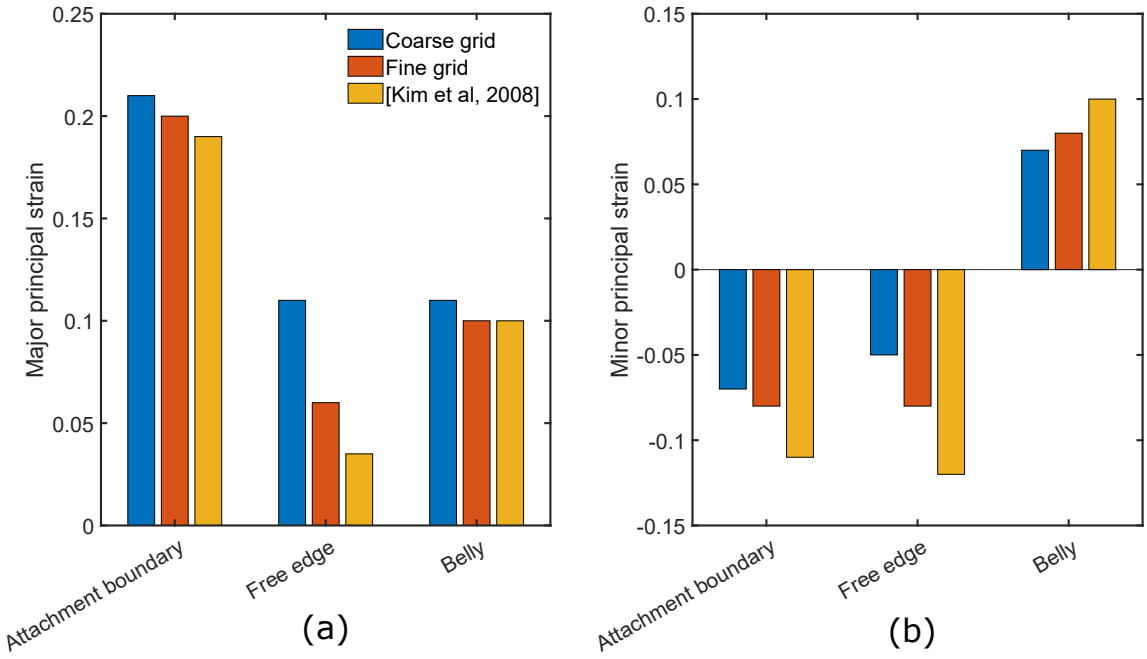

Figure 3.15: Comparison of the average in-plane principal Green-Lagrange strains of the present study with experimental results of Kim et al. [6]: (a) major principal strains and (b) minor principal strains.

The closing phase of BHV is a critical phase for contact handling due to the high acceleration movement of the leaflets imposed by the surge in transvalvular pressure difference. The new contact model with a restitution coefficient of $e = 0$ during high acceleration movement of BHV closing phase ($t = 0.203s$) is compared to the penalty method in figure 3.17 for an asymmetrical fiber orientation. The penalty method uses predefined forms of contact force ($\mathbf{F}_{cnt}$), which may be applied to the node contacting an element in the direction of the element normal, e.g., using [90]:

$$\mathbf{F}_{cnt} = \begin{cases} |\mathbf{F}_{ext}| e^{-kd/|\mathbf{F}_{ext}|} & \text{if} \quad d > 0 \\ |\mathbf{F}_{ext}| - kd & \text{if} \quad d \leq 0 \end{cases} \tag{3.6}$$

where d is the perpendicular distance between the node and the element (with positive values on the side of element normal), k is the contact stiffness, and $\mathbf{F}_{ext}$ is the external force acting on the node. This comparison illustrates the capabilities of the proposed method in creating a zero gap

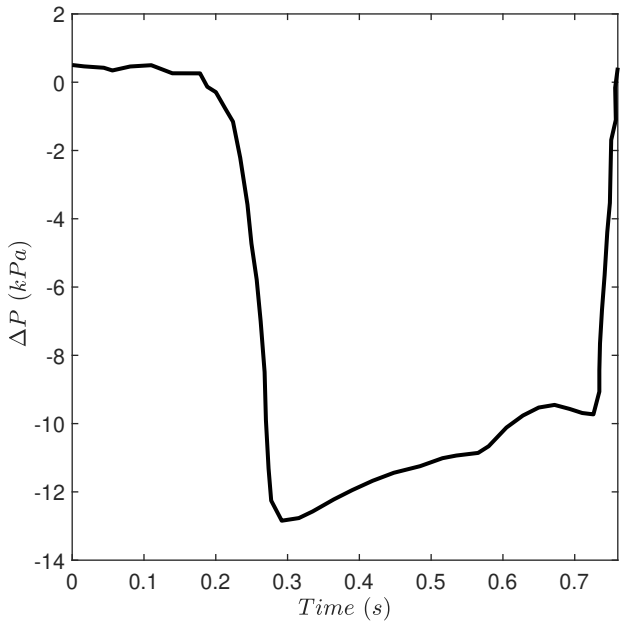

Figure 3.16: The transvalvular pressure difference between left ventricle and aorta for complete human cardiac cycle [7] applied to the leaflets.

between the leaflets while generating smooth edges. It is evident from figure 3.17 (b) that the penalty method fails to keep a constant gap between the leaflets, creating nonsmooth edges, which in some regions the edges fold up around each other. Note that determining the coefficients for the penalty method is ad hoc and after trying different values, the performance of the penalty method is not nearly as good as the new contact method, which does not require experimentation.

In order to test the robustness of the contact handling, sequences of displacement of the BHV model are illustrated in figures 3.18 and 3.19 for the opening and closing phases of a complete cardiac cycle, respectively, colored by major in-plane principal Green-Lagrange strain (MIPE) with symmetrical and asymmetrical fiber directions. We use damping to model the viscous and inertial resistance of the surrounding fluid. The value of $C = 0.06\ gr/s$ is chosen so that the valves open at a physiologically reasonable time. The opening phase is qualitatively similar to the computations of [6, 67, 24] in timing of the opening. Our results show more clearly that during the opening phase, commissure and central free edge regions (marked as regions 1 and 2, respectively,

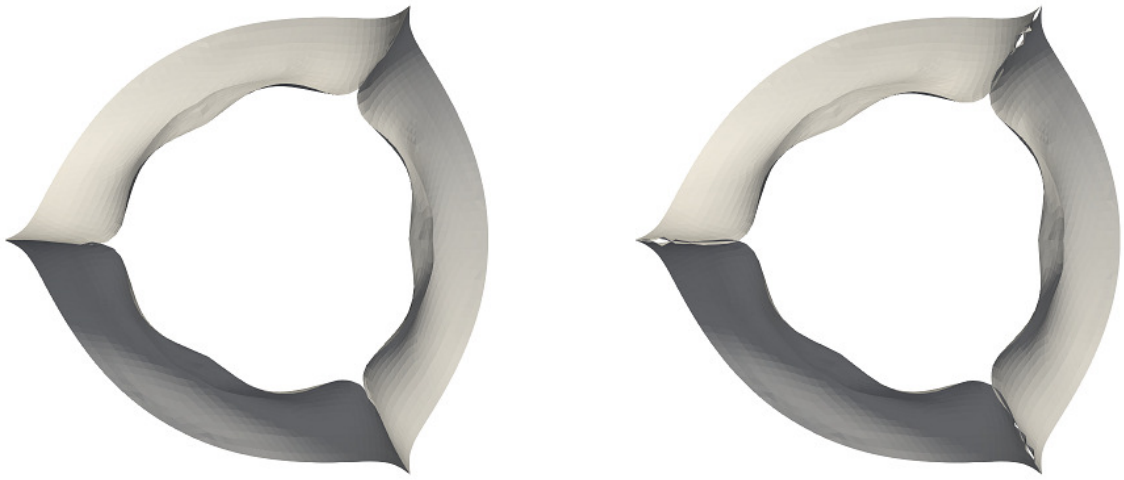

Figure 3.17: Contact of Leaflets during closing phase of BHV ($t = 0.203s$) with contact handled using (a) new and (b) penalty methods. An asymmetrical fiber orientation of 45^o is considered for both methods.

in figure 3.14(a)) show high values of MIPE as the leaflets stretched out ($t = 0 - 0.04s$ in figure 3.18). Nevertheless, the values of MIPE in the commissure region are several folds larger than the central free edge region. This is not directly visible in figure 3.18 due to the color legend chosen to show the distribution of data for most of the time instants. The top-view of valve deformations in figure 3.18 at $t = 0.04s$ also show that fiber direction affects the opening of the valve in a way that valve with asymmetrical fiber orientation (typical bovine pericardial fiber orientation) bends its edge consistently over all of the free edges, in contrast to the valve with symmetrical one where only the commissures region bends backward while the central part of the free edge remains straight. Overall the fiber direction does not show to have a major effect on the MIPE distribution on the leaflets; however, for the late time steps of the opening phase ($t = 0.04s$) the valve with asymmetrical fiber orientation shows lower values of MIPE compared to the symmetrical one.

During the closing, as can be observed in figure 3.19, the results of both fiber directions are generally similar to computations of Kim et al. [6] in a sense that first the commissures of the leaflets come to contact with each other and then coaptation area extends to the central parts of

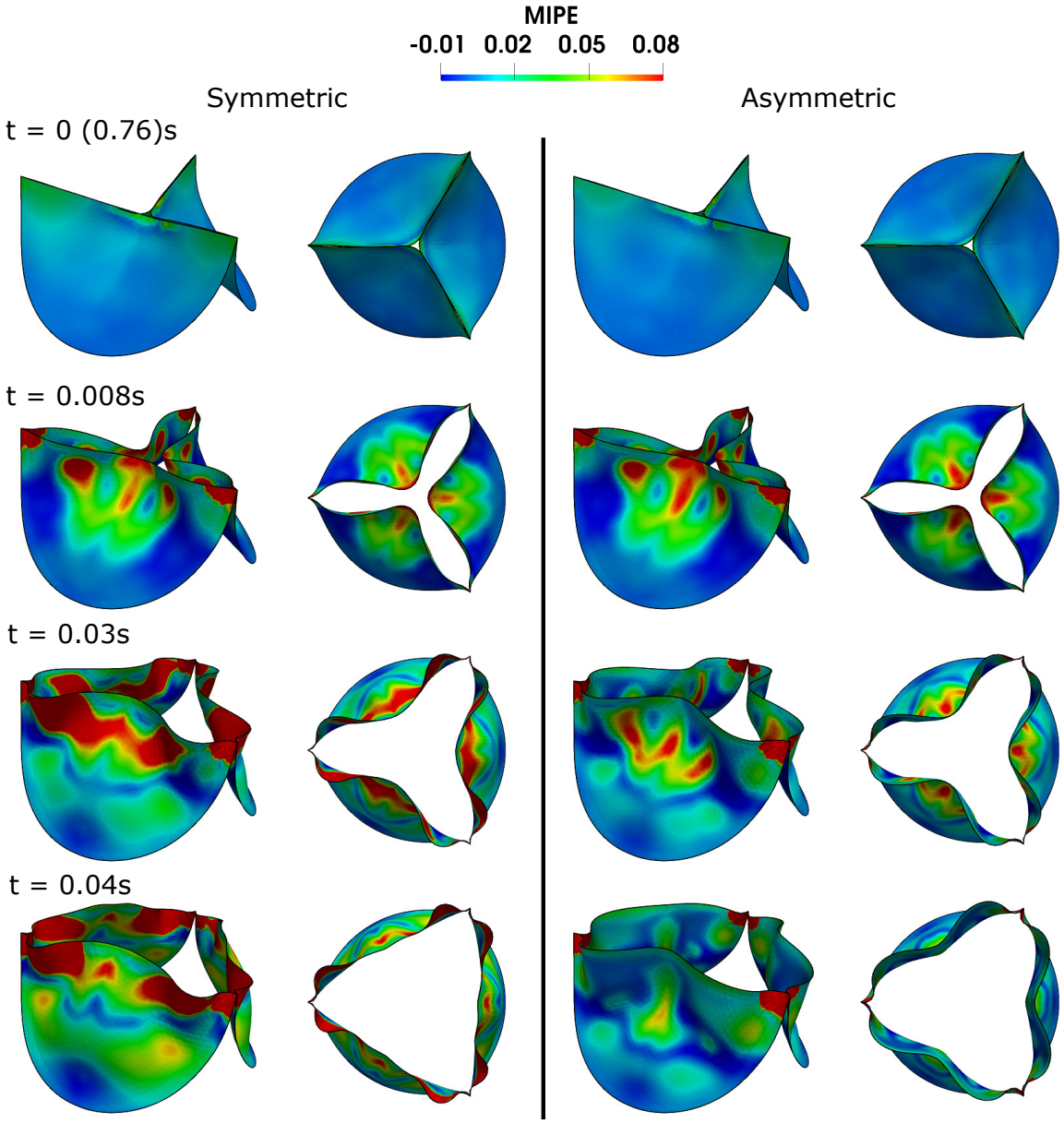

Figure 3.18: Deformations of the BHV during the opening phase of a cardiac cycle, colored by major in-plane principal Green-Lagrange strain (MIPE) for symmetrical (column 1) and asymmetrical (column 2) fiber directions at 4 time instants from the side and top views. The initial condition $t = 0$ is taken from preceding cycle ($t = 0.76s$).

the leaflets edge. This similarity might be due to the same material model employed; however, our results do not show any wrinkles along the free edges. The effects of fiber orientation on the closing of the valves becomes evident during the late closing phase ($t = 0.21s$ in figure 3.19). The

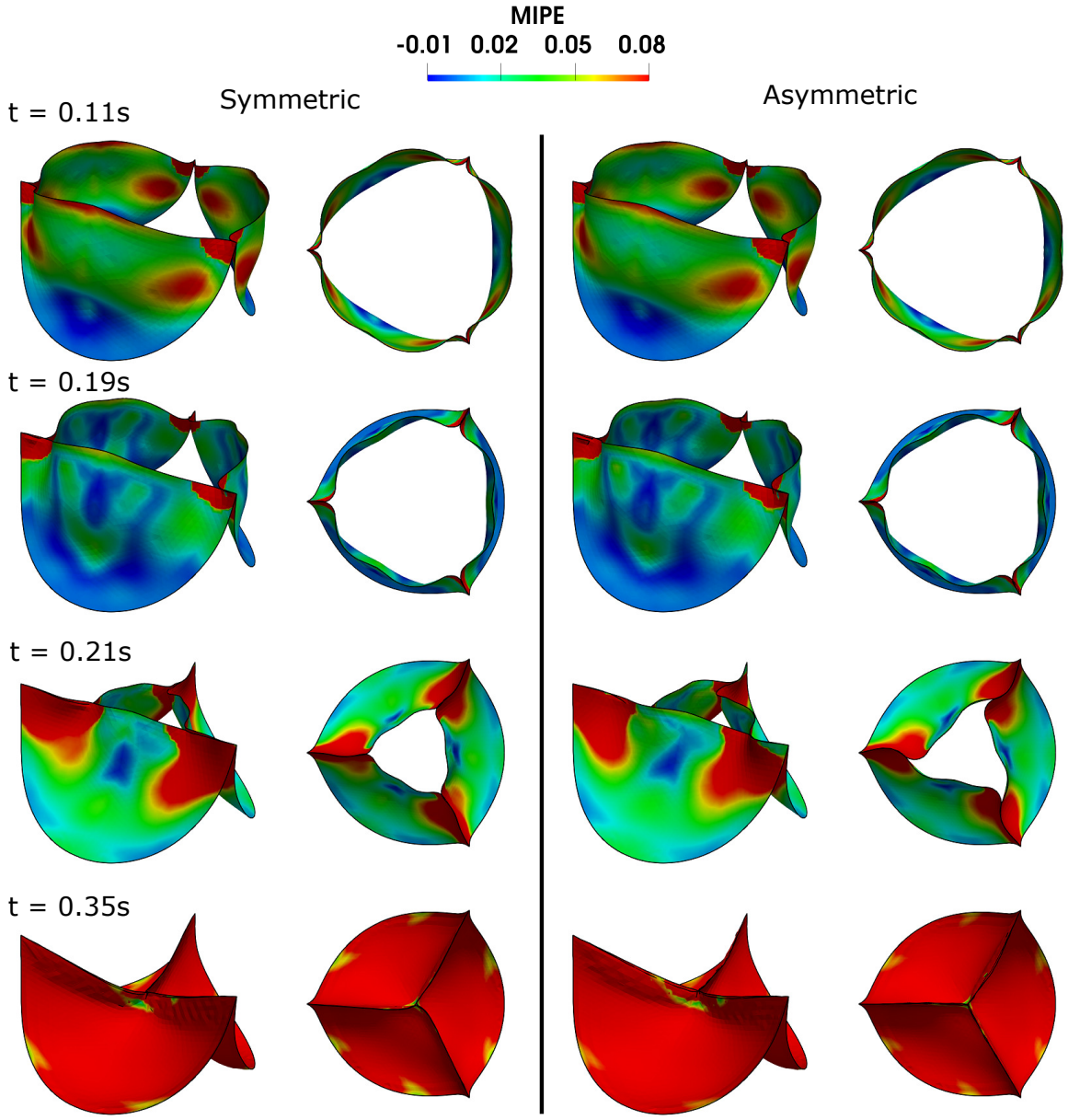

Figure 3.19: Deformations of the BHV during the closing phase of a cardiac cycle, colored by major in-plane principal Green-Lagrange strain (MIPE) for symmetrical (column 1) and asymmetrical (column 2) fiber directions at 4 time instants from the side and top views.

valves with typical fiber orientation (asymmetrical) show a swirling motion, similar to experimental results of Lee et al.[91]. The closing phase of other simulations [67, 24] are different in pattern, which might be due to the different material models and shows their importance especially during the closing phase [92]. In addition, due to exponential stiffening of the material model, our results

do not show the sagging of the belly region, compared to linear material models [24] during the fully closed position. During the cycle, the highest concentration of MIPE is seen in commissures, which is in agreement with the known failure regions of a BHV [93]. During the fully closed phase, the coaptation area is about 32% of the leaflet area, which is in the clinical range of a functioning BHV [94]. This indicates that the proposed contact handling method, not only is generic for different configurations and provides wrinkle-free edges but also provides physical results with regards to coaptation area.

3.4 Finite Element Fluid-structure Interaction Validation

The validation and verification studies addressed in §3.1 include the FSI simulations combining CURVIB flow solver with an immersed rigid body. In order to gauge the accuracy of the newly developed FE-CURVIB FSI coupling, a challenging benchmark problem is chosen. In §3.4.1, a high deformation vibration of a deformable flag, known as inverted flag, is studied, which undergoes cyclic displacements in a flow with high Reynolds number. By comparing the numerical results of this test case with the experimental data, the validity of the coupled FE-CURVIB framework is established.

3.4.1 Flapping of an Inverted Flag

In this validation study, which is based on the experimental data of Kim et al. [8], a square flat thin shell with length of $L = 0.3m$ and thickness of $h = 8 \times 10^{-4}m$ is considered, which is fixed on its trailing edge and free on the other edges. It is exposed to oscillations due to a uniform inflow of velocity $U_\infty = 6.7m/s$, as shown in figure 3.20. The background fluid domain boundary conditions for the side, top, and bottom walls in figure 3.20 (X and Y direction) are no-slip condition ($\mathbf{V} = 0$). In Z direction, the Dirichlet boundary condition of $\mathbf{V} = U_\infty k$ and Neumann boundary condition of $\partial \mathbf{V}/\partial Z = 0$ are applied on the left and right walls, respectively. The Young's modulus, density, and Poisson's ratio of the flag are set to $E = 2.38 \times 10^9 Pa$, $\rho_s = 1200kg/m^3$, and $\nu = 0.38$, respectively, while the fluid's density is $\rho_f = 0.98kg/m^3$. According to the experimental data [8], these values of fluid and structure features places the flag motion into dynamically

rich "flapping mode", which is characterized by high amplitude cyclic oscillations with multiple local maxima and minima of flag's leading edge displacement. Additionally, the corresponding Reynolds number based on inflow velocity and flag length is $Re = U_\infty \rho_f L/\mu = 99500$ (for a fluid viscosity of $\mu = 1.92 \times 10^{-5} Pa.s$), which causes the separated flow in the wake of the flag to be completely turbulent; therefore, it requires a turbulence modeling to accurately simulate the flow. Consequently, the FE-CURVIB FSI framework is supplemented with LES modeling, using dynamic Smagorinsky subgrid scale model [95] for closure and Cabot wall function [96] for boundary condition reconstruction on the immersed body, as adopted by Kang et al. for CURVIB method [97, 98]. Here, the flag is discretized using triangular mesh with 141 grid points, while the background fluid mesh is $53 \times 53 \times 141$ uniform Cartesian grid in X, Y, and Z directions, respectively. The non-dimensional time step size of 0.01 is used.

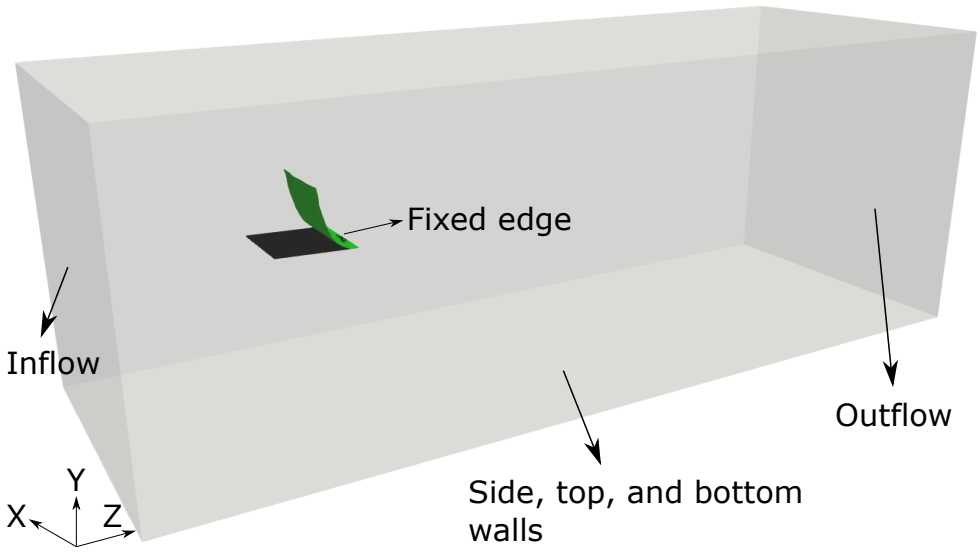

Figure 3.20: A 3-D view of the computational domain for the inverted flag benchmark. The shaded and green sheets show the inverted flag position in initial and representative deflected states, respectively. The boundary conditions for the side, top, and bottom walls (X and Y direction) are no-slip condition ($\mathbf{V} = 0$). In Z direction, the Dirichlet boundary condition of $\mathbf{V} = U_\infty k$ and Neumann boundary condition of $\partial \mathbf{V}/\partial Z = 0$ are applied on the left and right walls, respectively.

The leading edge deflection of the inverted flag is computed and compared against experimental data of [8] in figure 3.21. It is clear that the implemented FE-CURVIB FSI framework captured the complex dynamics of the inverted flag, which includes multiple minima (near maximum deflection) and maxima (near minimum deflection). The computed leading edge deflections after reaching quasi-steady state show a maximum of 8% and 9% error in the amplitude and frequency compared to the experimental data [8]. In order to compare the exerted forces of the flow over the flag, the drag coefficient ($C_D = F_D/F_0$) is calculated by normalizing the force in Z direction (F_D) with $F_0 = \rho_f U_\infty^2 L^2/2$. The quasi-steady state calculations show a maximum drag coefficient of 2 and an average drag coefficient of 1, which is in excellent agreement with the experimental data [8].

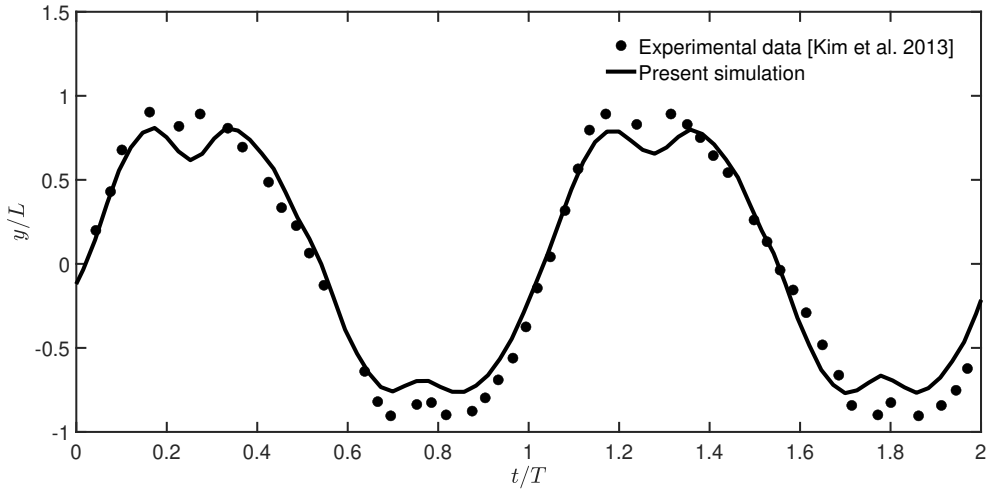

Figure 3.21: Time history of the computed leading edge deflection of the inverted flag against experimental data of [8].

The three-dimensional vortical structures of the flow over the inverted flag are shown in figure 3.22 using iso-surfaces of Q-criterion [9]. These snapshots, as expected, illustrate a highly separated flow over the flag after reaching the quasi-steady state. The vortex tubes shed from the two sides of the flag (figure 3.22(a)) become intertwined and twisted, while the leading edge vortical arch evolves (figure 3.22(b)). The instabilities of the side vortex tubes intensify and progress to-

ward the leading edge vortex (figure 3.22(c)), which causes intermittent vortex shading from the sides as shown in figure 3.22(d). By the breakdown of these structures in the wake, the flow becomes dominated by small-scale turbulent structures (figure 3.22(e)), which persist until the flag reaches the initial position (figure 3.22(f)).

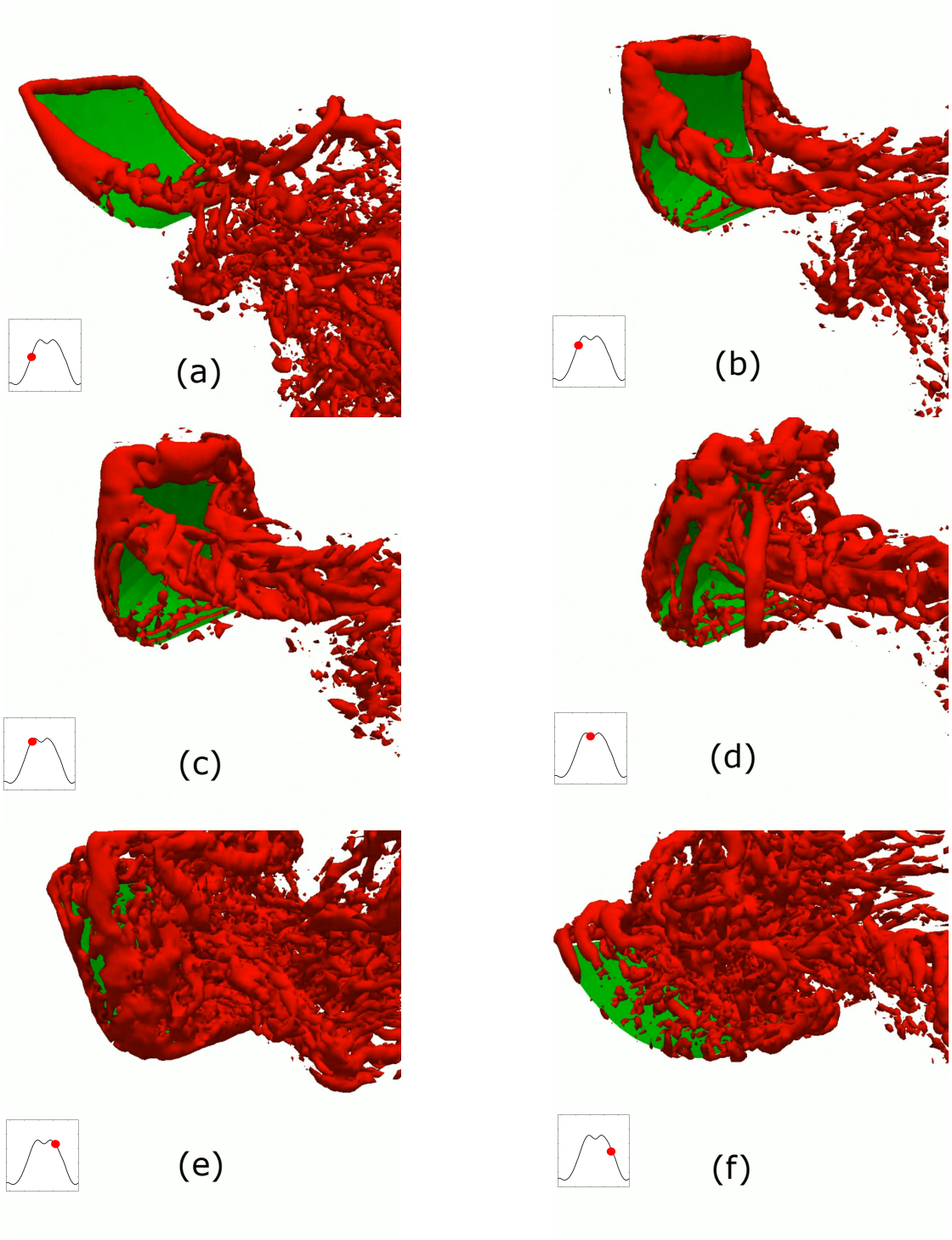

Figure 3.22: Three-dimensional vortical structures visualized using Q-criterion [9] for different time instants after reaching quasi-steady state. The red dots in the insets show the corresponding time during the cycle.

4. VORTEX DYNAMICS OF PERIODICALLY GENERATED VORTEX RINGS[1]

The purpose of this chapter is to investigate the periodic vortex rings in order to better understand their dynamics in cardiovascular flows such as seen around BMHV and BHV. Therefore, we proposed a scaling law for the time tracking of core centers of vortex rings. Such a relation for periodically generated vortex rings, which accounts for all the potentially important parameters, i.e., Reynolds number, period (formation time), and stroke ratio of the waveform, is missing in the literature, to the best of the knowledge of the author. To do so, after a brief introduction in §4.1, we carry out numerical simulations of vortex rings in a tank using our framework described in §2.1. We discuss the simulated test cases in §4.2. An application-specific validation study is performed for our framework in order to capture the propagation speed of vortex rings in §3.1.1. We present the results of the dynamics of periodic vortex rings in §4.3 and their propagation in §4.4. The discussion and conclusions are presented in §4.5 and §4.6, respectively.

4.1 Background

Periodically generated vortex rings are regularly observed in nature, e.g., animal propulsion [99, 100, 101, 102, 103, 104] and cardiovascular flows [105, 106, 107]. Many studies have focused on isolated vortex rings, instead of periodically generated ones, to identify the main parameters governing their physics. Glezer [108] utilized two non-dimensional parameters (Reynolds number and non-dimensional stroke time) to build a transition map to predict if a vortex ring would be turbulent upon formation or not. Gharib, Rambod, and Shariff [109] proposed a non-dimensional time, called the formation time and defined as the ratio of the stroke length to the diameter of the cylinder (L/D), to govern the optimum formation of a vortex ring. The vortex rings' circulation grows until formation time of about 4, referred to as formation number, after which the ring cannot grow due to energetic constraints and forms trailing vortices. How these parameters, e.g., Reynolds number or formation time, affect the propagation of a vortex ring, nevertheless, is still not well

[1]This chapter has been published as "H. Asadi, H. Asgharzadeh, and I. Borazjani. "On the scaling of propagation of periodically generated vortex rings," *Journal of Fluid Mechanics*, vol. 853, pp. 150-170, 2018."

quantified.

Several studies have discussed the propagation of isolated vortex rings. For short times after the formation of vortex rings, Didden [110] experimentally showed that the non-dimensional axial locations of vortex core centers for two relatively low Reynolds numbers are proportional to non-dimensional time powered by 1.5. He also suggested similar scaling law with different power for radial location of vortex core centers and observed a linear increase in total circulation during most of the formation process, which were later verified numerically by Nitsche and Krasny [111] and James and Madnia [112], separately. Baird [113] experimentally showed that for sufficiently large orifice diameters, velocity of the vortex ring near the formation region is approximately half of the jet mean velocity for high Reynolds numbers, which was later verified by a formula suggested by Mohseni [58]. Baird [113] also concluded that the jet injection time interval (formation time) does not affect the vortex ring velocity. However, later, Sullivan et al. [86] by an empirical method showed that vortex core velocity is approximated by 0.3 of piston velocity. Saffman [114] derived an equation for a thin vortex ring's velocity in viscous flows, where the effect of viscosity is to slow down the ring after long time. He assumed circular core for the vortex rings, which is not a valid assumption for cases with high formation times. In this equation, similar to classical Kelvin formula for circular vortex rings [115], the diameter and circulation of the vortex ring are required for calculating its velocity. His work was later extended by fukumoto and Moffatt [116] to a higher order asymptotic formula, which accounts for core deformations at high Reynolds numbers; however, this formula needs several numerical integrations. Maxworthy [57] experimentally studied the slowing of vortex rings and showed that the propagation velocity of a stable laminar vortex ring decays exponentially with the distance from the origin and varies as $1/t$, where t is time, for long times. Gan and Nickels [59] showed a similarity theory holds for isolated vortex rings at two high Reynolds numbers. Based on the above review, most studies consider isolated vortex rings to propagate at constant speed except during early formation [110] or decay after long times [57]. Nevertheless, how the constant speed is affected by Reynolds number or formation time is not well described yet. In addition, the interaction between vortices for a periodically generated train of

vortices may change the velocity of vortex cores [117].

Several studies have investigated the propagation of periodically generated rings. Aydemir, Worth, and Dawson [118] studied vortex rings for periodically initiated and terminated jets, and showed that spacing between consecutive rings depends on both frequency and amplitude of inflow waveform. Krueger [119] found that by decreasing the period of the inflow, the velocity of vortex rings reduces and approaches to an isolated vortex ring velocity. Schram and Riethmuller [120] studied the interaction of leading and trailing vortex rings with each other and divided it into three stages. They showed that during the last stage, the trailing vortex rolls over the leading one, which leads to an increased vortex core velocity. Zaman and Hussain [121] reported two distinct modes under which vortex ring pairing occurs: 'shear layer mode' for cases with certain values of Strouhal number based on the initial shear layer momentum thickness and 'jet column mode' for cases with specific values of Strouhal number based on jet diameter. They also observed that vortex pairing occurs regularly in space and time at low Reynold numbers, but less regularly by increasing the Reynolds number. Asgharzadeh and Borazjani [60] showed that the propagation of vortex rings in aneurysms increases with increasing the Reynolds number and decreasing the Womersley number. However, a general formula that can quantitatively describe the changes in the propagation of vortex rings as a function of governing parameters, such as Reynolds number, formation time, etc has yet to be reported.

4.2 Computational Details

The computational setup consists of a square tank of size $5.5D \times 5.5D \times 10.5D$ to which a circular cylinder of diameter $D = 72.8\ mm$ and length $2D$ is attached as shown in figure 4.1(a). All test cases have been carried out in a setup similar to [1]. Note that for cases with high Reynolds numbers, the length of the domain was extended to $19D$ to achieve a better convergence. The flow enters the domain through the cylinder, which is placed as an immersed boundary, and leaves it through the boundary across the cylinder as outflow. The no-slip condition is applied on the sidewalls and the wall behind the cylinder. The vortex rings are generated by a pulsed jet with period T as an inflow at the inlet of the cylinder with a profile whose magnitude varies in time

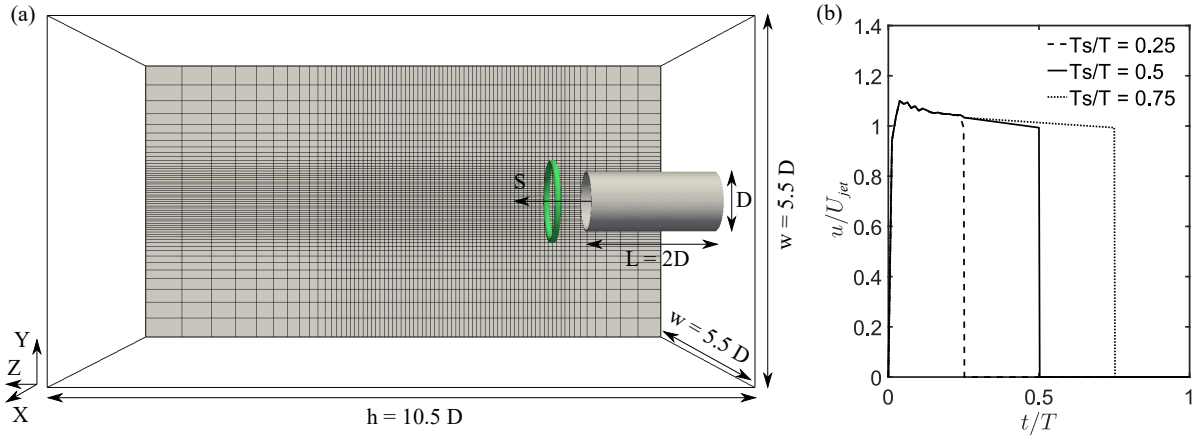

Figure 4.1: (*a*) A 3-D view of domain with generated vortex rings in green and a cross-section of fluid mesh over the tank and (*b*) different inflow velocity waveforms for different test cases. Only every fourth grid point is shown in (*a*) for better illustration.

according to figure 4.1(*b*). These waveforms are adopted from [1] to form a jet pulse for duration T_s (stroke time) and a nominal speed of U_{jet}. There is no flow between pulses. Three different ratios of T_s/T are considered for the inflow velocity (u) waveform (see figure 4.1(*b*)). The characteristic length scale is the diameter of cylinder D. Because of the step-like inflow waveform (figure 4.1(*b*)), the average velocity in each cycle is:

$$U_{ave} = \frac{1}{T}\int_0^T u dt = \frac{U_{jet}T_s}{T}. \tag{4.1}$$

The computational grid consists of $225 \times 225 \times 301$ nodes in X, Y, and Z directions, respectively. Due to longer domain for cases with high Reynolds numbers, 433 nodes were utilized in Z direction. The region of interest is a $1.1D \times 1.1D \times 4D$ cuboid with a uniform spacing of $0.01D \times 0.01D \times 0.02D$, which starts from the exit of the cylinder and is symmetric relative to the mid-plane. The grid was stretched from the cuboid to the outer edges of the computational domain using a hyperbolic tangent function as shown schematically in figure 4.1(*a*). For temporal discretization, a non-dimensional time-step size ($\triangle t U_{jet}/D$) of 0.005 is considered for all the test cases. Therefore, the Courant number for all the simulations is 0.5.

$test\ case$	Re_{ave}	Re_{jet}	T^*_{ave}	T^*_{jet}	T_s/T	α	$(\frac{U_v}{U_{jet}})_{FI}$	$(\frac{U_v}{U_{jet}})_{FE}$	$(\frac{U_1-U_v}{U_v})_{FI}(\%)$
1	2800	2800	-	-	-	-	-	0.29	-
2	23000	23000	-	-	-	-	-	0.30	-
3	1400	2800	1	2	0.5	93.79	0.26	0.30	0.4
4	1400	2800	2	4	0.5	66.32	0.35	0.40	6.6
5	11500	23000	1	2	0.5	268.81	0.28	0.29	2.6
6	11500	23000	2	4	0.5	190.07	0.31	0.35	0.9
7	500	1000	4	8	0.5	28.02	0.5	0.62	10.7
8	500	1000	2.88	5.67	0.5	33.03	0.45	0.57	9.4
9	250	500	2	4	0.5	28.02	0.43	0.57	15.4
10	11500	23000	2.88	5.67	0.5	158.4	0.36	0.4	3.7
11	11500	23000	4	8	0.5	134.4	0.39	0.45	4.5
12	700	2800	1	4	0.25	66.32	0.27	0.28	5.5
13	2100	2800	3	4	0.75	66.32	0.39	0.46	10
14	1400	5600	2	8	0.25	66.32	0.37	0.40	2.1
15	1400	1867	2	2.67	0.75	66.32	0.35	0.41	13.2
16	1400	2800	4	8	0.5	46.89	0.45	0.52	7
17	500	1000	1	2	0.5	56.05	0.28	0.45	3.7
18	5000	10000	1	2	0.5	177.25	0.27	0.29	1.9
19	5000	10000	2	4	0.5	125.33	0.35	0.41	6.2
20	5000	10000	4	8	0.5	88.62	0.42	0.49	8.4

Table 4.1: Characteristics of test cases: Re_{ave}, average Reynolds number; Re_{jet}, jet Reynolds number; T^*_{ave}, average non-dimensional period; T^*_{jet}, jet non-dimensional period; T_s/T, stroke to period ratio; α, Womersley number; $(U_v/U_{jet})_{FI}$, vortex velocity to jet velocity ratio for the approach with ring's formation included (FI); $(U_v/U_{jet})_{FE}$, vortex velocity to jet velocity ratio for the approach with ring's formation excluded (FE); and $(U_1 - U_v/U_v)_{FI}$, relative velocity difference between first and quasi-steady vortex rings for the approach with ring's formation included (FI).

In this study, 18 periodic cases have been simulated for a range of average Reynolds number ($Re_{ave} = U_{ave}D/\nu$, where ν is the kinematic viscosity), average non-dimensional period ($T^*_{ave} = TU_{ave}/D$), and T_s/T, which are tabulated in table 4.1, accompanied with their related jet Reynolds number ($Re_{jet} = U_{jet}D/\nu$), jet non-dimensional period ($T^*_{jet} = TU_{jet}/D$), and Womersley number ($\alpha = D\sqrt{2\pi/T\nu}$). For biological flows, Reynolds number is typically between 50 to 4000 [99, 107]. The Reynolds number in engineering applications is relatively higher, e.g., around 10,000 for underwater robots that employ vortex ring thrusters [122]. Therefore, a range of Re_{ave} from 250 to 11,500 has been investigated here (table 4.1). Note that average non-dimensional period T^*_{ave} is equivalent to formation time ($T_sU_{jet}/D = L/D$, where L is the stroke length) because $U_{ave}T = U_{jet}T_s$ according to Eq. 4.1. For a broad range of flow conditions, formation number is around 4 [109]. Consequently, a range of T^*_{ave} from 1 to 4 has been investigated here (table 4.1). Three stroke ratios T_s/T of 0.25, 0.5, and 0.75 are also investigated (table 4.1).

4.3 Vortex Ring Dynamics

The dynamics of vortex rings in a periodic setup is an interesting phenomenon. In order to study the interaction of vortex rings, the iso-surfaces of vorticity magnitude $|\omega|$ colored with helicity density contour [123] are presented in figures 4.2-4.5. Here, we describe the interaction of vortex rings in the transient regime until reaching the periodic state for case 3, and then discuss the effects of the non-dimensional period and Re. Figure 4.2(*a*) shows that the velocity induction by the first leading vortex (L1) over the first stopping vortex (S1) toward its center reduces its diameter and causes it to go through L1. Note that the second leading vortex (L2) has a higher translational velocity relative to other vortex rings. While S1 goes through L1, L2 gets closer to them and induces velocity, which increases their diameter. Again, the velocity induction by L1 causes the engulfment of the L2 (figure 4.2(*b*)) and consequently, L2 induces some backward velocity over S1, pushing it to the back of L1. The close interaction of S1 with the stronger vortex L1 creates wavy structures on the weaker vortex S1 which leads to Tsi-Widnall instability (figure 4.2(*c*)) [124].

The shapes of Tsi-Widnall instabilities are Re dependent [125]. Figure 4.3 shows the shape of

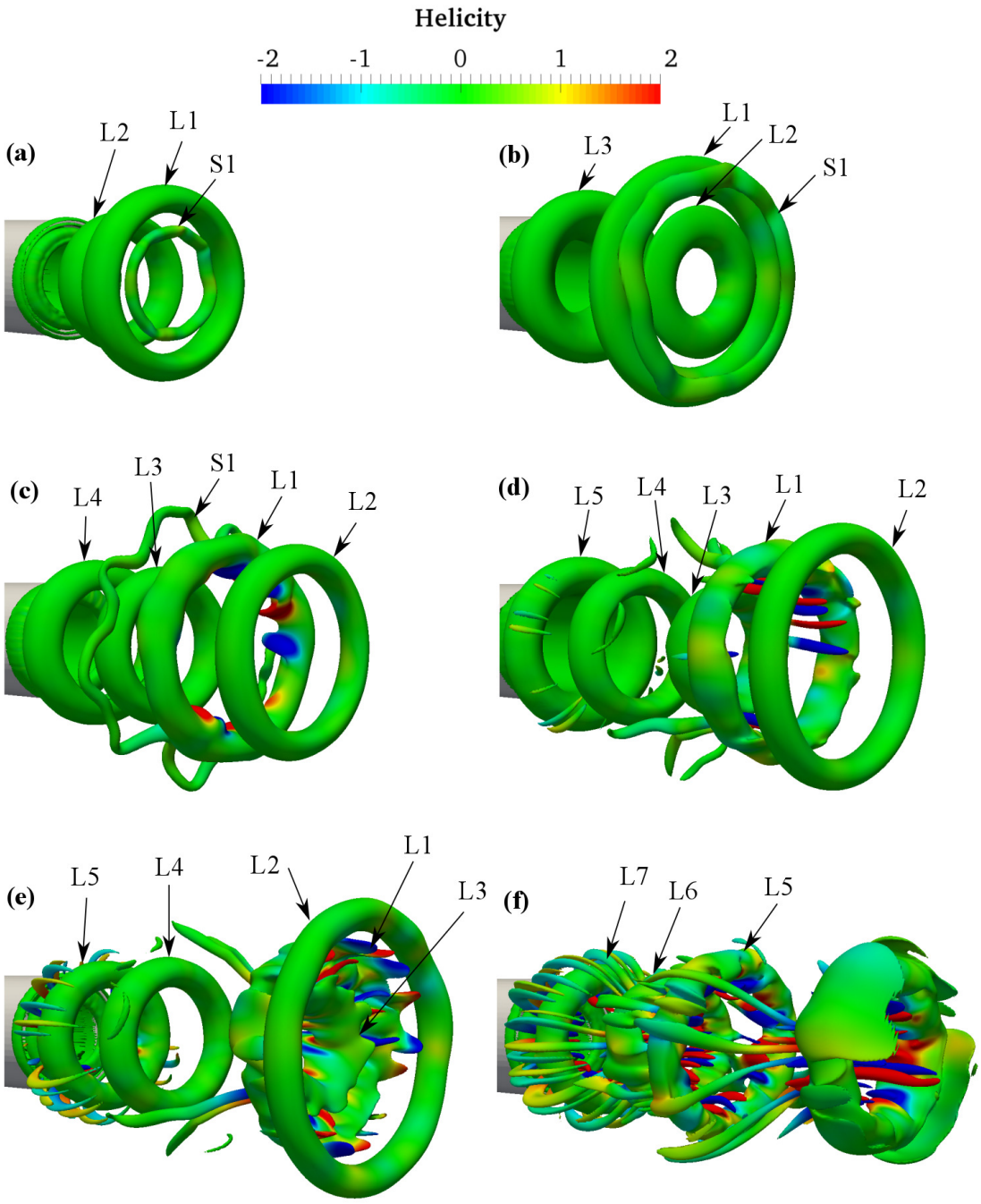

Figure 4.2: Vortex rings for case 3 ($Re_{ave} = 1400,\ T^*_{ave} = 1$) at times (*a*) $t/T = 2$, (*b*) $t/T = 2.65$, (*c*) $t/T = 3.75$, (*d*) $t/T = 4.5$, (*e*) $t/T = 5$, and (*f*) $t/T = 8$ visualized by plotting $|\omega| = 4$ isosurface of vorticity magnitude and colored by helicity density contours.

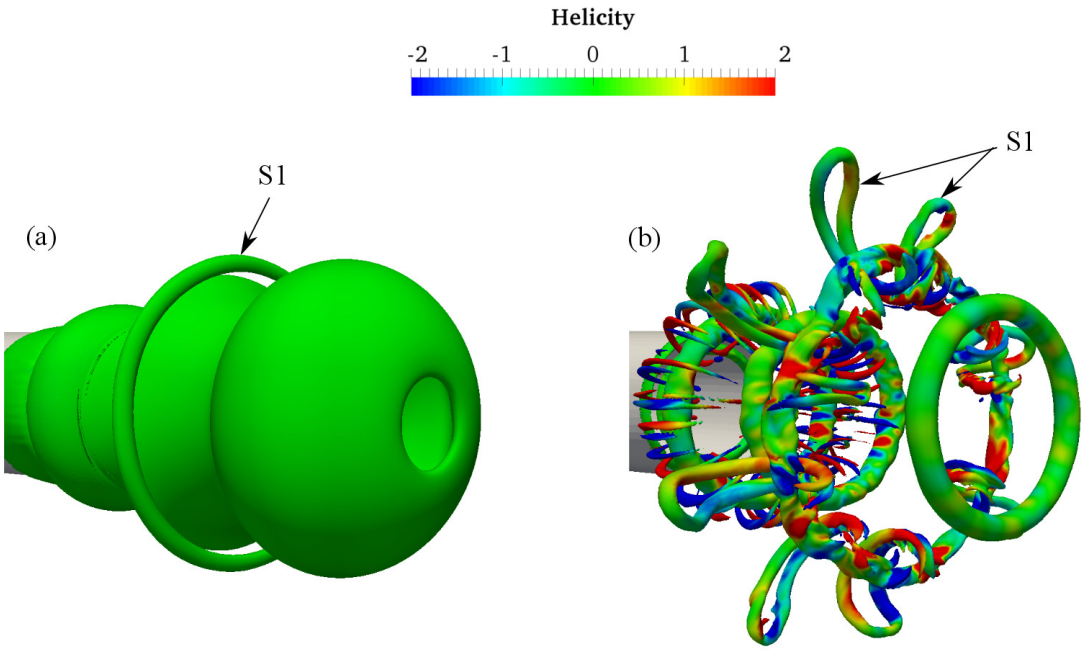

Figure 4.3: Effect of Re on the shape of the first stopping vortex ring (S1) at time $t/T = 3.75$: (*a*) case 17 with $Re_{ave} = 500$ and (*b*) case 5 with $Re_{ave} = 11500$, visualized by plotting $|\omega| = 1$ and $|\omega| = 9$ isosurface of vorticity magnitude for (*a*) and (*b*), respectively and colored by helicity density contours. $T^*_{ave} = 1$ for both cases.

S1 for a lower $Re_{ave} = 500$ and a higher $Re_{ave} = 11500$ at time $t/T = 3.75$. For the one with lower Re_{ave}, S1 is completely circular (figure 4.3(*a*)) but by increasing Re_{ave}, instabilities appear and intensify (figure 4.3(*b*)). For $Re_{ave} = 1400$, L1 and S1 are not connected (figure 4.2(*c*)); however, by increasing Re_{ave}, S1 ties around L1 (figure 4.3(*b*)).

As shown in figure 4.2(*d*), the breakdown of S1 spreads the instabilities throughout the domain, distorting the two closest leading vortices (L1 and the third leading vortex (L3)). Figure 4.2(*e*) shows the hairpin vortices generated upstream around the fifth leading vortex (L5), which are indeed the stopping vortices disturbed by the instabilities. In order to study the interaction of stopping vortices, isosurfaces of vorticity with a lower magnitude are illustrated in figure 4.4 for the same test case, as stopping vortices are weaker than the leading vortices. Figure 4.4(*a*) shows the perfect tubular second stopping vortex (S2) that surrounds L3. As L3 moves forward, S2 and

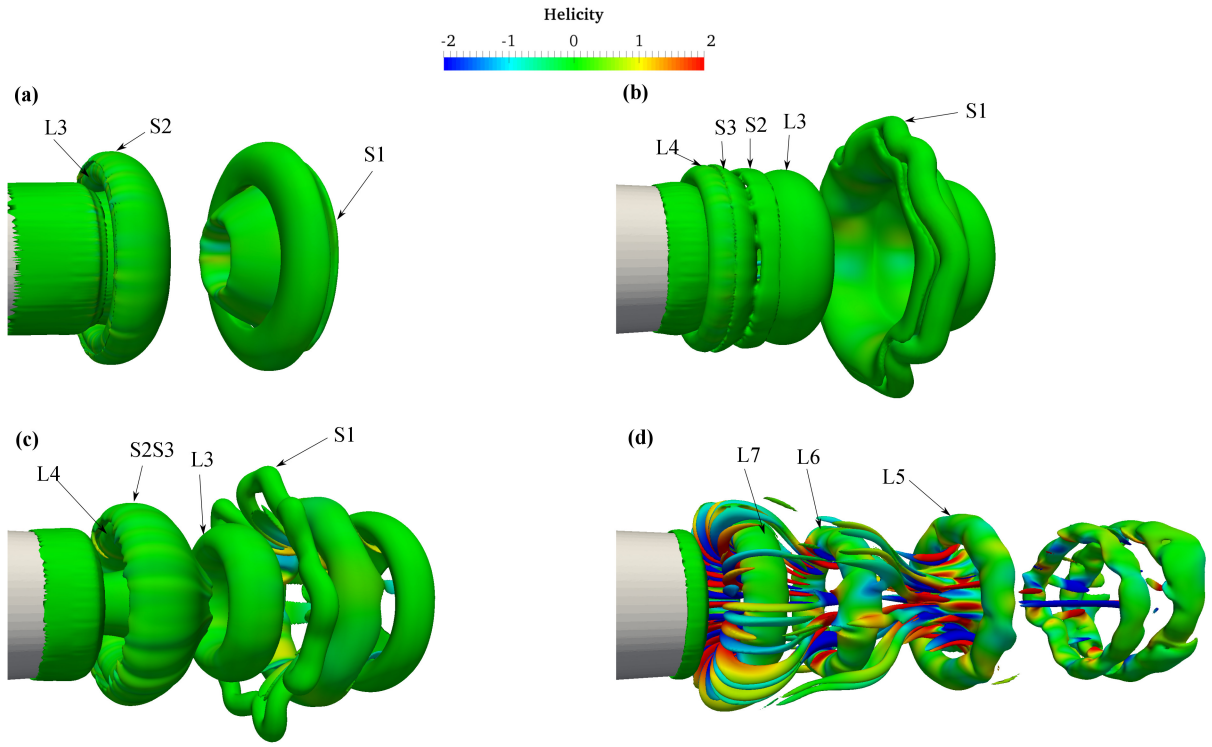

Figure 4.4: Stopping vortex rings for case 3 at times (*a*) $t/T = 2.5$, (*b*) $t/T = 3.25$, (*c*) $t/T = 3.85$, and (*d*) $t/T = 6.9$ visualized by plotting $|\omega| = 1$, $|\omega| = 2$, and $|\omega| = 4$ isosurface of vorticity magnitude for (*b,c*), (*a*), and (*d*), respectively and colored by helicity density contours.

the third stopping vortex (S3) get closer (figure 4.4(*b*)) and merge together—see the resultant vortex (S2S3) in figure 4.4(*c*). However, later, by the breakdown of S1 and the spread of instabilities, the stopping vortex rings lose their tubular shape and turn into hairpin vortices (figures 4.2(*f*) and 4.4(*d*)).

The breakdown of S1 and the consequent effects over other stopping vortices was not observed for lower $Re_{ave} = 500$. In addition, for higher $Re_{ave} = 11500$, S2 and S3 turn into hairpin vortices before the breakdown of S1, as observed in figure 4.3(*b*), which might be because of the existence of the immediate instabilities for vortex rings in high Reynolds numbers [57]. Increasing T^*_{ave} causes S1 to surround L2, rather than L1, and dissipate quickly without any breakdown—see figure 4.5(*a*) for test case 16. This simplifies the flow dynamics and makes reaching the quasi-steady state faster. Therefore, the stopping vortices for later periods remain tubular and the leading

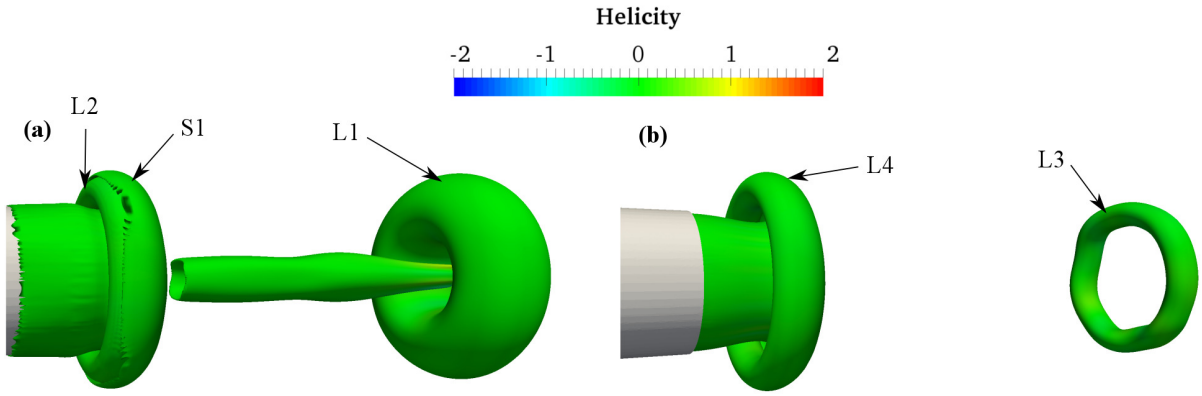

Figure 4.5: Vortex rings for case 16 ($Re_{ave} = 1400$, $T^*_{ave} = 4$) at times (a) $t/T = 2.25$ and (b) $t/T = 6.5$, visualized by plotting $|\omega| = 0.7$ and $|\omega| = 5$, isosurface of vorticity magnitude, respectively and colored by helicity density contours. The rings remain tubular at high T^*_{ave}.

vortices show the same behavior as previous periods. This is illustrated in figure 4.5(b) without the stopping vortices because of their very low vorticity magnitude. Note that the low vorticity long tubular structure that is located between $L1$ and $L2$ in figure 4.5(a) is the trailing jet [109] which is generated because of the relatively large formation time ($T_s U_{jet}/D = 4$) for the test case 16. These structures are also present in the quasi-steady state, but not observed in figure 4.5(b) because of their low vorticity magnitude.

In summary, there are two scenarios for stopping vortices after reaching the quasi-steady state. For cases with $T^*_{ave} \leq 2$ and $Re_{ave} \geq 1400$, the leading vortices are surrounded by hairpin vortices which are in fact the deformed precedent stopping vortices—similar to figure 4.4(d). By decreasing Re_{ave} or increasing T^*_{ave}, the stopping vortices surrounding the leading ones remain weak and intact (figure 4.5(b)).

All our test cases reached quasi-steady (cyclic) state and show two distinct interaction patterns (figure 4.6): (a) the cases that show vortex pairing at short $T^*_{ave} = 1$; and (b) the ones that do not pair and form a train of rings at high $T^*_{ave} \geq 2$. For cases with short $T^*_{ave} = 1$, the quasi-steady flow field consists of three different zones. Zone 1 is defined as the distance propagated by a quasi-steady ring in one period time interval starting from the edge of the cylinder. Here, the rings

form, detach, and propagate in the domain (see vortex ring L16 in figure 4.6(*a*)). Zone 2, which starts from the end of zone 1 and is extended approximately 4 to 5 times of zone 1, is where the quasi-steady vortex rings pair up and merge together (vortex rings L15, L14, and L12L13 in figure 4.6(*a*)). This phenomenon starts with accelerating one of the rings and shrinking its diameter due to velocity inductions. In figure 4.6(*a*), the first pair of rings (L15 and L14) at the beginning of zone 2 shows the onset of the pairing process. It is clear that the stretched core of one of the vortex rings (L15) ties around the circular one (L14). The second vortex ring at the end of zone 2 in the same figure (L12L13) is indeed two vortex rings after the pairing process. Zone 3, which is located after the end of zone 2, is where the vortex rings become unstable and break down. Since this zone is mostly located at the low-resolution part of the computational grid, the exact location of zone 3 may not be accurate. The approximate locations of these zones are shown in figure 4.6(*a*) for case 3 which shows the pairing process. Our results are consistent with the requirements for vortex pairing of [121]. The $T^*_{ave} = 1$ for this flow pattern is within the bounds of Strouhal number ($St_D = D/U_{ave}T = 0.85$; equivalent to $T^*_{ave} = 1/St_D = 1.18$) reported by [121] for "jet column mode" of vortex pairing. Additionally, their measured pairing location ($S/D = 1.75$) is placed in our zone 2 for this flow pattern.

For cases with longer $T^*_{ave} \geq 2$, the flow pattern includes only two zones. Zone 1, similar to the first zone of the previous pattern, is where the vortex rings develop, pinch-off, and propagate (see vortex rings L10, L9, and L8 in figure 4.6(*b*)). However, for this pattern, the length of zone 1 is relatively higher (equivalent to the distance a quasi-steady ring travels in 3 to 4 periods). For these cases, the vortex rings do not pair up after reaching a quasi-steady state, due to the relatively higher distance between the rings. However, vortex rings become unstable and break out just after the end of zone 1. We called this part of the domain zone 2 for this pattern. Figure 4.6(*b*) illustrates this flow pattern for case 4.

Figures 4.6(*c,d*) show flow patterns for cases 5 and 6, respectively. Comparing these figures with figures 4.6(*a,b*), shows that increasing Reynolds number does not affect the quasi-steady flow patterns. However, it destabilizes the pairing process [121] in zone 2 for the first flow pattern which

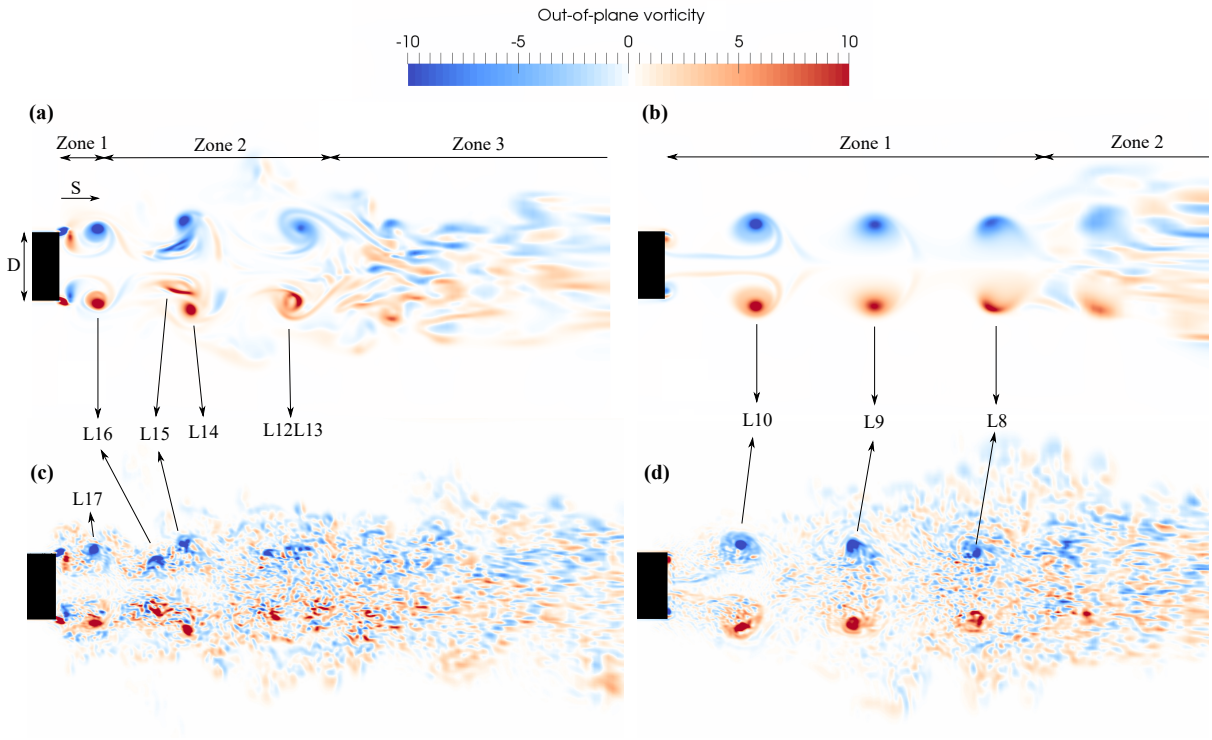

Figure 4.6: Out-of-plane vorticity contours of two distinct quasi-steady flow patterns for (*a*) case 3 ($Re_{ave} = 1400$, $T^*_{ave} = 1$), (*b*) case 4 ($Re_{ave} = 1400$, $T^*_{ave} = 2$), (*c*) case 5 ($Re_{ave} = 11500$, $T^*_{ave} = 1$), and (*d*) case 6 ($Re_{ave} = 11500$, $T^*_{ave} = 2$).

delays reaching quasi-steady state.

It is clear that vortex interaction in zone 2 of the first flow pattern could affect the cyclic state of zone 1. However, the interaction of vortices in zone 2 (the pairing process) follows a distinct pattern which is cyclic itself. There is still some small cycle-to-cycle variation in zone 1 because of the vortex interactions in zone 2. We quantified such variations by defining a 2% threshold for the difference in the trajectory of a vortex ring in zone 1 with respect to the previous ring in that zone. In this study, all of the test cases reached the cyclic state before the analysis of their propagation. Our results show that cases with the second flow pattern, i.e., without vortex pairing in zone 2, reach a cyclic state in 3 to 4 cycles, irrespective of their Re_{ave}. However, it takes more cycles for cases with the first flow pattern to reach a cyclic state due to vortex pairing in zone 2. Since high Re_{ave} destabilizes the vortex pairing process [121], increasing Re_{ave} for these cases makes reaching the cyclic state even longer.

4.4 Vortex Ring Propagation

In this section, the time history of the location of vortex rings is presented for all periodic test cases. Since the simulations are started from at rest condition, the propagation of the vortex rings should reach quasi-steady state. The number of periods required to reach quasi-steady state changed between 4 to 9 for different test cases. As mentioned before, the flow is considered to be quasi-steady if the change in time history of the location of a vortex ring with respect to its previous ring is less than 2% during the first period after the formation of those vortices. In this study, we tracked vortex rings for a time interval of T for all the periodic test cases to make sure that they remain in the fine region of our grid. Additionally, the aforementioned pairing phenomenon in zone 2 for cases with low T^*_{ave} (figure 4.6(*a,c*)) causes one of the rings to expand and accelerate and the other to shrink and decelerate when they get closer. Therefore, the propagation is only tracked in zone 1 before the pairing process. For the cases without pairing, tracking the vortex rings for a longer time does not affect our conclusions.

Reaching the quasi-steady state is shown for test case 6 in figure 4.7(*a*). For cases with high T^*_{ave} like this case, the interaction of the vortices is negligible for a few periods after the formation

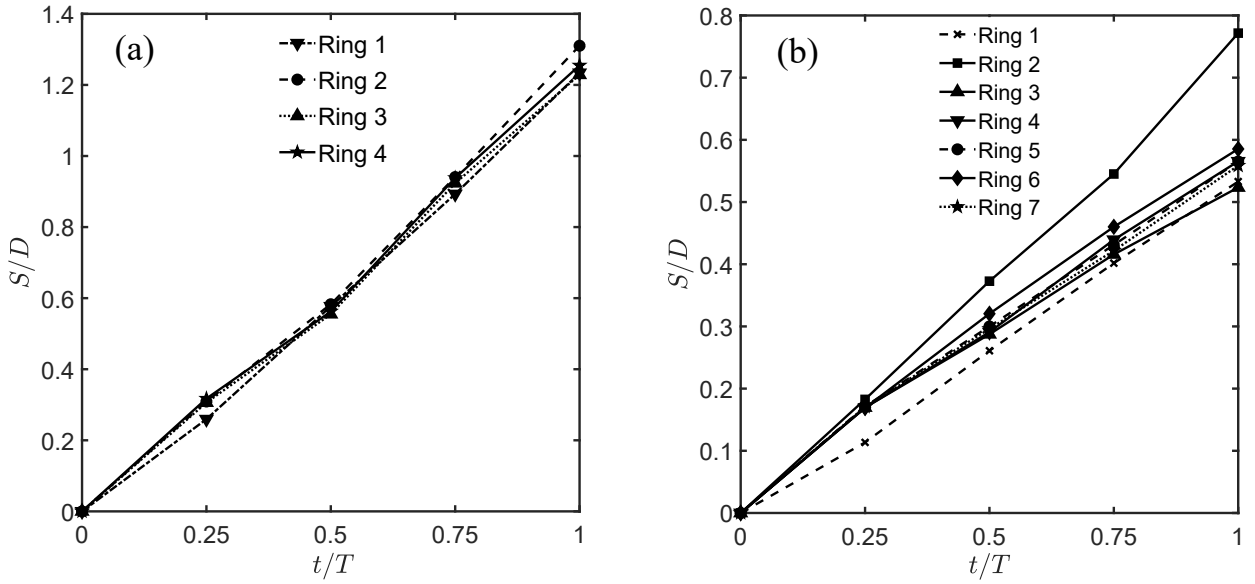

Figure 4.7: Location of vortex rings until reaching quasi-steady condition for test cases (*a*) 6 and (*b*) 5, traveled in one period.

of a vortex and, consequently, the propagation of vortex cores becomes quasi-steady after only 4 periods. Note that even small differences in the ring's velocity before reaching the quasi-steady state can lead to high interactions after several periods, e.g., ring 2 is engulfed by ring 1 in case 6 after four periods even though it is only slightly faster than ring 1 (figure 4.7(*a*)). However, for these test cases, as the flow reaches quasi-steady state, a train of vortices are formed (figure 4.6(*d*)). For cases with shorter T^*_{ave}, the interaction between the vortex rings plays an important role during the first periods after the formation of a vortex and takes longer to reach the quasi-steady state—see figure 4.7(*b*) for case 5.

Figure 4.8 shows the location of vortex rings for all periodic test cases during quasi-steady state accompanied with several experimental data. It should be noted that all the experimental data are non-periodic. Therefore, we used the stroke time T_s, instead of period T, to normalize time. The data of Gharib et al. [109] is for $Re = 6000$ and formation time ($T_s U_{jet}/D$) of 14.5, which is equivalent to T^*_{ave}. The two sets of data for Webster and Longmire [1] are the same as those discussed in §3.1.1 with formation time of 1. The data of Didden [110] is for $Re = 2300$

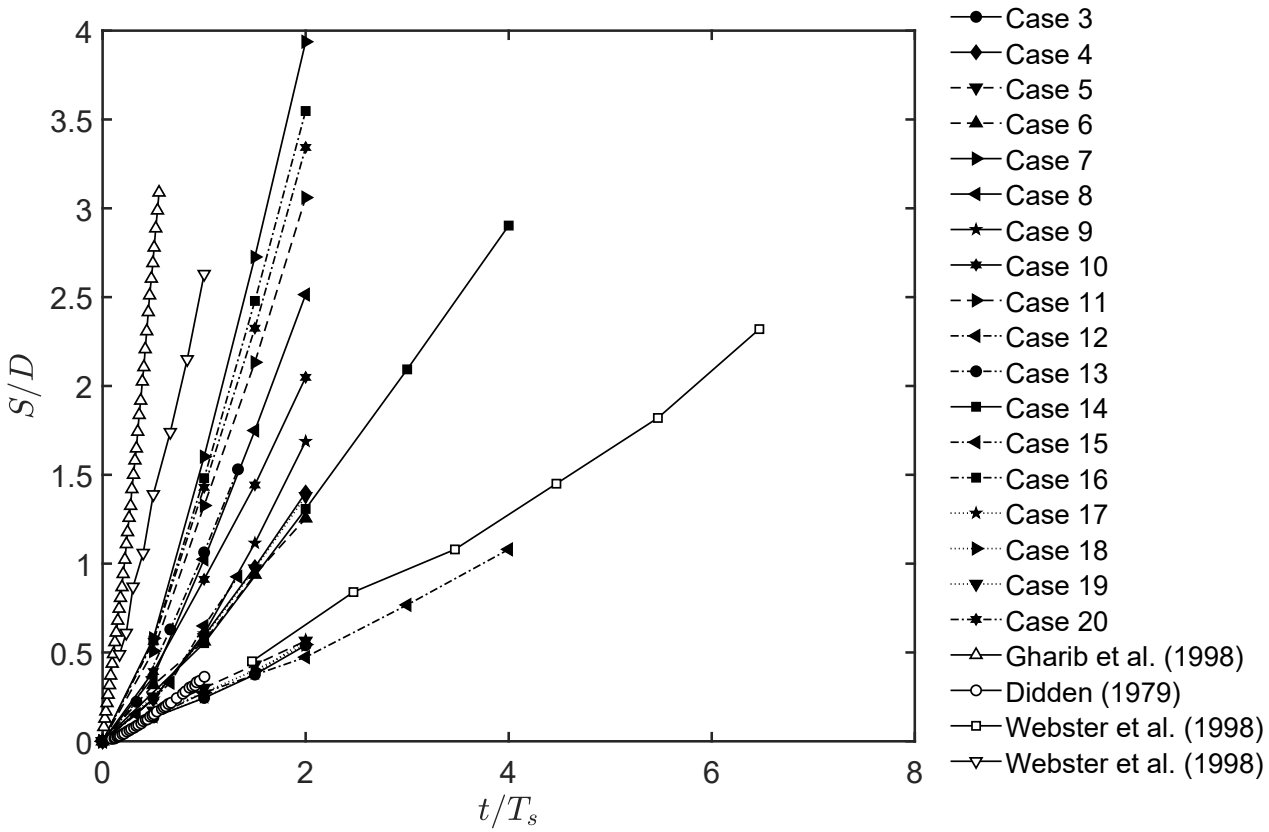

Figure 4.8: The location of vortex ring core centers of different numerical and experimental test cases.

and formation time of 1.4. As mentioned in §4.1, Didden [110] reported an exponential trend for time history of location of vortex core centers; however, figure 4.8 shows that after reaching the quasi-steady state, all of the test cases including data of Didden [110], can be approximated as linear with R-squared of greater than 0.97.

By dividing the slope of lines in figure 4.8 to their corresponding T^*_{ave} and taking into account the relation between U_{jet} and U_{ave} (Eq. 4.1), propagation velocity of vortex rings U_v/U_{jet} ($U_v = S/t$) are calculated. It can be observed that the slopes are not the same for different cases and show a widespread (figure 4.8). The effect of different parameters on the vortex ring velocity will be further discussed in the next section.

The slopes are calculated using two approaches: (a) calculating the slope from the core centers

tracked only after the ring is fully formed and detached from the cylinder, i.e., ring's formation excluded (FE) similar to [86]; and (b) calculating the slope from all core centers tracked starting from the jet inflow initiation, i.e., ring's formation included (FI). There are several methods in the literature for detecting the pinch off process, e.g., using the trailing pressure maximum [126, 127]. We used Burgers' model, as discussed in §3.1.1, for detecting the core boundaries and considered vortex rings pinched off when their boundaries completely disconnected from the cylinder. Including the formation process only slightly decreases the accuracy (R-squared value) of the linear fit, and still, it can be considered linear for the duration presented here as observed in figure 4.8.

Propagation velocity U_v/U_{jet} for both of the above approaches are tabulated in table 4.1. It can be observed that including the vortex formation process decreases the computed velocity because of two reasons: (1) the rings propagate slightly slower during the formation process and their speed increases as they are formed for short times after their initiation [110]; and (2) Tracking for a period and excluding vortex formation extends the tracking to the next inflow cycle. The next inflow cycle pushes the vortex under study forward, causes its velocity to slightly increase compared to the approach which includes the formation process. Note that based on our results, similar to the experimental results of [128], formation process is strongly Re dependent. Our results show that the formation process takes from approximately $T/4$ (for cases with $Re_{ave} > 500$) up to $3T/4$ (for cases with $Re_{ave} \leq 500$) after the inflow initiation for quasi-steady vortex rings. Different durations of the formation process make it difficult to use the FE approach to find an empirical relation for vortex propagation as a function of time because $t = 0$ at which the vortex is detached varies depending on the formation process. In contrast, $t = 0$ in the approach which includes the formation process is defined based on the inflow (figure 4.1(*b*)) and does not depend on Re_{ave}, T^*_{ave} or other parameters, i.e., suitable for finding an empirical relation for vortex propagation S/D and time t/T_s (figure 4.8).

For the approach which includes the formation process, the velocity of the first vortex (U_1) can be considered the velocity of an isolated vortex before the second vortex ring appears, i.e., for $t/T < 1$. The differences between U_1 and the quasi-steady ones (U_v) are reported in table 4.1

for the approach which includes the formation process. The other approach shows the same trend. Based on the results, the difference varies between less than 1% for case 3 to about 15% for case 9. For the lowest $T^*_{ave} = 1$, the difference varies between about 1% and 6%. However, for the highest $T^*_{ave} = 4$, it changes between about 5% and 11% depending on Re_{ave}.

4.5 Discussion

The vortex core velocity is a function of these dimensional parameters:

$$U_v = F\,(U_{ave}, U_{jet}, T, T_s, D, \nu). \tag{4.2}$$

where F is a function that relates U_v to the other variables. One possible arrangement of non-dimensional parameters is $U_v/U_{jet} = F\,(Re, T^*, T_s/T, U_{ave}/U_{jet})$. Considering the relation $U_{ave}/U_{jet} = T_s/T$ (see §4.2), two of the non-dimensional groups are equivalent. Consequently, we can eliminate U_{ave}/U_{jet}:

$$\frac{U_v}{U_{jet}} = F\,(Re, T^*, \frac{T_s}{T}). \tag{4.3}$$

Re and T^* in Eq. 4.3 could be defined using either the average or jet velocity. Our results (figure 4.9(*a*)) show that by choosing the average velocity in the definition of Reynolds number and non-dimensional period and keeping both fixed, different values of T_s/T does not affect the vortex ring velocity substantially for both approaches of computing velocity; however, using the jet velocity results in different vortex ring velocities (figure 4.9(*a*)). Based on linear fits to the points of figure 4.9(*a*), using U_{jet} in the definition of Re and T^*, gives slopes of 0.35 and 0.25 for formation process excluded and included approaches, respectively. On the other hand, using average velocity gives slopes as small as 0.03 for both approaches. Note that Re can also be defined based on the initial circulation of the vortex ring and be approximated as $Re_\lambda = U^2_{jet}T_s/2\nu$ [59]. By using this definition of Re and T^*_{jet} or T^*_{ave}, the vortex ring velocity shows dependency on the stroke ratio. Based on our results, for a fixed $Re_\lambda = 1400$ and $T^*_{ave} = 1$, changing T_s/T from 0.75 to 0.5 increases U_v/U_{jet} by 21% and 26% for formation excluded and included approaches, respectively. On the other hand, by keeping $Re_\lambda = 5600$ and $T^*_{jet} = 8$ and changing T_s/T from 0.25 to 0.5,

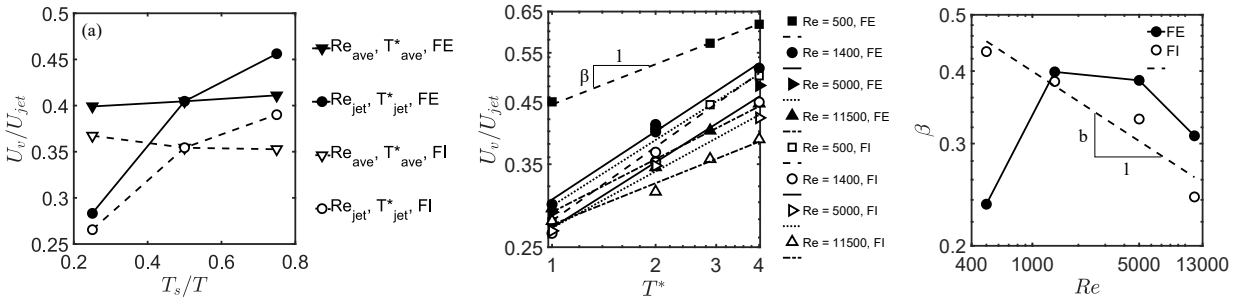

Figure 4.9: Vortex core velocity analysis with both ring's formation excluded (FE) and ring's formation included (FI): (*a*) the effect of T_s/T on vortex ring velocity for fixed Re and T^*, which are defined based on the average or jet inflow velocity, (*b*) the vortex velocity versus non-dimensional period for different Re in log-log scale, and (*c*) the slopes of lines in (*b*) for relevant Re in log-log scale.

U_v/U_{jet} increases by 30% and 23% for formation excluded and included approaches, respectively. Therefore, we choose to define Re and T^* based on U_{ave} to have U_v/U_{jet} be approximately independent of T_s/T, i.e., a simpler scaling law $U_v/U_{jet} \approx F(Re_{ave}, T^*_{ave})$. Note that this result is limited to waveforms illustrated in figure 4.1(*b*). Hereafter, Re=Re_{ave} and T^*=T^*_{ave} for simplicity.

We investigate how U_v/U_{jet} scales with Re and T^* by plotting U_v/U_{jet} versus T^* for different Reynolds numbers in log-log scale (see figure 4.9(*b*)). These lines closely, with R-squared greater than 0.97, represent lines with slope β in log-log scale, i.e., a power law with exponent β and coefficient c ($U_v/U_{jet} = cT^{*\beta}$). Figure 4.9(*b*) shows that for a fixed non-dimensional period, the ratio of U_v/U_{jet} reduces by increasing the Reynolds number, e.g., it goes from 0.5 to 0.39 by increasing Re from 500 to 11,500 at $T^* = 4$ for the approach which includes the formation process. It can also be observed that for a fixed Re, increasing the T^* would increase U_v/U_{jet}, which is consistent with the results of [119] (see its figure 4b), e.g., U_v/U_{jet} changes from 0.28 to 0.5 by increasing T^* from 1 to 4 at $Re = 500$ when the formation process is included. Based on the above results, U_v/U_{jet} is more sensitive to T^* than Re. Note that T^* here is equivalent to formation time [109] as discussed in §4.2.

We plot the exponent of the power law (β) as a function of their Re in log-log scale (see figure 4.9(*c*)). It is clear that the functional form of β depends on the velocity calculation approach.

The results for the approach which includes the formation process with relatively high accuracy, R-squared about 0.92, can be approximated by a line of slope b, i.e., a power law with exponent b ($\beta = aRe^b$). Consequently:

$$\frac{U_v}{U_{jet}} = c\, T^{*\, aRe^b}, \tag{4.4}$$

where, $a = 1.31$, $b = -0.2$, and $c = 0.27$ based on all of the lines in figure 4.9(*b,c*) when the formation process is included. It is interesting that the limit of Eq. 4.4 for very high Re, provides the vortex ring velocity as 0.27 of U_{jet}, which is consistent with empirical results of [86]. As shown in figure 4.9 (c), the approach which excludes the formation process has the same trend as the other approach until $Re = 1400$, i.e., β increases as Re decreases, but for the low $Re = 500$ the trend does not continue probably because of the large duration of formation process ($3T/4$) compared to higher Re cases ($T/4$). This approach is problematic because the reference time ($t = 0$) to initiate the tracking and finding a relationship varies from case to case as the time required for the formation of the rings varies with Re—see the discussion at the end of the previous section. This makes the approach which includes the formation process a better candidate for an empirical relation for the location S/D as a function of time (figure 4.8) as the time in this approach is clearly defined based on the flow pulse at the inflow ($t = 0$ coincides with the start of the inflow in each period). Nevertheless, because β does not vary much with Re, we can approximate β as a constant, i.e., $\beta \approx 0.3$ for the approach that excludes the formation process. This will provide us with an approximation that is independent of Re, which we will investigate as well.

Considering that the translational velocity of the vortex ring is the displacement of its core center in the streamwise direction over the required time, we can take $S = U_v t$. By dividing both sides of this equation to D and multiplying the right-hand side to $U_{ave}T/U_{jet}T_s$, which is equal to unity, we get:

$$\frac{S}{D} = \frac{U_v}{U_{jet}} \frac{U_{ave}T}{DT_s} t. \tag{4.5}$$

Now, by substituting non-dimensional period $T^* = U_{ave}T/D$, Eq. 4.5 becomes:

$$\frac{S}{D} = \frac{U_v}{U_{jet}} T^* \frac{t}{T_s}. \tag{4.6}$$

By substituting U_v/U_{jet} from Eq. 4.4, one can obtain:

$$\frac{S}{D} = (0.27\ T^{*\ 1+1.31Re^{-0.2}}) \frac{t}{T_s}. \tag{4.7}$$

This equation provides a scaling law for the location of vortex ring core centers at different Reynolds and non-dimensional periods (formation time). Substituting T^* based on its relation with Reynolds and Womersley numbers ($T^* = 2\pi Re/\alpha^2$), Eq. 4.7 is written in terms of Wormersley and Reynolds number:

$$\frac{S}{D} = [0.27(\frac{2\pi Re}{\alpha^2})^{1+1.31Re^{-0.2}}] \frac{t}{T_s}. \tag{4.8}$$

We see that if the Womersley number is kept constant, contrary to when T^* is kept constant (Eq. 4.7), increasing Re will increase vortex propagation. Also, by fixing Re and increasing Womersley number, vortex propagation decreases as predicted by [60].

To see if the proposed relation (Eq. 4.7) can scale the data of figure 4.8, S/D scaled with Eq. 4.7 is plotted against t/T_s in figure 4.10. In this figure, Eq. 4.7 is a line with slope one (zero-error line). The proposed relation not only collapses the numerical data of figure 4.8 around the zero-error line, but also the scattered experimental data (shown more closely in the inset of figure 4.10), which were not part of the curve fitting process (Eq. 4.4). This is probably due to the fact that the quasi-steady velocity of the vortex ring is close (maximum 15% difference) to the velocity of the initial (isolated) one as discussed in the previous section. Note that we did not check this scaling for closely spaced rings where they interact even after reaching quasi-steady condition. In fact, this might be another reason that the proposed scaling for periodically generated rings works for isolated ones as well. In the scaling of the experimental data, which are non-periodic, formation time ($T_s U_{jet}/D$) is used which is equivalent to T^* here. Therefore, the above scaling can be used

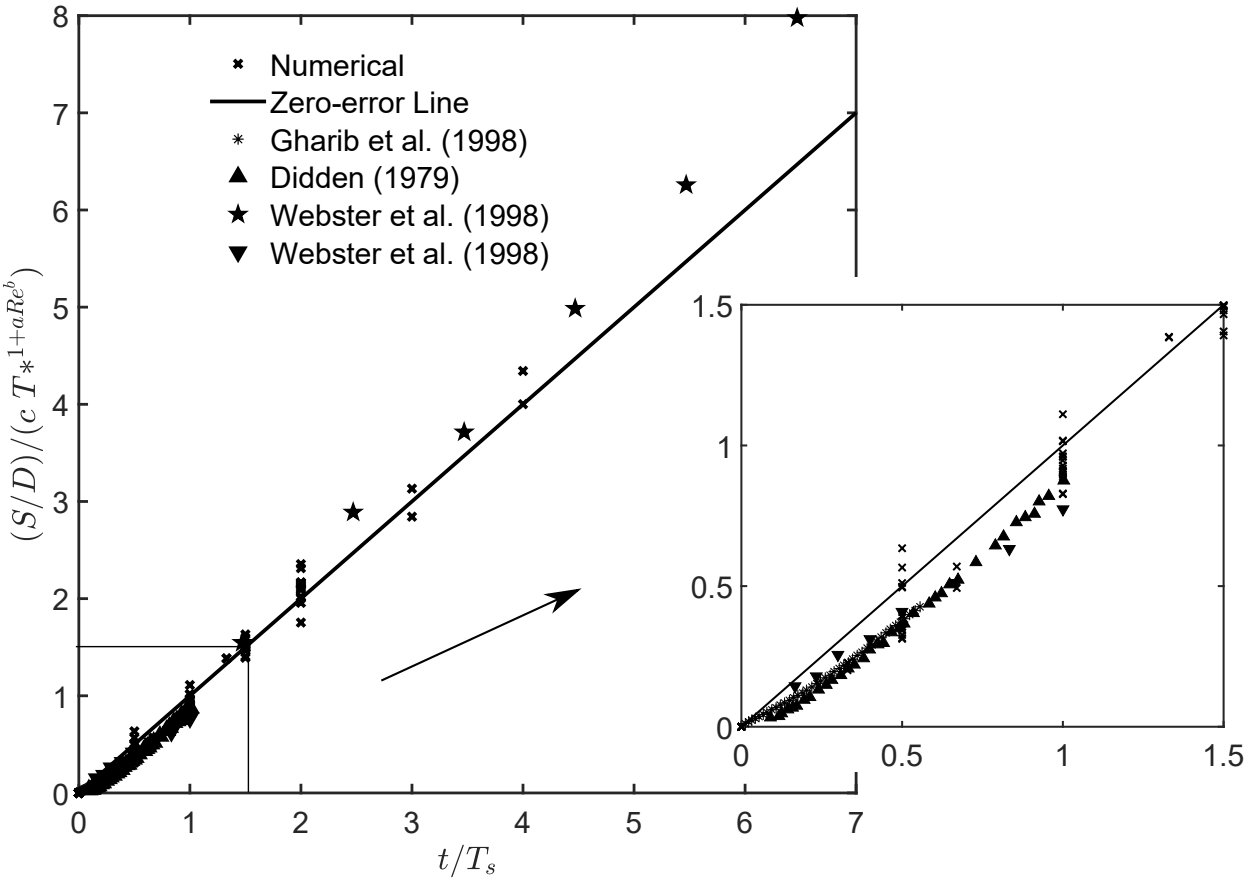

Figure 4.10: Location of vortex ring core centers after scaling for numerical and experimental test cases.

for non-periodic rings as well by using formation time in place of T^*.

It is interesting to observe that the experimental data for non-periodic rings (except $\star$ Webster et al, 1998) fall below the zero-error line as observed in figure 4.10. It seems that during the early formation of the vortex ($t/T_s < 0.25$) the isolated rings propagate slower relative to the zero-error line, but after they are fully formed their trajectory follows almost the same slope as the zero-error line. The slower speed of isolated rings during the formation process has been previously observed [110]. The data for our periodic rings falls both above and below the line. We have observed that the periodic rings are also slightly slower during their formation process, but it is overshadowed by the effect of Re and T^* on the propagation of periodic rings. As we discussed in figure 4.9(*b*), the propagation speed is more sensitive to T^* than Re. Removing Re from the equation by considering the limit of $Re \rightarrow \infty$, Eq. 4.7 simplifies to $S/D = (0.27T^*)t/T_s$ which shows a noticeable degradation in collapse of data (R-squared = 0.88). Considering a constant $\beta \approx 0.3$ (not $\beta = aRe^b$) for Eq 4.4 and substituting into Eq. 4.6 provides another formulation for $S/D = (0.27T^{*1.3})t/T_s$ that is independent of Re. This formulation collapses the data (R-squared=0.97) almost as good as Eq. 4.7 (R-squared = 0.98). The underlying reason is the small variation of β ($0.24 < \beta < 0.43$) for the range of Re of our test cases—see figure 4.9(*c*). Although including the Re does not seem to be necessary for the range of Re tested here, such an approximation might not work well for very high Re ($Re \gg 10,000$ cases, which were not investigated here due to their high computational cost). In addition, it is clear from figure 4.9(*b*) that the increase of Re at a constant T^* decreases the propagation speed, i.e., excluding Re from the equation reduces the accuracy.

4.6 Conclusion

Based on different test cases for a range of Reynolds number, non-dimensional period, and stroke ratio (T_s/T), an empirical relation (Eq. 4.7) for the location of periodically generated vortex rings is proposed. This equation not only scales the numerical results but also collapses the results of experiments for non-periodic rings (figures 4.8 and 4.10). Based on our results, the number of cycles needed for reaching the periodic state is controlled by T^*_{ave}. For cases with short $T^*_{ave} = 1$, it takes more cycles to reach quasi-steady (cyclic) state because of the pairing process downstream of

the newly generated ring. The stability of this process for these test cases is affected by Re_{ave}. Our observations in the cyclic state show that for low $T^*_{ave} \leq 2$ and high $Re_{ave} \geq 1400$, the stopping vortices deform into hairpin vortices and envelop the leading ones. However, by increasing T^*_{ave} or decreasing Re_{ave}, the original form of the stopping vortices are maintained. The results show that the periodic vortex ring velocity is close to the velocity of an isolated one (maximum 15% difference). Based on our results, the vortex velocity U_v/U_{jet} becomes independent of the stroke ratio when the average velocity is used in the definition of Reynolds number and non-dimensional period. In this way, vortex ring velocity becomes only a function of the Reynolds number and non-dimensional period. The vortex ring velocity is more sensitive to the non-dimensional period (formation time) than the Reynolds number, and depends on them according to a power law (Eq. 4.4). The results show that for a fixed non-dimensional period, vortex ring velocity decreases by increasing the Reynolds number. However, if the Womersely number is kept constant (instead of the non-dimensional period) then the vortex ring velocity increases by increasing the Reynolds number (Eq. 4.8). On the other hand, keeping the Reynolds number fixed and reducing the non-dimensional period (increasing the Womersely number) decreases the vortex ring velocity.

5. VORTEX DYNAMICS OF BI-LEAFLET MECHANICAL HEART VALVES (BMHV)

In this chapter, the vortex dynamics of a bi-leaflet mechanical heart valve (BMHV) in an aorta-left ventricle configuration is investigated. This chapter is organized as follows. First, the literature review of the hemodynamics of BMHVs is provided in §5.1 for different implantation orientations. Then, the computational set-up utilized for this study is presented in detail in §5.2. The reader is referred to §2.1 for details of the numerical framework utilized for the flow solver of this chapter. Next, in §5.3, the kinematics of the leaflets of the valves are discussed for different orientations during multiple cycles. The vortex dynamics, shear stress distribution, and platelet activation for different orientations are addressed in §5.4, §5.5, and §5.6, respectively. Finally, the outcome of the results is discussed in §5.7.

5.1 Background

It is approximated that 156,000 surgical operations are performed each year in the US to replace defective human heart valves [129], 20% of which are substituted by BMHV [130]. Despite the decline in the usage of BHMV in recent years, these valves are considered a better option for patients between 50 to 70 years old due to their high durability [131]. On the other hand, the BMHVs are associated with generating non-physiological flow patterns, imposing high shear stress on blood cells, which can cause thrombus generation [132]; thus, requiring patients to consume anticoagulant drugs for the rest of their lives. The hemodynamics of implanted BMHVs have been investigated in recent years in numerous experimental and numerical studies [133, 134, 135, 136, 137, 138].

The implantation orientation of BHMV is particularly important due to its bilateral symmetry as opposed to the triradial symmetry of the aortic sinus area, which creates different flow patterns compared to native heart valves [139, 140, 141, 142, 143]. The effects of implantation orientation of St. Jude Medical BMHV (figure 1.1(c)) and Medtronic Hall tilting disk MHV (TMHV) (figure 1.1(b)) were investigated in an in vivo study on healthy pigs [144]. Their results showed that

when the major orifice of TMHV is faced toward the right-posterior aortic wall, it produces less turbulence [144]. For the BMHV, the same orientation showed lower turbulence compared to the orientation perpendicular to it; however, the difference was not considerable. Later, the left coronary flow for different valve orientations was studied [145]. It was found that when the BMHV line of symmetry intersects the non-coronary cusp, i.e., the valve lateral orifices are aligned with the right coronary cusp, it produces higher left coronary flow. In a separate in vitro study [146], this orientation was associated with stronger forward flow and sinus recirculation, correlating with higher coronary flow [147]. In a recent experimental study, St. Jude Medical BMHV and Lapeyre-Triflo FURTIVA tri-leaflet mechanical heart valve were compared in terms of wall-shear stress (WSS) [137] and found that the bi-leaflet valve imposes peak WSS near twice the magnitudes of the tri-leaflet one. They reported that it was due to the magnitude of the jet-like flow and the location of its impingement on the aortic wall [137].

A previous work studied the effects of BMHV implantation orientation in an anatomic aorta [63] and found that despite the negligible effects of implantation orientation on shear stress distribution in the aorta, valves with the plane of symmetry aligned with the plane of curvature of the ascending aorta show better results in terms of the symmetrical motion of the leaflets and minimum rebound during the closing phase compared to other orientations. Afterwards, an in vitro study[148] compared the turbulent and viscous stresses above the threshold of blood cells damage criteria and found higher values for the valve with the plane of symmetry perpendicular to the aortic plane of curvature, which was concluded to be the result of the impact of the lateral jet to the aortic concave wall and higher velocity gradient due to the asymmetry of the valve central jet relative to the sinuses [148]. However, this study was limited to peak flow and center-plane of the aorta and did not consider different cross-sections and time instants. In a recent numerical study [62], BMHVs with different tilting angles were compared in terms of the kinematics of the valves in an anatomic aorta and found that intermittent regurgitation is minimized for the valve with the pivot axis parallel to the plane of curvature of the aortic root, which resulted in lower platelet activation levels.

In the previous work [63], the effects of implantation orientation were studied using an axisymmetric inflow generated based on a prescribed physiological waveform, which might not be a precise representation of the asymmetrical flow driven by a contracting left ventricle (LV). This approximation might alter the effects of valve orientation during systole compared to diastole. To investigate the consequences of asymmetric inflow by an LV, therefore, we have added a moving anatomic LV to the anatomic aorta to study the effects of implantation orientation on valve kinematics and hemodynamics during both systole and diastole for multiple cycles.

5.2 Computational Details

The overset computational domain used for this study, as shown in figure 5.1, consists of two sub-domains: the LV and the aorta blocks. The LV block contains the anatomic LV chamber with contracting walls to which the mitral orifice is connected. The anatomic aorta block is connected to the LV block via an interpolation interface and contains the BMHV (structural domain). The anatomic LV and aorta geometries are reconstructed from magnetic resonance imaging (MRI) scanned images of a healthy subject provided by the Cardiovascular Fluid Mechanics Laboratory at the Georgia Institute of Technology with a method similar to [149] and meshed with triangular elements as required by the CURVIB solver. The geometries are nondimensionalized with diameter $D = 25.4\ mm$ of the aortic orifice.

In this study, turbulence modeling is not included and the blood is assumed to be Newtonian. Since the blood flow is pulsatile, it only transitions to turbulence. It is not a fully turbulent flow to use turbulence modelings such as Reynolds-averaged Navier-Stokes (RANS) and large eddy simulation (LES) whose constants are obtained based on high Re fully turbulent channel flows. Indeed, these turbulence models are highly diffusive and are not suitable for pulsatile low Re transitional flows in human arteries. Therefore, similar to previous computational studies [63, 46, 150], all the features of the pulsatile flow are resolved by directly solving the Navier-Stokes equations, and turbulence modeling is not included. The Newtonian fluid assumption is valid for flows in larger arteries; however, in the small gaps between the BMHV and the housing, i.e., the hinge area, the non-Newtonian effects could be dominant. Modeling the hinge area requires very

fine mesh near the valve, which is beyond the scope of this work, and therefore blood is assumed to be Newtonian.

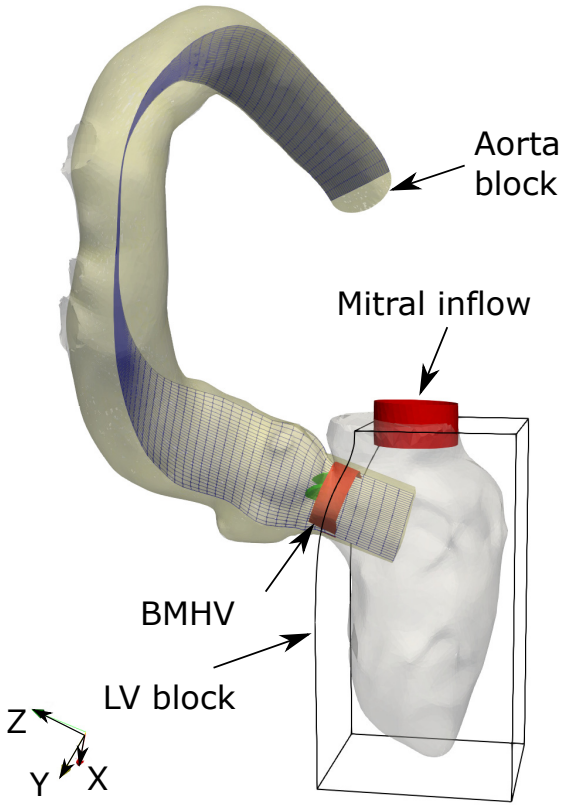

Figure 5.1: The overset grid consists of two grid blocks: a box-shaped block that contains the anatomic LV and a body-fitted block for the anatomic aorta, where the BMHV is placed. A cross-section of the aorta body-fitted grid is plotted for only every five grid points for better illustration.

The LV geometry and the mitral inflow are placed as immersed boundaries inside the LV block (grid box) of dimension $4.5D \times 4.4D \times 2.9D$ with $201 \times 125 \times 145$ (3.6 million) grid points, which is similar to the grid of related studies [151, 152, 153] that found it to be fine enough to produce grid-independent results. The LV motion is prescribed based on a lumped parameter model [154], which is used to provide the volume of the LV with a physiological stroke volume of $66mL$ and ejection fraction of 55% [155]. The LV geometry is scaled by the cubic root of the volume in both

axial and radial directions of the LV. However, the top of the LV, where the mitral and aortic orifices are located, is fixed and the motion of 30% below the aortic outflow toward the LV apex is linearly constrained to smoothly transition to the rest of the LV motion (see [81] for more details). The prescribed motion of the LV generates a physiological flow waveform with one large systolic and two smaller diastolic peaks (E-wave and A-wave, respectively) during one cardiac cycle ($860\ ms$) with the peak flow rate of $23.6\ lit/min$ as illustrated by solid line in figure 5.2. The LV waveform creates a systolic duration of $400ms$, which is within the physiological range [156], measured from the end of the second diastolic wave (A-wave) till the end of the systolic wave.

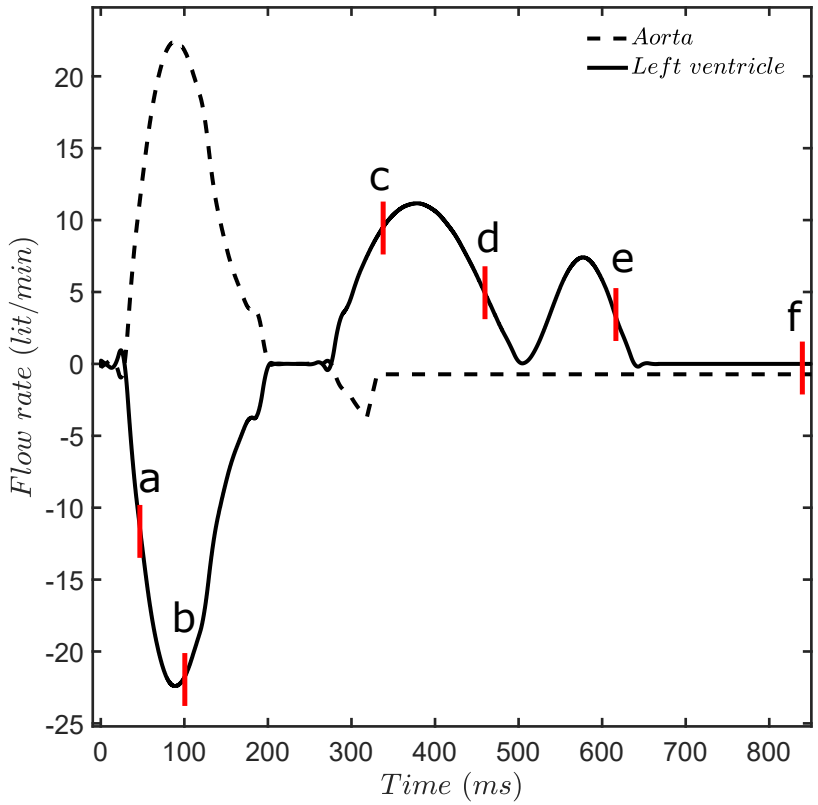

Figure 5.2: The LV and aorta flow rates during one cardiac cycle ($860\ ms$). The flow is visualized in time instants marked with thick vertical red lines a, b, c, d, e, and f.

In order to simplify the outflow boundary condition, the main branches of the anatomic aortic

arch, i.e., the coronary arteries, the carotids, the innominate artery, and the left subclavian artery, have been removed [61]. While the leaflet kinematics during opening are not that sensitive to the downstream geometry, they might be affected by the downstream geometry during the closing. However, the flow rate through the coronary and branches are not high compared to the main branch during the closing phase. Therefore, they are ignored in this study. A body-fitted curvilinear grid with $161 \times 161 \times 401$ (10.4 million) grid points has been utilized to discretize the anatomic aorta. Previous validation studies [46, 61] have shown that such fine grids are adequate to capture the valve kinematics and hemodynamics of the aortic arch with good accuracy. A cross-section of the body-fitted grid for the aortic block is shown in figure 5.1 for only every five grid points for clarity. In this study, the deformation of the aorta is assumed to be negligible; therefore, the aortic block is considered rigid.

The valve and the housing geometries (clinical quality St. Jude Regent 23 mm valve) are discretized with triangular grids (figure 5.3(a)) and placed at the beginning of the sinus area (figure 5.1) in three different orientations, each positioned 45 deg from the other, as illustrated in figure 5.3(b). The different orientations are identical to the previous work [63], in which the 0 deg orientation corresponds to a case which valve plane of symmetry is parallel to the ascending aorta's plane of curvature, as shown in figure 5.3(b) with green leaflets. The location of left coronary (LC), right coronary (RC), and non-coronary (NC) cusps are shown in figure 5.3(b) for clarity. The 90 deg orientation is perpendicular to the aorta plane of curvature (red leaflets in figure 5.3(b)) and the 45 deg is oriented between the 0 and 90 deg orientations as shown with blue leaflets in figure 5.3(b). The angle of attack of each leaflet with respect to the streamwise direction varies from 5 deg, as fully open, to 59 deg, as fully closed [61].

Each leaflet is considered to rotate around the hinge axis of the valve; therefore, the angular momentum equation governs the motion of the structure domain, which consists of a system of second-order ordinary differential equations (ODE). These equations are transformed into a set of first-order ODE and then integrated in time using the trapezoidal rule [46, 61].

The reduced-inertia of the valves are considered $I_{red} = 0.001$ similar to [63, 46, 61], as-

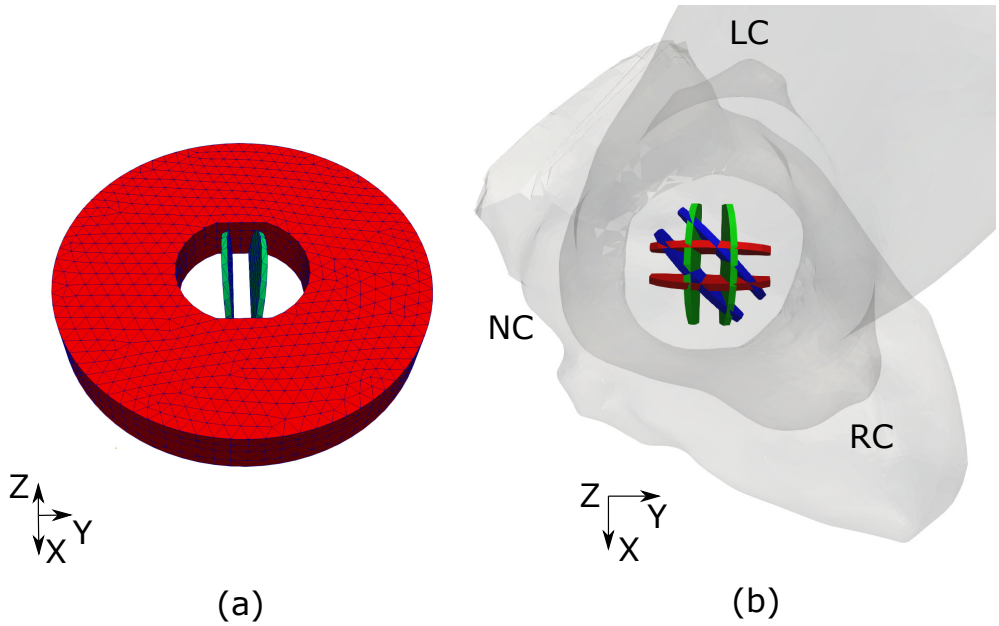

Figure 5.3: (a) A typical BMHV with triangular mesh, as required by the CURVIB method. (b) The location of valves inside sinus from a top view. The green, blue, and red leaflets correspond to 0, 45, and 90 deg orientations, respectively. RC - right coronary cusp; LC - left coronary cusp; NC - non-coronary cusp.

suming Polycarbonate as the leaflet material with a density of $1750\ kg/m^3$ and blood density of $1030\ kg/m^3$. As in the previous work [63, 46, 61], the hinge geometry, which connects the leaflets to the valve housing, has been removed. Additionally, the damping due to the hinge friction has been neglected, since it is small relative to the flow forces and there is no precise experimental data available. As the LV contracts according to its prescribed waveform (solid line in figure 5.2), the aortic valve opens while the mitral valve remains closed. During this phase, the convective boundary condition is applied at the aortic block outflow similar to [63, 46, 61]. By the beginning of the diastolic phase, the outflow of the aortic block reverses to an inlet with pulsatile plug flow according to the dashed waveform in figure 5.2 and the mitral valve opens as the second inflow. In this work, the mitral valve is replaced with a circular orifice with the diameter of $22.4\ mm$. Despite the potential effects of the mitral valve on the LV vortex ring during the diastole [157], the mitral valve does not significantly affect the flow during systole (because it is closed) or the aorta when the aortic valve is closed. The equations are nondimensionlized using the aortic diameter $D = 25.4\ mm$

and the peak bulk velocity $U = 0.778\ m/s$ at 70 bpm, leading to the peak Reynolds number of $Re = 6000$ with blood viscosity of $\nu = 3.3 \times 10^{-6}\ m^2/s$. Each cardiac cycle is discretized with 5000 time instants, leading to the physical time step of $\Delta t = 0.17\ ms$ for all different orientation simulations similar to a previous work [80]. In order to investigate the effects of ventricular flow, all of the simulations are performed for at least two cycles. For 0 deg orientation, an extra (third) cycle is performed to illustrate the cycle-to-cycle variations in valve kinematics.

As discussed earlier, the motion of the LV was prescribed while the motion of leaflets are calculated using the under-relaxed SC-FSI algorithm enhanced with the Aitken acceleration technique [46]. Our results show that this method reduces the residual (i.e., the difference in angular velocity and position of each leaflet between two successive iterations) by about 4 orders of magnitude to 10^{-6} within 5 iterations.

5.3 Leaflet Kinematics

The calculated leaflet angles for different orientations are shown in figure 5.4 for multiple cycles. The insets in the plots for each orientation illustrate the opening phase of leaflet kinematics in detail. The flow waveform of the LV is also included in the plots to give a better view of the leaflet kinematics with respect to the related time instant during the cycle. For convenience, we shall refer to the first-to-fully open leaflet as leaflet 1 for each orientation, and subsequently, the other leaflet will be referred to as leaflet 2. As it is shown in the insets, for all the orientations, both of the leaflets for the first cycle have a $30\ ms$ delay to start to open compared to the later cycles. This causes the rebound during the beginning of the opening for the first cycles for all orientations. However, the leaflets for the first cycle show higher acceleration so they reach fully open position almost at the same time compared to the later cycles. Therefore, for all orientations, there are no cycle-to-cycle variations in reaching the fully open position for both leaflets. The insets of figure 5.4 show that leaflet 1 fully opens simultaneously for all different orientations; however, leaflet 2 for 0 deg orientation reaches fully open slightly sooner than other orientations. There are 6, 11, and 13 ms time differences between reaching fully open position for leaflets 1 and 2 for 0, 45, and 90 deg orientations, respectively. Therefore, 0 deg orientation shows less asymmetry in

the opening phase than the other ones. The results show that the rebound duration for leaflets 1 after reaching the opening position till fully open again are 10, 15, and $13ms$ for 0, 45, and 90 deg orientations, respectively. Additionally, as it is shown in the inset of figure 5.4(a), the opening phase of the valve with 0 deg orientation for second and third cycles are very similar, i.e., it reaches the quasi-steady state for the opening phase.

As it is shown in figure 5.4, during the closing phase of valves, there are high cycle-to-cycle variations in the kinematics of the valves compared to the opening phase. In order to better illustrate these fluctuations, an extra cycle (third cycle) of 0 deg orientation is plotted in figure 5.4(a), which shows the difference in valve full closure timing, varying from $410\ ms$ for the second cycle to $640\ ms$ for the third one. These cycle-to-cycle variations in the closing phase are in accordance with previous experimental results of Dasi et al. [158] in an axisymmetric aorta, where they have reported fluctuations as high as 60%. Since high cycle-to-cycle variations are observed for the valve with 0 deg orientation by performing the third cycle, showing the same variations for other orientations does not provide any additional new information but adds significantly to the computational costs. Each cycle takes about 10 days to two weeks on over 300 cpus. Therefore, we only report the additional cycles for one orientation. Similar to a previous study for an anatomic aorta without the contracting LV [63], the leaflets during the closing phase show high asymmetry compared to opening phase. However, here, neither of the orientations show advantage in terms of symmetrical closure in their leaflet kinematics when different cycles are compared. For all of the orientations and cycles that both leaflets close during the first diastolic wave (E-wave), closing the second-to-close leaflet causes the other one to rebound after reaching the closed position; however, these rebounds can differ for different orientations and cycles, ranging from 2 to 36 deg. In addition to rebound during the end of the closing phase, all orientations show considerable rebounds during the beginning of the closing phase. These rebounds are higher for the second cycles (10 to 15 deg) and cause the other leaflets to rebound after reaching the closed position.

The transvalvular pressure difference between LV and aorta are plotted in figure 5.5 for the valve with 0 deg orientation during three consequent cycles. The pressure differences are associ-

ated with the average pressures on z-planes located immediately before the housing (LV side) and $0.5D$ after the housing (aortic side). As it is clear in figure 5.5, the transvalvular pressure follows the aortic flow rate waveform in a reversed manner as expected. It generates a pressure difference of $-30mmHg$ during systole while creating a small pressure difference for the diastole. Note that in numerical simulations, one can only prescribe flow or pressure boundary conditions (not both) to have a well-posed problem. Due to the prescribed velocity boundary condition for the aorta equal to the rate of volume change of LV, the pressure difference across the valve cannot be explicitly imposed. Therefore, the valve closure times are different for different cycles and orientations, while the regurgitation remains constant.

5.4 Vortex Dynamics

In this section, the vortex dynamics of aorta-LV assembly are illustrated for the second cycle of three different orientations to include the remaining flow features from the previous cycle. The contours of out-of-plane vorticity are visualized in figure 5.6 for time instants shown in figure 5.2 during a cardiac cycle. In order to show aorta and LV blocks in the same figure, the out-of-plane vorticity contours of aorta and LV blocks are plotted on mid-planes of 90 deg orientation valve and LV, respectively, for all orientations. The early systole (figure 5.6(a)) for all of the orientations starts with organized shear layers developed between two leaflets, the housing wall, and the sinuses as reported in the previous experiments [159] and simulations [63]. By reaching the peak systole (figure 5.6(b)), these layers rapidly break into small-scale structures and dominate the flow till the end of systole in the ascending aorta.

As shown in figure 5.2, the aortic flow rate waveform includes leakage flow [158], which helps keeping the valve closed during the diastolic phase. This leakage flow creates a strong jet by the start of first diastolic wave (figure 5.6(c)), which interferes with the mitral vortex ring, similar to the results of Le et al. [160]. Our results show that the part of the vortex core which is located near the anterior wall (aortic side) is significantly affected by the leakage flow jet while the vortex core near the posterior wall remains intact for a longer time as shown in figure 5.6(d). This accelerates the mitral vortex breakup as it propagates in direction of the LV apex (figure 5.6(e)). During this

time, a smaller shear layer is generated because of the second diastolic wave. As it is shown in figure 5.6(f), the small-scale structures created after the breakdown of mitral vortex rings and aortic backward flow jet persist till the end of diastole and affect the valve kinematics for the next cycle. In general, all three orientations show similar flow during the opening phase (early systole) but significant differences are observed during the closing (late systole and diastole) due to the dominance of the small scale turbulent structures in the aorta and LV, which contributes to the cycle-to-cycle and orientation differences seen in valve kinematics.

The three-dimensional vortical structures are visualized in figure 5.7 using the iso-surfaces of q-criteria [9] at different time instant marked in figure 5.2 from the second cycle for three orientations. As discussed before, qualitatively, similar organized vortical structures are observed shedding from valve orifices and sinuses for all of orientations during the early systole (figure 5.7(a)), which break down into asymmetric small scale chaotic structures after peak systole (figure 5.7(b)). In such an asymmetric flow, valve orientation can play an important role in leaflet kinematics. As it is shown in figure 5.7(a),(b), during the systole, the leftover vortical structures from the previous cycle inside the LV are elongated and sucked into the aortic root similar to the previous simulations [160]. The existence of these structures for the second and third cycles might be the underlying reason for the differences in leaflet kinematics observed during the beginning of the opening phase between the first and later cycles (see time interval of 0 to 30 ms in insets of figure 5.4). Figure 5.7(c) illustrates the strong jet created due to the backward flow, which perturbs the aortic side of the mitral vortex ring (figure 5.7(d)), causing the ring to be inclined toward the posterior wall. The asymmetric vortex ring breaks up and creates worm-like structures (figure 5.7(e)) inside the LV which persist till the end of the cycle (figure 5.7(f)).

To test the scaling law proposed in §4, we plotted the location of the second mitral vortex ring in the second cycle of the 0 deg orientation (figure 5.8(a)). In order to use the scaling, only the first diastolic wave shown in figure 5.2 (E-wave) and mitral orifice diameter are considered for the calculation of non-dimensional numbers since only this part of the LV flow rate drives the first diastolic mitral vortex ring. This gives a Reynold number of $Re_{ave} = 536$ and a non-dimensional

period of $T^*_{ave} = 3.03$. Our results show no trailing jet behind the formed vortex ring as the low stroke ratio of 3.03 suggests based on the formation number discussed by Gharib et al. [109]. As it is shown in figure 5.8(b), the scaling law collapses the location of the mitral vortex ring with an R-squared of 0.99. Note that we only tracked the first mitral ring before its high interaction with the leakage flow.

5.5 Shear Stress

In order to evaluate the mechanical forces acting on blood cells, viscous stress distributions are studied for all three valve orientations in the ascending aorta. The second-order shear stress tensor σ_{ij} is reduced to a coordinate-independent scalar shear stress τ based on the formulation outlined by Apel et al. [161] as

$$\tau = [\frac{1}{6}\sum_{i,j=1}^{3}(\sigma_{ii} - \sigma_{jj})(\sigma_{ii} - \sigma_{jj}) + \sigma_{ij}\sigma_{ij}]^{1/2} \tag{5.1}$$

Figure 5.9 shows the histograms of scalar shear stress in the ascending aorta for three valve orientations at time instants marked in figure 5.2 during the second cycle. Similar to subsection5.4, the results of the second cycle are investigated to include the remaining flow features from the previous cycle. The histograms show the percentile of the number of occurrences $f(\tau)$ of a scalar shear stress value τ in intervals with width $0.1\ dyne/cm^2$ to the total number of occurrences. Figure 5.9(a) shows the percentile of occurrences of scalar shear stress for shear values with the highest occurrences while figure 5.9(b) shows the percentile of shear stresses with high values. It can be observed that the valve orientation does not significantly affect the distribution of shear stress in the ascending aorta. Figure 5.9(a) shows that for all of the orientations, the most frequent values of shear stress increase as the flow reaches the peak systole (times t_a and t_b). This trend continues until we reach the peak diastole (time t_c) due to the fact that most of the domain becomes affected by the high shear flow generated near valve and sinus areas. Later, the high occurrence values of shear stress decrease to their lowest at time t_f as flow comes to rest.

The histogram of figure 5.9(b) illustrates a correlation between the occurrence of high-value

shear stress and the flow rate as reported in previous simulations [63]. It can be observed that higher histogram values occur at peak systole (t_b) and mid systole (t_a), respectively. Histogram values of peak diastole (t_c) show higher values compared to other time instant (t_e and t_f). Additionally, for all of the orientations, $\%99.5$ of the shear stresses observed in the ascending aorta were less than $150\ dyne/cm^2$ which is in the range of previous simulations and experiments reported by Ge et al.[20].

5.6 Platelet Activation

In this work, the performance of MHV at different orientations is investigated in terms of shear-induced platelet activation in an Eulerian framework. In order to ensure the model-independent results, two platelet activation models are considered: (1) linear level activation, which is the integration of shear stress times exposure time on the platelet path [162]; and (2) the Soares model, which accounts the effects of loading rate and sensitization [163]. The reader is referred to [136] for details of the implementation, validation, and sensitivity studies of our platelet activation framework of these models.

The integration of platelet activation in the ascending aorta is shown in Fig. 5.10 for three different implantation orientations during two consecutive cycles using linear and Soares models. For the second cycles, while the remaining flow features from the previous cycle is considered in the domain, in order to compare the platelet activation levels generated at each cycle, the platelet activation from the previous cycle is not included, i.e., the platelet levels start from zero for the second cycle similar to the first one. The platelet activation of each model is normalized by the total platelet activation in 0 deg orientation at the end of the first cycle, i.e., the normalized activation for 0 deg orientation is 1 at the end of the first cycle regardless of the activation model. It is clear from Fig. 5.10 that the implantation orientation does not have a major effect on the platelet activation regardless of the activation model with less than 8% difference between the orientations at the end of each cycle. Comparing results of different cycles shows that the remaining flow features from the first cycle change the total platelet activation at the end of the second cycle by about 106% and 73% the total platelet activation in the first cycle for linear and Soares models, respectively.

5.7 Discussion

The kinematics of the valves with different orientations showed that during the opening phase, there are negligible cycle-to-cycle variations between leaflets movement after the first cycle, which is attributed to the laminar and reproducible feature of the flow during the early systole (Fig. 5.6(a)), consistent with previous experimental study in a straight aorta [159], i.e., flow remains organized and laminar at early systole even in the anatomic LV and aorta. During this phase, valves with different orientations show relatively symmetrical kinematics in terms of synchronous movement of the leaflets, similar to the previous study without the contracting LV [63]. At near peak systole, as vortex shedding of the leaflets starts (Fig. 5.6(b)), the small scale, turbulent-like structures emerge, which continue till the closing phase of the valves (Fig. 5.7(c)). The presence of these structures causes cycle-to-cycle vorticity variations in the flow in the aortic root, which could cause significant fluctuations in the forces exerted on the leaflets during different cycles; therefore, for the first time, to the best of the knowledge of the author, elucidating the reasons behind cycle-to-cycle variations in leaflet kinematics (Fig. 5.4), which were also observed in a previous experimental study [159]. Consequently, in stark contrast to the previous study without the contracting LV [63], where the 0 deg orientation showed less asymmetry and rebound, our results show that there is not a preferred valve orientation in terms of symmetrical closing and minimum rebound of the leaflets, which are important parameters in determining the amount of intermittent regurgitation [164].

The shear stress histograms illustrated that valve orientation does not have a significant effect on the distribution of viscous shear stress in the ascending aorta (Fig. 5.9), which is consistent with the previous simulations [63] for a flow in ascending aorta driven without LV. Recently, in-silico results of Gulan and Hozler [165] showed that while the valve orientation has major effects on local shear stress distribution but its effects on spatially averaged shear stress are not considerable. In addition, the animal study of Kleine et al.[144] concluded that the orientation of BMHV did not have a significant effect on the Reynolds stresses. While the Reynolds and viscous shear stresses are different metrics but putting together these studies suggests that valve orientation does not have a significant effect on the hemodynamic stresses exerted on blood elements. This is further

confirmed by calculating shear-induced platelet activation using two different mathematical models in the ascending aorta for two cycles, which showed less than 8% difference in the total platelet activation levels among different orientations.

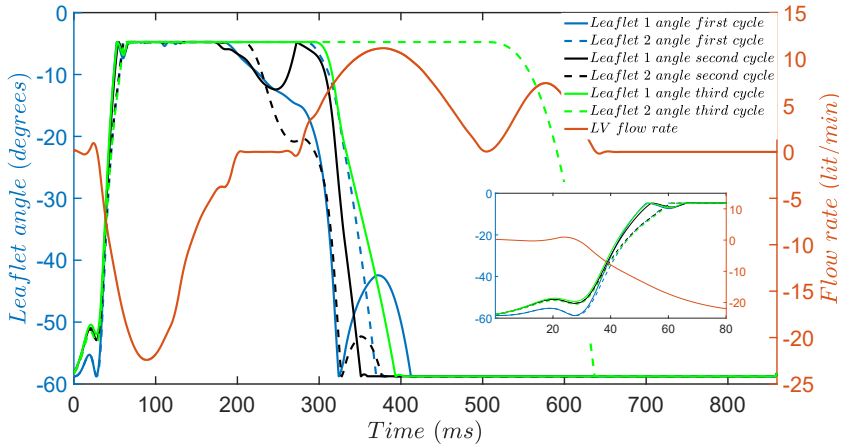

(a)

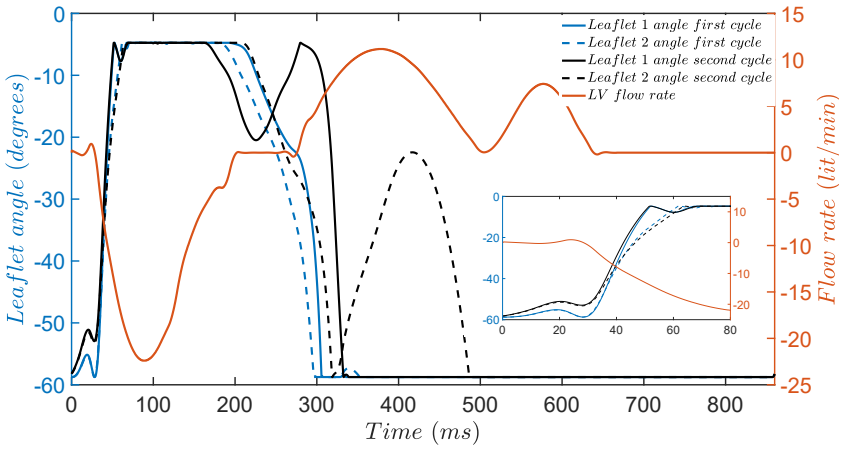

(b)

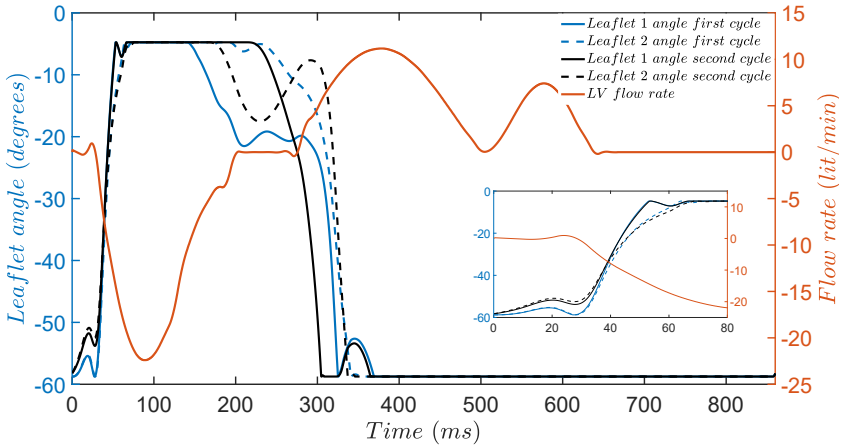

(c)

Figure 5.4: Leaflet kinematics for (a) 0, (b) 45, and (c) 90 deg orientations. The insets in each figure are zoomed-in views from the opening phase of leaflet kinematics.

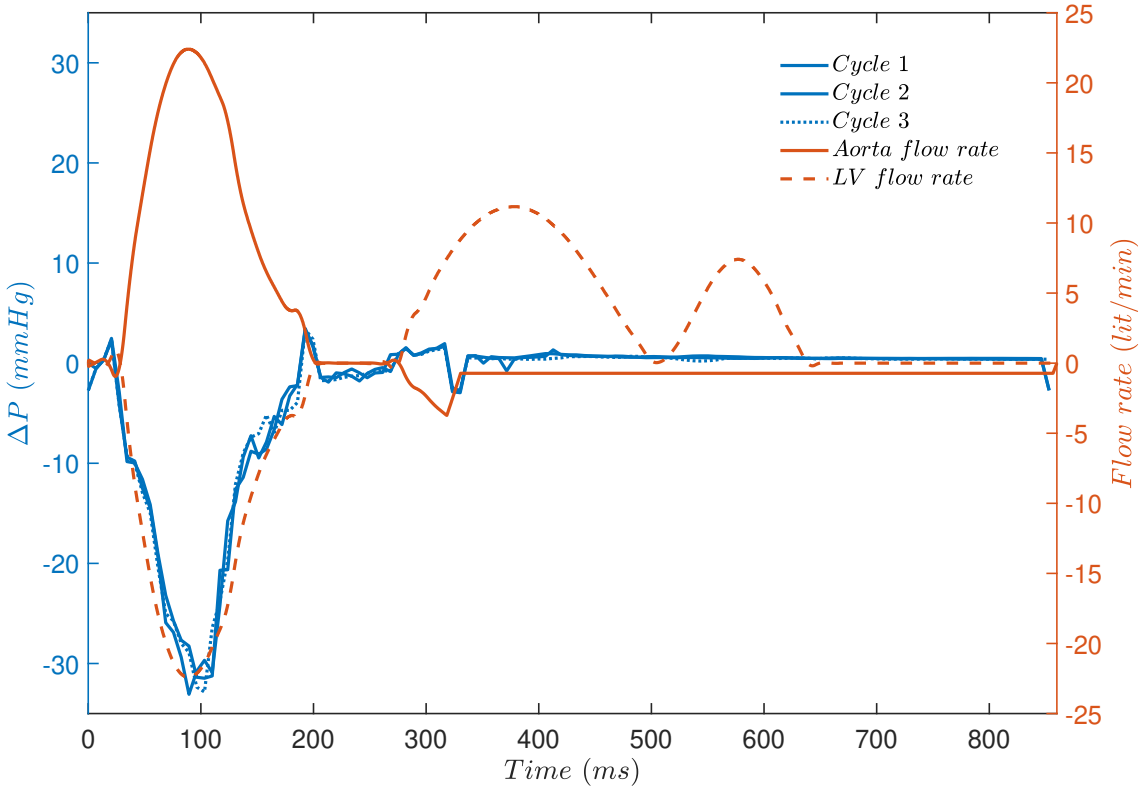

Figure 5.5: The transvalvular pressure difference between LV and aorta for the valve with 0 deg orientation during three consequent cycles.

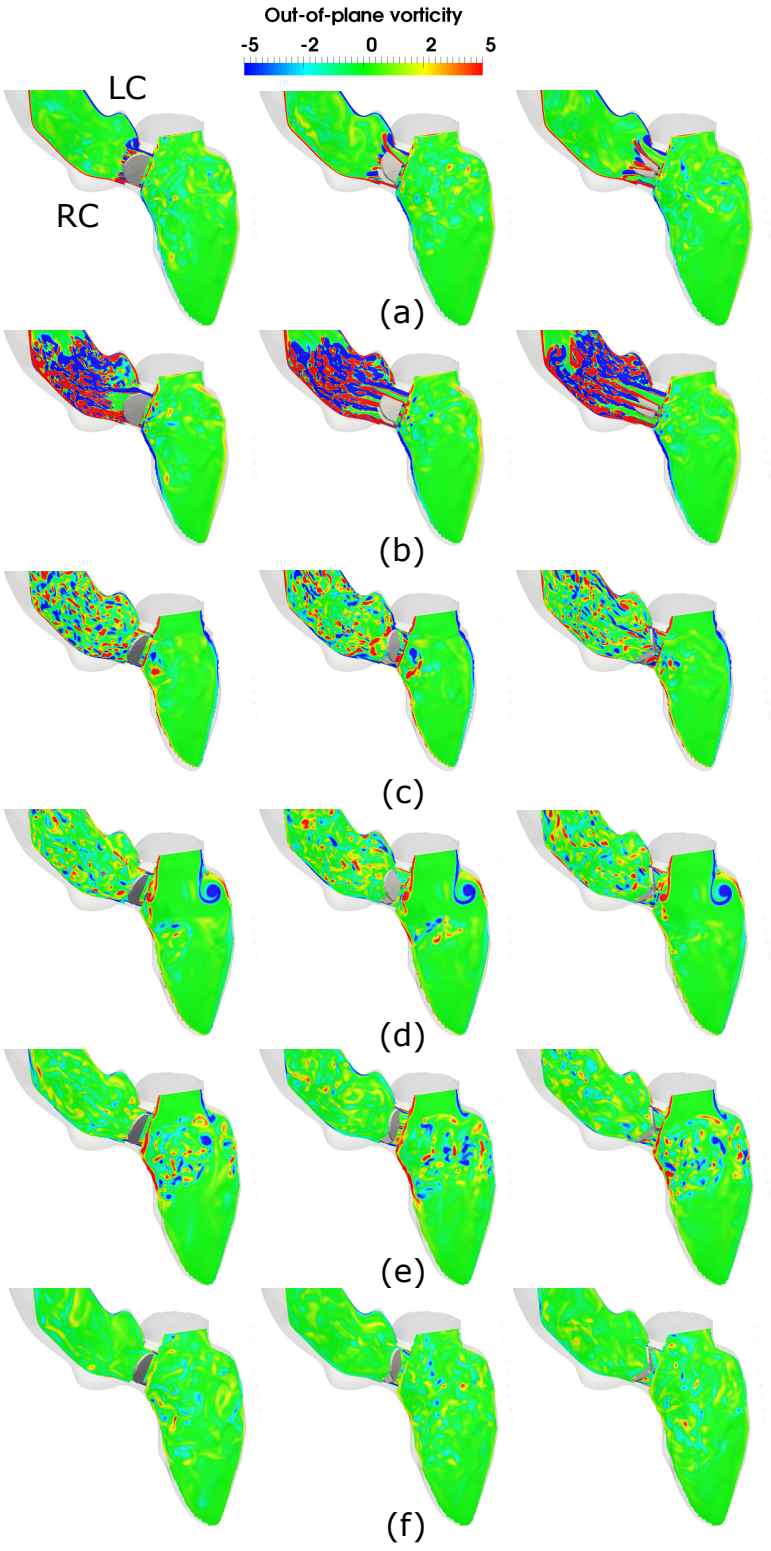

Figure 5.6: Instantaneous non-dimensional out-of-plane vorticity ($\Omega D/U$) for 0 deg (left), 45 deg (middle), and 90 deg (right) orientations. a, b, c, etc., correspond to the time instants marked in figure 5.2 within the cardiac cycle.

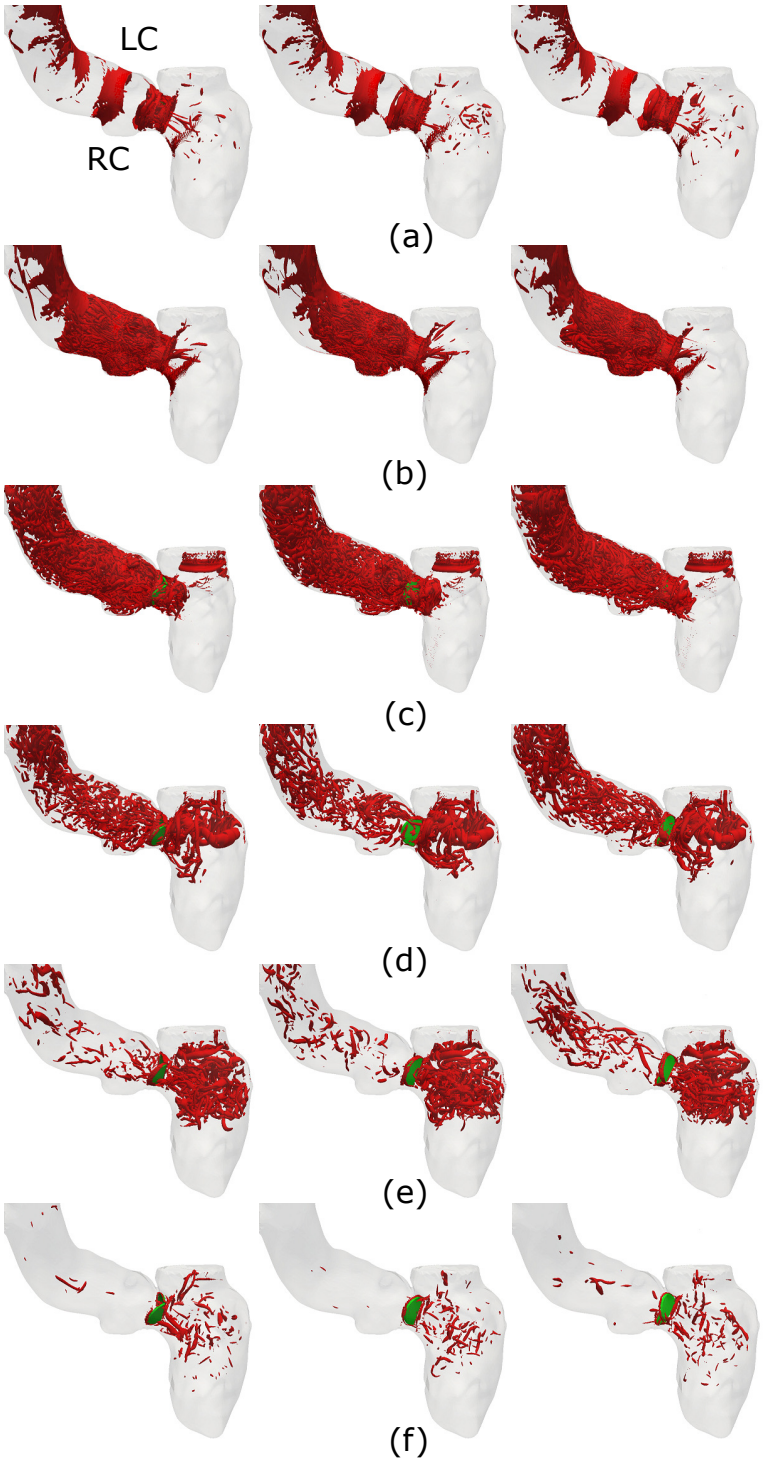

Figure 5.7: Vortical structures are visualized by iso-surfaces of q-criteria for 0 deg (left), 45 deg (middle), and 90 deg (right) orientations. a, b, c, etc., correspond to the time instants marked in figure 5.2 within the cardiac cycle.

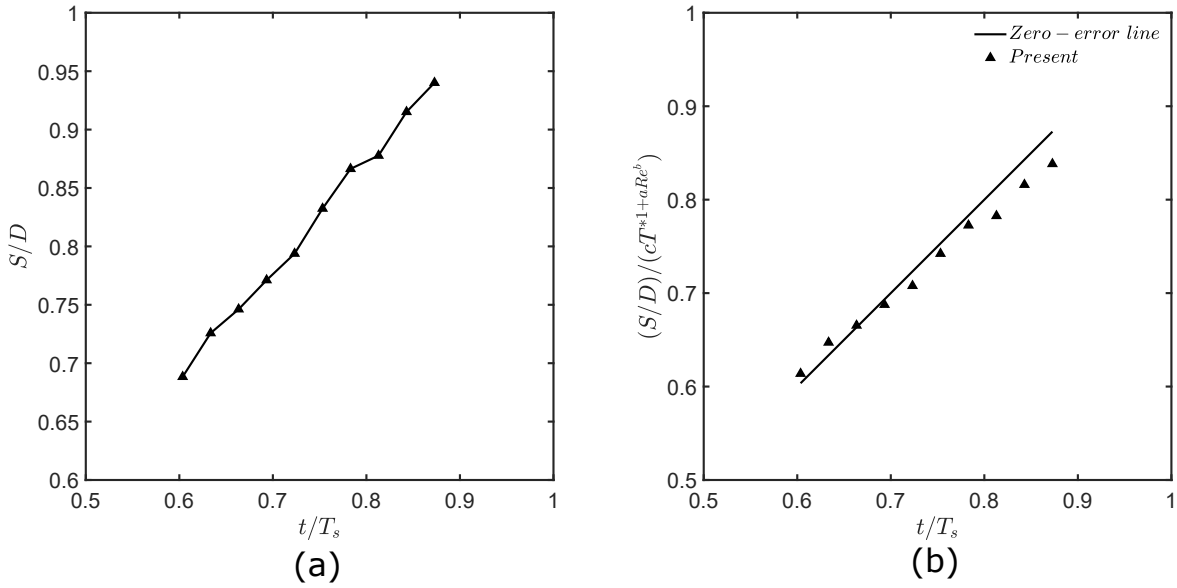

Figure 5.8: Location of the first mitral vortex ring (a) before and (b) after the scaling for the second cycle of the 0 deg orientation.

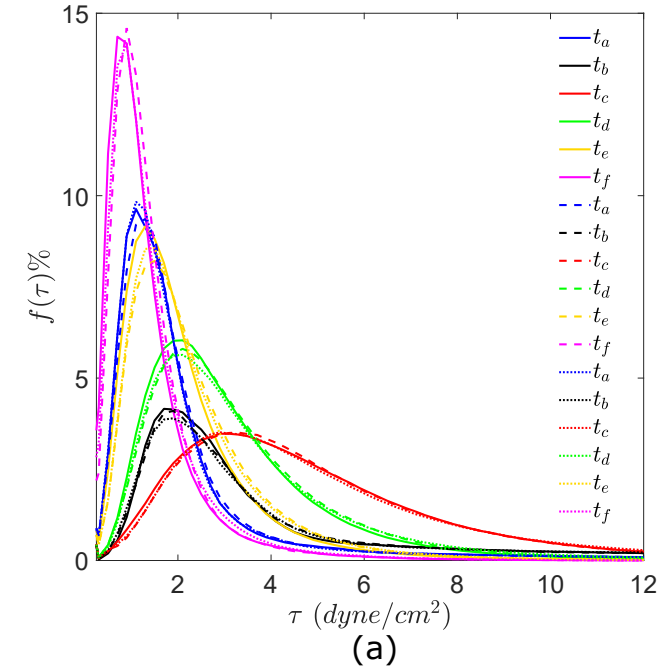

(a)

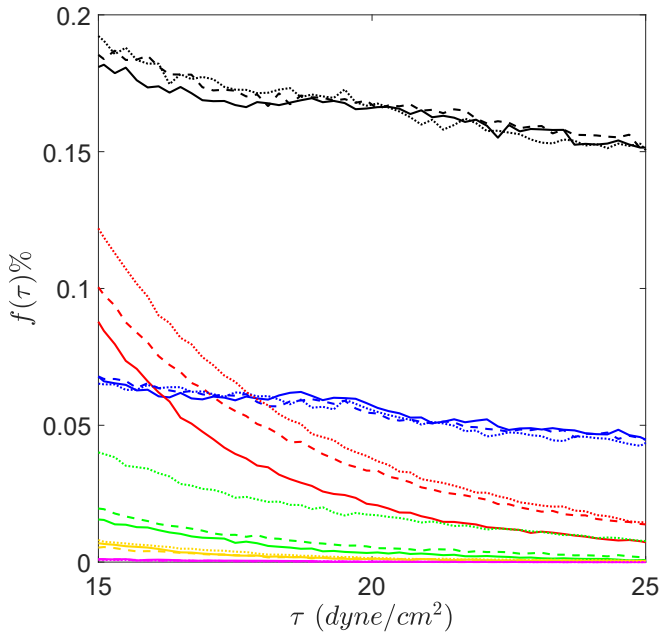

(b)

Figure 5.9: Histograms of scalar shear stress in the ascending aorta for 0 deg (solid lines), 45 deg (dashed lines), and 90 deg (dotted lines) orientations during the second cycle for: (a) scalar shear values with the highest percentile and (b) high scalar shear values. f is the percentile of the number of occurrences of a scalar shear value τ in intervals with width $\Delta\tau = 0.1\ dyne/cm^2$ to the total number of occurrences. a, b, c, etc., correspond to the time instants marked in figure 5.2 within the second cardiac cycle.

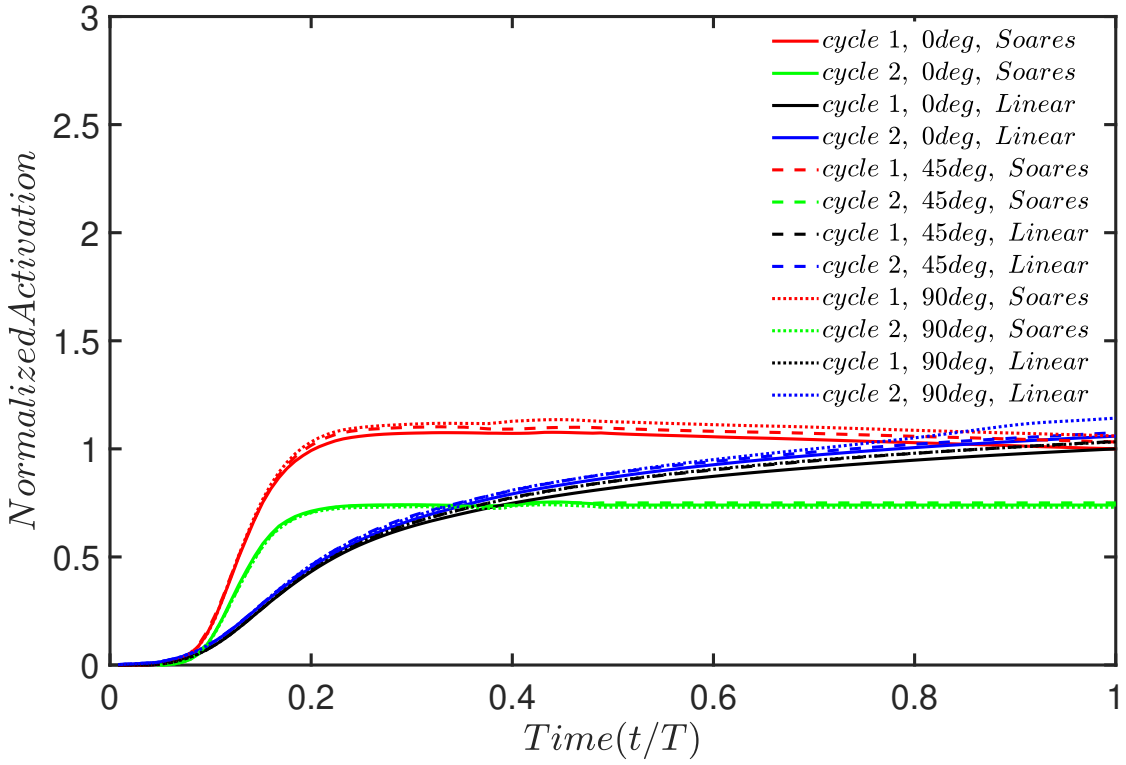

Figure 5.10: The integration of platelet activation over the ascending aorta for 0 deg (solid lines), 45 deg (dashed lines), and 90 deg (dotted lines) orientations during two consecutive cycles using different models. The platelet activation for each model is normalized by the total platelet activation in 0 deg orientation at the end of the first cycle.

6. VORTEX DYNAMICS OF BIO-PROSTHETIC HEART VALVES (BHV)

In this chapter the coupled CURVIB flow solver and FE structure solver, incorporating non-linear and anisotropic material model and proposed contact model, will be used for FSI simulations of a BHV in a straight aorta for a complete cardiac cycle. In §6.1, a literature review for the contact modeling and FSI simulations of BHV are provided. The computational details of the FSI simulations are discussed in §6.2. The kinematics of the valves are presented for the FSI simulation in §6.3 and compared with the dynamic simulation results. The velocity field, vortex dynamics, and shear stress distribution in the straight aorta are addressed in §6.4, §6.5, and §6.6, respectively. In §6.7, two different mathematical models of platelet activation are used for investigating the platelet activation levels in the straight aorta. Finally, the conclusions of this simulation are discussed in §6.8.

6.1 Background

The main function of heart valves (HV) is to ensure unidirectional flow through the cardiovascular system with the minimum backward flow (regurgitation) during specific time intervals in a cardiac cycle. Despite the fact that HVs have different structural features, e.g., mitral valves have two leaflets while aortic valves have trileaflet structure, all of them use the proper coaptation of the free edges of their leaflets to prevent regurgitation during the closing phase of the HVs, which is an important parameter in determining the valvular health [64]. The proper modeling of the coaptation of leaflets, i.e., contact modeling, in numerical simulations is not straightforward and adds to the challenges of modeling of tissue heart valves, e.g., non-linearity and anisotropy of the materials, and high deformation [22, 166].

One of the main challenges of tissue heart valve simulations is the inter-leaflet contact handling during the closing phase of valves in a physiological cycle. The solution to the contact problem breaks into two main steps: (1) contact detection and (2) interpenetration prevention. At each time step, both of these steps must be applied; therefore, it could be computationally expensive.

In order to reduce the computational cost of the first step, some studies restricted their contact detection to a prescribed region near the free edges [10]. Others implemented a more general and efficient approach by dividing each leaflet mesh into smaller regions (control cells) and searching for contact only in a smaller number of grid points [78].

In order to take the second step efficiently, Kim et al [6] used master-slave method with three virtual vertical planes located between leaflets as slave surfaces upholding a 120^o angle, which is based on threefold symmetry assumption. Later, Borazjani showed threefold symmetry breaks in early systole and adopted the penalty method [78]. The penalty method has been widely used to handle the interpenetration problem [10, 65, 167, 168, 66, 67] due to easy implementation. The penalty method uses predefined forms of contact force, e.g., equation 3.6, which may be applied to the node contacting an element in the direction of the element normal [90]. The contact forces applied in this manner are generally prone to convergence problems [169] and are based on numerical experimentation for a specific problem [24] and may not be suitable for different configurations [170], which can cause interpenetration or non-smooth edges if applied in lower or higher than required magnitudes, respectively. To overcome these problems the Lagrange multiplier method[169] can be used, which preserves the impenetrability constraints; however, it requires the solution of an augmented system of equations, which is not feasible for high-resolution simulations. Applying the variational non-smooth technique to the contact problem has been done both implicitly [171] and explicitly [79]. The more recent variational-based explicit contact modeling method, termed decomposition contact response (DCR), [79] applies the impenetrability constraints and exchange of momenta separately. In this method, the penetration is measured using signed volume of intersection of elements, which is removed using closed point projection. The transfer of momentum is performed using self-equilibrating impulses to the nodes participating in the impact [79].

In this study, we employ a novel and efficient method, described in §2.3, which applies the impenetrability constraints and exchange of momenta independently, similar to reference [79]; however, the transfer of momenta between the contacting bodies is applied using the simple particle-

particle impact equations with some considerations using coefficient of restitution. The validity of the proposed method is established by performing two impact benchmark problems and comparing to a set of experimental BHV data as discussed in §3.3. Furthermore, the smooth edges and zero gaps between the leaflets for this method are compared to the results taken by the penalty method of equation 3.6.

In general, there are three main computational approaches for modeling BHV: structural mechanics (SM), computational fluid dynamics (CFD), and FSI [22]. SM models are divided into two categories: static SM, which uses a constant uniform pressure loading applied to a fully closed valve [172] and dynamic SM, which considers the time variations of pressure waveform in the cardiac cycle [173]. Early studies used linear isotropic material models to simulate the BHV [174, 175]. Petterson et al. [176] showed the effects of material non-linearity on compressive and tensile stress distributions on the leaflet. Later, the influence of anisotropy has been investigated and shown that a small amount of anisotropy can significantly affect the mechanical behavior of the valves [177]. Driessen et al. [178] used an isotropic matrix with fiber-reinforcement to model the anisotropic linear material model. Kim et al. [179] used a Fung-type elastic constitutive model to consider anisotropy and non-linearity of the leaflets based on the experimental results. The thin structures of leaflets may be modeled considering in-plane stresses only, i.e., membrane elements [180], or in-plane and bending stresses, i.e., shell elements [181]. The experimental results of Iyengar et al. [182] showed that due to large deformation of BHVs, bending stresses are substantial during cardiac cycle. The first model presented by Kim et al. [179] considered a linear isotropic approximation of moment-curvature relationship. Later, a nonlinear anisotropic shell element has been presented from three point bending tests [183] and added to Fung-type membrane model [6].

In order to study the details of fluid-induced pressure and shear stresses on the leaflets, FSI analysis is required. For coupling the fluid dynamic equations of blood flow with structural mechanics, two main approaches are available [184]: the boundary conforming methods, in which fluid grid moves with boundary, and non-boundary conforming methods, in which fluid grid does not moves with the moving boundary. In boundary conforming methods, e.g. the Arbitrary Lagrangian Eule-

rian (ALE) formulation [185], the fluid mesh needs to be displaced and deformed constantly, which makes the three-dimensional simulations of HVs very expensive due to high deformations and adds artificial diffusivity due to projection of the fluid solution from the older grid to the new one [22]. In the non-boundary conforming methods, e.g., Immersed Boundary (IB) methods [43], the movement of boundary does not require the fluid mesh update, which reduces the computational cost. However, in these methods, high resolution grids are required near the immersed fluid-structure interface, due to diffuse interface implementations. To overcome this drawback, sharp-interface curvilinear immersed boundary (CURVIB) method is introduced [186, 42, 187]. Borazjani [78] coupled the CURVIB method with nonlinear large deformation FEM to simulate FSI of a BHV, while neglecting the bending stiffness of the structural model. Gilmanov et al. [188] extended the CURVIB method to fluid-shell interaction but only simulated the systole phase of cardiac cycle. In this chapter, the FSI simulation of a BHV in a straight aorta is performed for a thin shell element with material non-linearity and anisotropy, incorporating the new physic-based contact method.

6.2 Computational Details

In order to investigate the dynamics of the BHV more realistically during a physiological cardiac cycle and study the hemodynamics of the flow in the aorta, the FSI simulation of a BHV is performed. Here, we coupled the FE and CURVIB using the strong coupling of Borazjani [48], which used under-relaxation with Aitken acceleration technique to improve the stability of the coupling. Additionally, the proposed contact model of §2.3 is implemented for the closing phase of the valve dynamics. The non-linear and anisotropy material model for a pericardial BHV of Kim et al. [6] (see §2.2.3) is used as the leaflet constitutive equations for both bending and membrane responses similar to the dynamic simulations of §3.3.5; however, here, only an asymmetric fiber orientation is simulated (figure 3.14(b)). The same leaflet thickness, height, and radius of §3.3.5 is considered for the geometry of the BHV. As shown in figure 6.1, the BHV is mounted on a rigid support structure and stent and placed in an straight aorta. An inlet constant velocity is applied at the inlet according to the waveform illustrated in figure 6.2. A convective outflow is considered at the outlet and no-slip boundary condition is applied at the walls of the aorta.

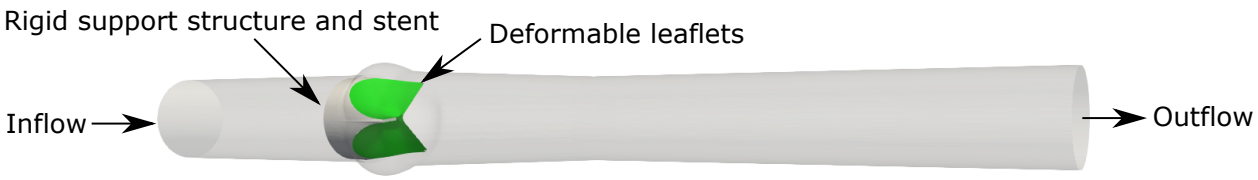

Figure 6.1: Computational domain for FSI simulation of a BHV in a straight aorta. The inflow is a pulsatile physiological flow and a convective outflow is applied at the outlet. No-slip boundary condition is considered for the aorta walls.

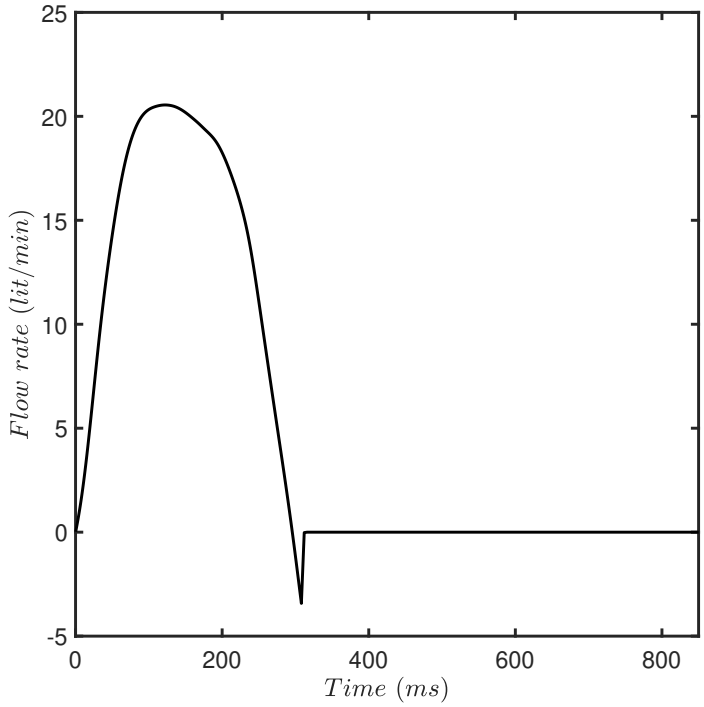

Figure 6.2: The physiological inflow waveform during one cardiac cycle ($850\ ms$) is used for the inlet boundary condition of the FSI simulation of a BHV in a straight aorta.

The straight aorta (figure 6.1) is discretized using a curvilinear mesh with $201 \times 201 \times 241$ grid points in two transverse and streamwise directions, respectively. A triangular mesh with 873 grid points is used for the discretization of each leaflet.

The equations are non-dimensionalized using the aortic diameter of $D = 25.82\ mm$ and peak systolic velocity of $U = 0.654\ m/s$ at $71\ bmp$, which gives a physiological peak systolic flow rate

[189] of $20.55\ lit/min$. By considering the blood density and viscosity of $\rho = 1200\ kg/m^3$ and $\mu = 5.6 \times 10^{-3} Pa.s$, respectively, the peak systolic Reynolds number of $Re = 3818$ is achieved, which is within the physiological range [190]. A nondimensional time step size of 0.005 is chosen for this simulation, which is equivalent to a physical time step size of $0.194\ ms$, leading to a total of 4311 time steps to cover the complete cardiac cycle with a period of $850\ ms$. In this simulation, utilizing the SC FSI algorithm, reduced the residuals by 3 orders of magnitude in 3-12 strong coupling iterations.

6.3 Leaflet Dynamics

The deformations of the BHV colored by major in-plane principal Green-Lagrange strain (MIPE) from the FSI simulation are shown in figure 6.3 for different time steps from the side and top views. Four snapshots on the first column show the status of the BHV in the systolic phase while the second column illustrates that of the diastolic phase. One of the main differences in the kinematics of BHV in FSI simulations compared to dynamic simulations (see §3.3.5) is the latency of the response of the BHV to hydrodynamics forces. Note that while the velocity and pressure boundary conditions implemented for FSI and dynamics simulations, respectively, are not necessarily relevant but they both are taken from physiological human cardiac cycles. The time that it takes for the BHV to reach the state of time $t = 0.03s$ in figure 6.3 is way longer than that of the similar state for the dynamic simulation ($t = 0.008s$ in figure 3.18). This difference is due to the uniform loading of the dynamic simulations in contrast to the transient hydrodynamic loading in FSI simulations, which previously has been reported [24, 10]. According to figure 6.3, it takes about $0.06s$ for the valve to rapidly open then there is an approximate $0.16s$ maximum valve opening state ($t = 0.06s$ to $t = 0.22s$), and finally valve closes in $0.11s$ ($t = 0.22s$ to $t = 0.32s$). The duration of these events is in good agreement with previous experimental and numerical studies [191, 192, 10, 193]. Note that the valve closure consist of two stages; the slow closure that occurs approximately from $t = 0.22s$ to $t = 0.31s$ and rapid closure, which happens during the reverse flow (from $t = 0.31s$ to $t = 0.32s$). The difference in valve velocity during these stages generates vortex rings, which will be discussed in §6.5. Additionally, the FSI results show that the

valve starts to close during the forward flow ($t = 0.22s$), which was reported in the previous FSI simulation [24].

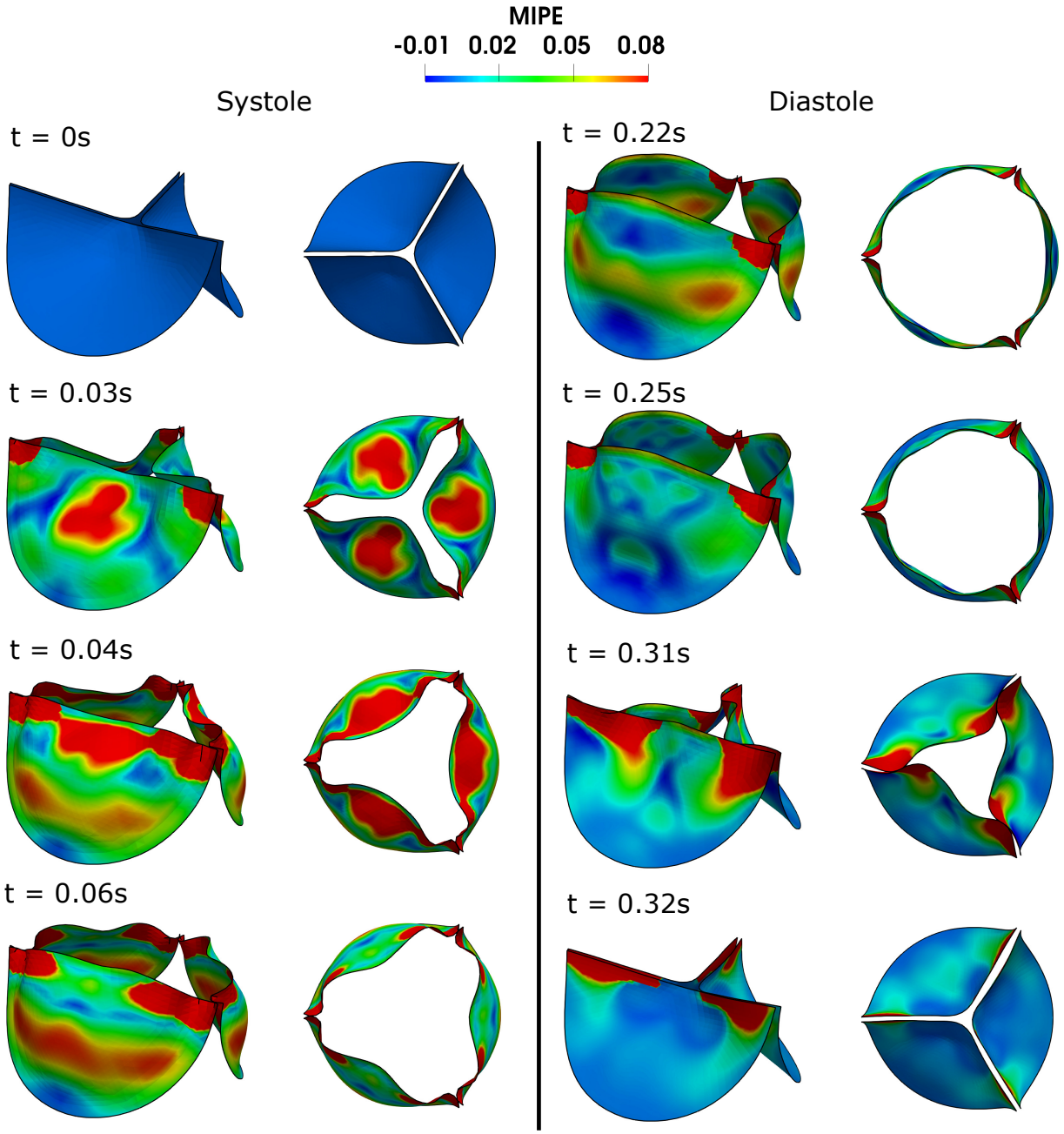

Figure 6.3: Deformation of the BHV from FSI simulation during the cardiac cycle, colored by major in-plane principal Green-Lagrange strain (MIPE) for 4 time instants of systolic (column 1) and diastolic (column 2) phases from the side and top views.

As it is shown in figure 6.3, during the whole opening phase, similar to the dynamic simulation, the commissures show the highest strains; however, during the last stages of the opening phase, the belly region also shows high values, which is illustrated as the red patches on the belly at $t = 0.05 - 0.06s$. This is in contrast to the dynamic simulation, where the belly remains as a low-strain region (see figure 3.18). In order to better illustrate the differences between the valve kinematics for the dynamic and FSI simulations, the perpendicular bisection plane of one of the leaflets is illustrated in figure 6.4(a,b) during the opening and closing phases, respectively. The red and blue lines correspond to the dynamic and FSI simulations, respectively. Note that the results did not show major differences between the dynamics of different leaflets; therefore, only the bisection of one of the leaflets is presented in figure 6.4. One of the main differences between the deformation of the leaflets is that in the dynamic simulation, the free edges of the leaflets deflect prior to the belly region, while in the FSI simulation, the belly undergoes high deflection first, i.e., in the dynamic case, the deformation starts with the free edges in contrast to FSI case, which the deformation begins in the belly region. The leaflet kinematics in the FSI simulation is according to the previous in-vivo [194] and in-vitro [195, 182] observations and FSI data [189, 192, 10], and as outlined by [10] is due to the non-uniform pressure distribution over the leaflet. This is shown in figure 6.5(a) for the opening phase, which illustrates a lower hemodynamic pressure loading on the free edges with the maximum loading in the belly region.

During the closing phase, the leaflets show similar strain distribution for the FSI and dynamic simulations, as seen in the second column of figure 6.3 and 3.19, respectively. However, during the fully closed state, the dynamic case ($t = 0.35s$) shows significantly large strain values, while the FSI case ($t = 0.32s$) shows comparable strain values compared to the previous time instants. This is due to the different boundary conditions applied for the two simulations. As it is shown in figure 6.4(b), the pattern of the deformations during the closing phase for both of the simulations are similar except for the state of number 4. Similar to the opening phase, this stems from the pressure distribution for the FSI case, while in contrast to the opening phase, here the pressure contours show relatively uniform pressure distribution (figure 6.5)(b)), which resembles the

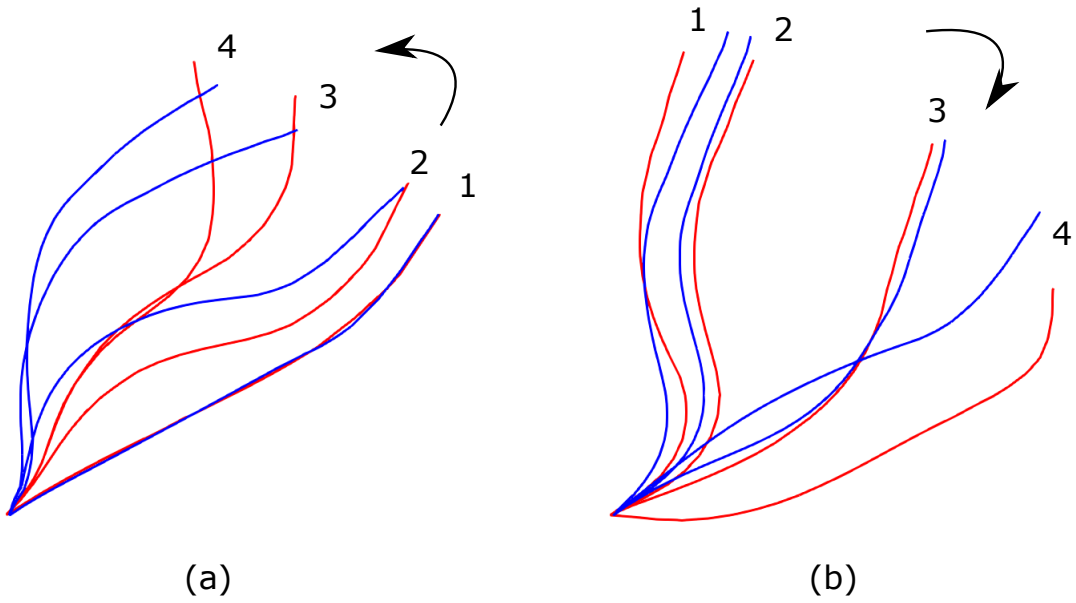

Figure 6.4: perpendicular bisection plane of the leaflet for (a) opening and (b) closing phases. The red and blue colors correspond to dynamic and FSI simulations, respectively. The numbers correspond to the row numbers in figures 3.18 and 3.19 for dynamic simulations of the valve with asymmetric fiber orientation and figure 6.3 for FSI simulation.

uniform pressure distribution of the dynamic case.

It is interesting that the swirling motion discussed for an asymmetric fiber orientation of a dynamic simulation in §3.3.5 is observed here, too. For a better illustration, the swirling motion of the dynamic and FSI simulations are shown in figure 6.6. It is clear that while the swirling motion is repeated in FSI simulations but it shows a reverse motion compared to the dynamic one. The small non-uniformity in the pressure distribution might be the underlying reason as the leaflets during this time are very unstable and move rapidly.

6.4 Velocity Field

In this section, the velocity field of the straight aorta around the valve is discussed. As the valve opens and closes the shape of the aortic orifice changes, which has a direct consequence on the shape of the aortic jet. Figure 6.7 shows the contours of velocity magnitude on several axial locations during the opening and accelerating phases. The slices are located at $z/D = 0.1, 0.5, 1,$

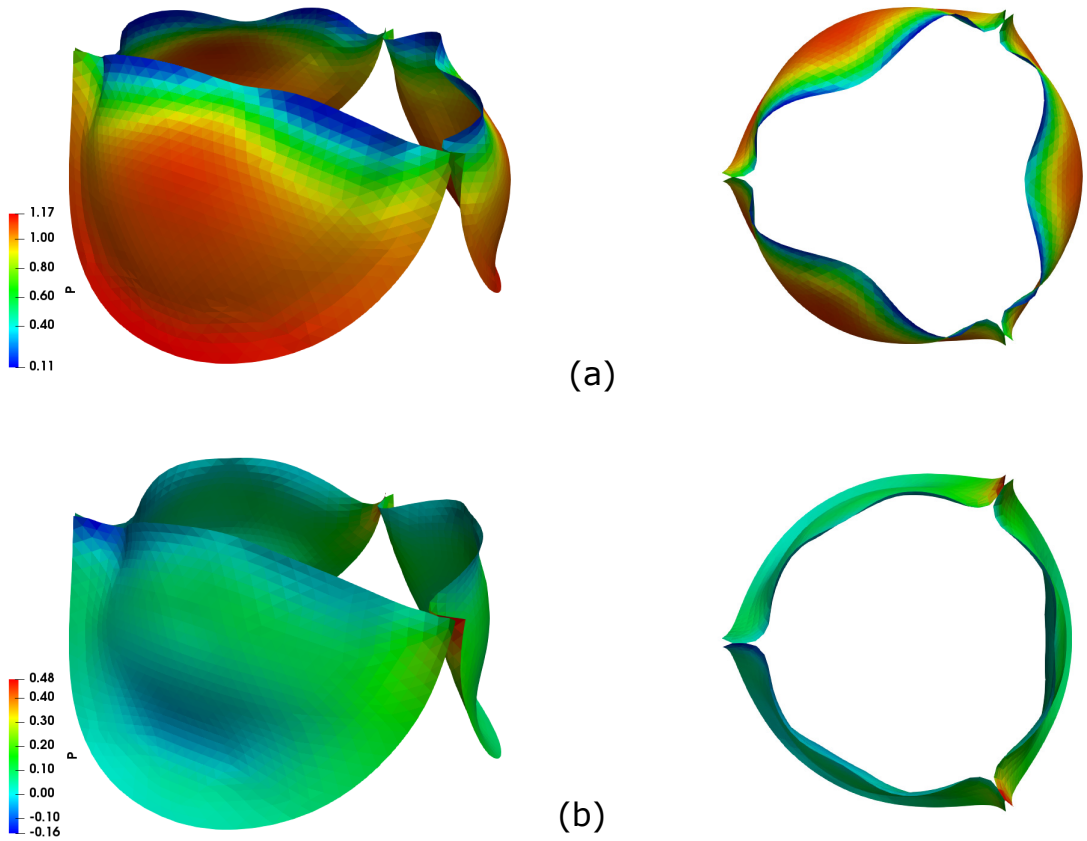

Figure 6.5: Pressure distribution (KPa) for (a) opening ($t = 0.06s$) and (b) closing ($t = 0.25s$) phases of the FSI simulation from side and top views.

and 1.5 from the edge of the BHV in an open position. In figure 6.7(a), when $t = 0.06s$, the first slice shows a hexagon shape representing the shape of the valve during the opening phase; however, the second and third slices show triangular shapes, which are due to the triangular shape of the opening during the earlier times (figure 6.3 at $t = 0.03s$). An interesting observation is that the orientations of these triangles are flipped from the second slice to the third one. This phenomenon is called "jet flipping" and is previously studied for non-circular stationary jets [196, 197] at axial location in the range of $z/D = 0.1$ and 1 and is recently observed in a FSI study of a BHV [10]. The last slice at this time instant does not show a relatively circular shape, which might be due to the inertial effects of the fluid on the shape of the jet. In figure 6.7(b), which shows the shape of

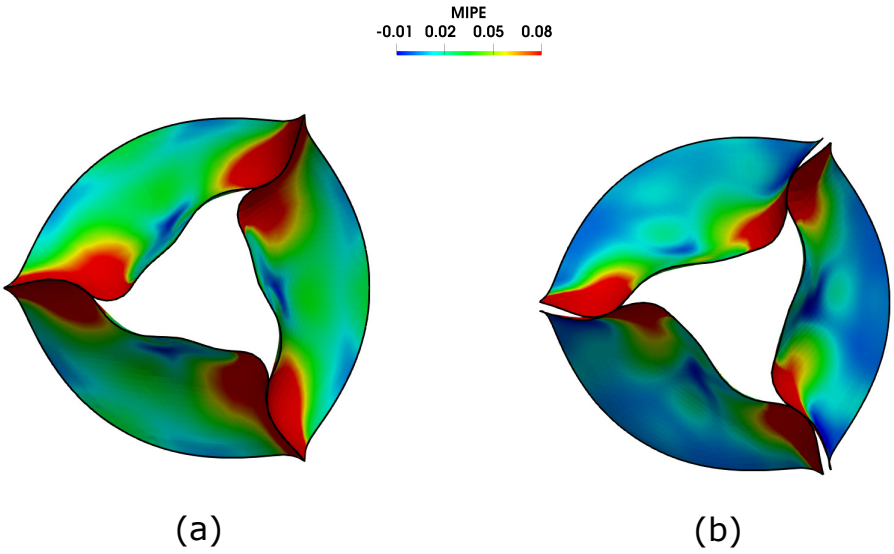

Figure 6.6: Comparison of the swirling motion of the BHV leaflets during the closing phase for (a) dynamic ($t = 0.21s$) and (b) FSI ($t = 0.31s$) simulations for an asymmetric fiber orientation.

the jet at $t = 0.08s$, the location of the flipped jets are moved to the third and fourth slices. During this time, the flow reaches the peak systole and the instabilities start to emerge, as the shapes of the triangles begin to get distorted. These instabilities are amplified in figure 6.7(c,d) as there are no visible well-defined shapes are observed for the third and fourth slices.

Figure 6.8 shows the contours of axial velocity component on y-plane during the complete cardiac cycle. At early systole (figure 6.8(a)), the velocity contours show well-organized jets, shaped based on the valve opening geometry. As the flow proceeds into the mid-systole (figure 6.8(b)) the instabilities start to emerge on the circumference of the jet, while the shape of the jet front is still well-defined. At the same time, a retrograde flow starts to occur near the valve in the sinus area, which is colored with dark blue. In the peak systole, as shown in figure 6.8(c), the instabilities are intensified, which leads to the oscillatory aortic jet [198]. This shading continues during the forward flow (6.8(d)) and occurs approximately at $z/D = 2$ with a core jet velocity of about $2m/s$, which is consistent with the in-vitro observation of Hasler and Obrist [193]. The impingement of the jet on the aortic wall causes stagnation points with high pressure, which develops a retrograde flow in the sinus area as shown in dark blue in figure 6.8(c,d). As the flow starts to decelerate

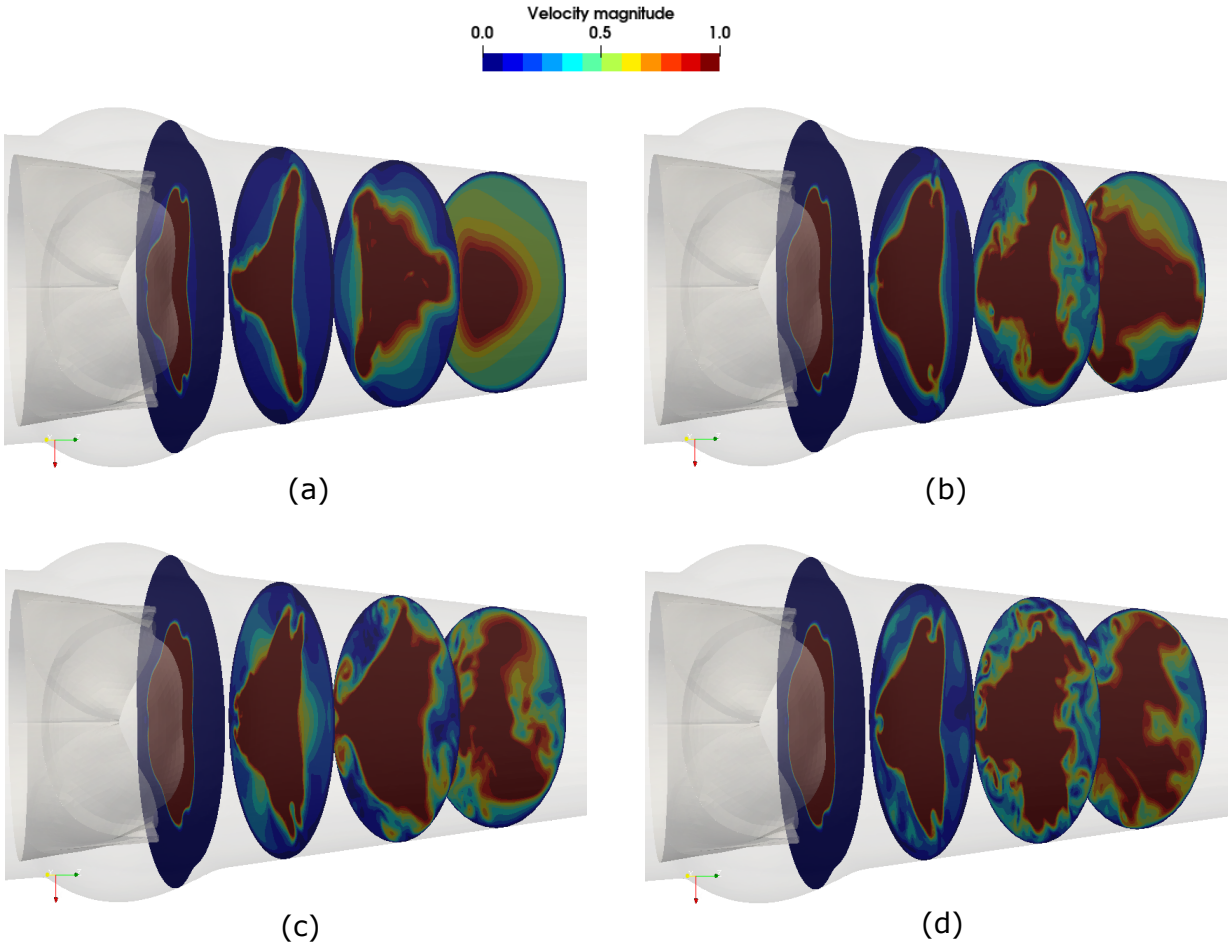

Figure 6.7: Contours of velocity magnitude at times (a) $t = 0.06s$, (b) $t = 0.08s$, (c) $t = 0.1s$, and $t = 0.12s$ on z-plane slices located respectively from left to right at $z/D = 0.1,\ 0.5,\ 1$, and 1.5 from the edge of the BHV in an open position.

(figure 6.8(e)), the positive pressure gradient causes a large portion of the flow near to the aortic wall to reverse direction, consequently, accelerating the closing of the valve (figure 6.8(f)). Therefore, the closing phase of the valve can be categorized into slow and rapid closure which happens during the decelerating and negative phases of the inflow waveform. The rapid closure of the valve creates a small sudden forward flow with circular vortex ring in the center of the aorta, which will be discussed more thoroughly in the next section.

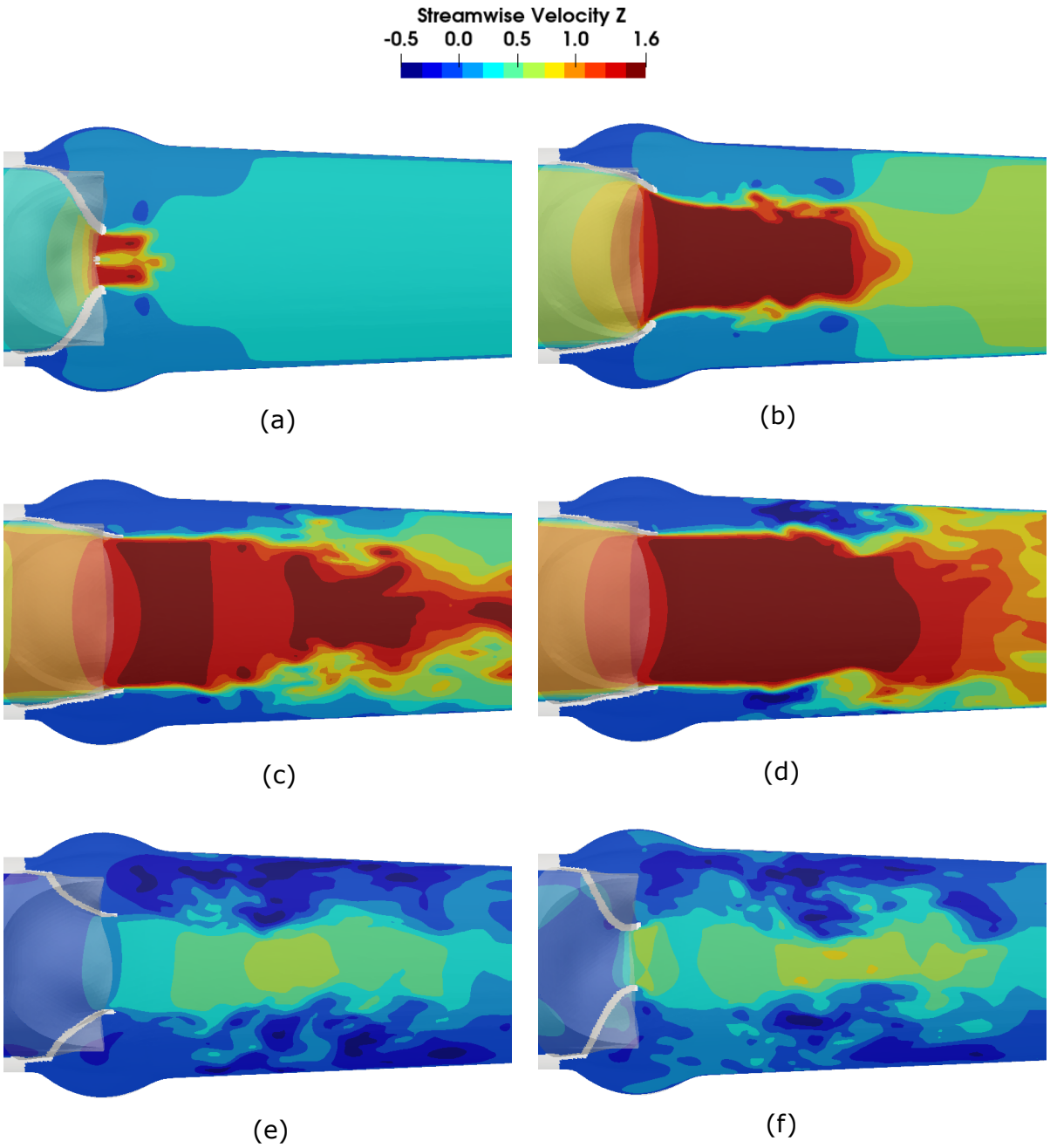

Figure 6.8: Contours of velocity component in axial direction (z) on y-plane at times (a) $t = 0.02s$, (b) $t = 0.05s$, (c) $t = 0.08s$, (d) $t = 0.12s$, (e) $t = 0.3s$, and (f) $t = 0.32$.

6.5 Vortex Dynamics

The contours of out-of-plane vorticity are illustrated in figure 6.9 on the y-midplane of the aorta for six time instants during the complete cycle. Figure 6.9(a) shows well-organized layers of vorticity created along the valve opening at early systole. Two vortex rings can be seen in this time step. The first one which is separated from the valve shear layer at an earlier time is due to the roll-up of the vorticity at the time when the valve was almost closed. As it was mentioned in §6.3 and shown in figure 6.4(a) during the FSI simulations, deformation of the leaflets starts from the belly region, as opposed to the dynamic simulations, where it starts from the free edges. This feature creates a vortex ring at the narrow opening of the valve. Once the free edges of the valve start to move, a larger and geometrically more complex vortex ring develops. Both of these vortex rings, which were also observed in the FSI simulations of Chen and Luo [10], are shown in figure 6.9(a). As the valve opens, both of the vortex rings and shear layer attached to the second ring propagate downstream and pass the sinus area (figure 6.9(b)).

During the mid-systole and by increasing the flow rate, the second vortex ring separates from the shear layer and triggers instabilities in the domain (figure 6.9(c)), after which the shear layer starts to shed that further destabilizes the vorticity field, causing the vortex rings to impinge on the aortic wall (figure 6.9(d)). The existence of the trailing jet behind the vortex rings is because of the high stroke ratio of $L/D = 5.23$ ($L = 0.135m$ is the stroke length of the cycle), which is higher than the formation number of 4 [109]. As the forward flow starts to decelerate, the leaflets initiate the slow closing phase. The displacement of the leaflets causes the shear layer to roll up and create a distinct vortex ring as shown in figure 6.9(e). This vortex ring detaches from the shear layer and due to the instabilities in the domain, break ups shortly afterwards. When the flow rate enters the backward flow phase, it causes a rapid movement of the leaflets. Consequently, the shear layer rolls up and creates the last vortex ring before the complete closure of the valve (figure 6.9(f)).

The 2D out-of-plane vorticity field cannot show the complexity of the vortex dynamics in these simulations; therefore, iso-surfaces of q-criterion [9] are illustrated in figure 6.10 to visualize the 3D vortical structures. Figure 6.10(a) shows the formation of the first vortex ring through the cen-

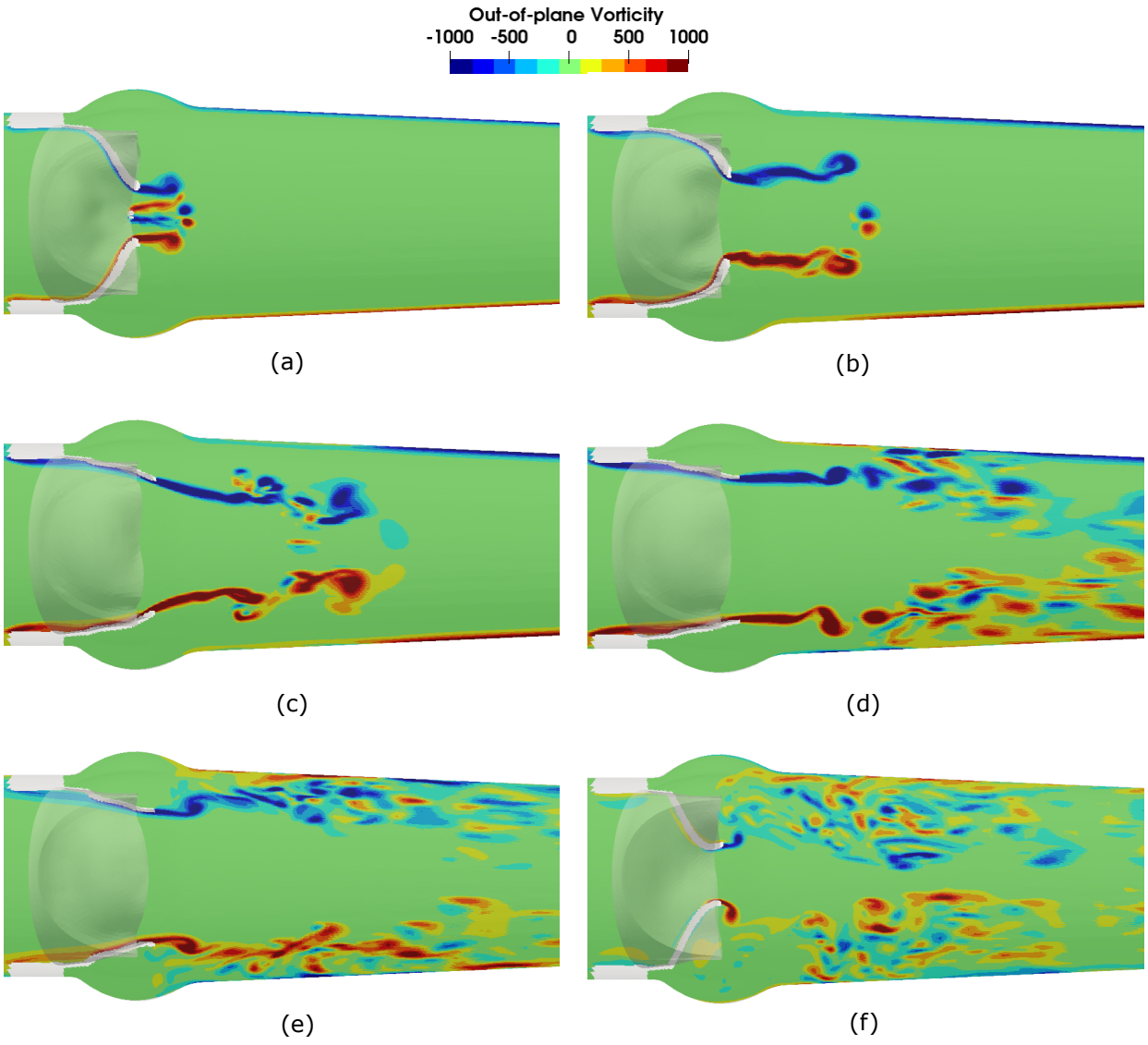

Figure 6.9: Contours of out-of-plane vorticity on y-plane at times (a) $t = 0.02s$, (b) $t = 0.04s$, (c) $t = 0.06s$, (d) $t = 0.08s$, (e) $t = 0.25s$, and (f) $t = 0.32s$.

tral opening. As free edges of the valve move a three-lobed vortex ring emerges, which is shaped according to the gap created between the leaflets (figure 6.10(b)). The newly generated stronger vortex ring causes the edges of the first circular vortex ring to bend back. As the vortex ring moves downstream, the three lobes move faster than the central part of the ring (figure 6.10(c)), similar to the vortex rings seen in pulsatile flows through inclined elliptic nozzles [199]. By separating the vortex ring from the shear layer (figure 6.10(d)), the central part catches up and even passes

it, making the three lobes stretch backward. Consequently, the vortex ring breaks up and further destabilizes the vorticity of the domain in addition to the shading effects of the shear layer. This causes the emergence of the small-scale worm-like turbulent structures that dominate the domain as seen in figure 6.10(e).

During the decelerating forward flow, as discussed earlier, the roll-up of the shear layer creates a distinct vortex ring. This relatively circular vortex ring is illustrated in figure 6.10(f). As we enter the backward flow phase, a weaker triangular vortex ring is created (figure 6.10(g)), which has the shape of the gap between the leaflets during the rapid closure (figure 6.6(b)). This vortex ring breaks up earlier than its predecessor and turns into turbulent-like structures similar to the rest of the domain (figure 6.10(h)).

In order to test the proposed scaling law for the propagation of vortex rings (see §4), the location of second vortex rings are plotted in figure 6.11(a) for previous [10] and present FSI simulations. The second vortex ring taken form FSI data of Chen and Luo [10] corresponds to a case with non-dimensional period of $T^*_{ave} = 12.33$ and Reynolds number of $Re_{ave} = 1264$, while for the present simulation, $T^*_{ave} = 5.24$ and $Re_{ave} = 880$. The scaled locations of the vortex rings are illustrated in figure 6.11(b). The scaling law collapses data with R-squared of 0.94, which is lower than the results of vortex rings generated from a circular cylinder in §4. While the accuracy of the scaling is still satisfactory, there are three main reasons contributing to the lower accuracy compared to results of §4. First, the waveform of these simulations (figure 6.2 for the present simulation) are different than the waveform used to calculate the current scaling (4.1(b)). Additionally, the cross-section of the inflow for FSI simulations are not circular and change with time. Finally, the second vortex rings are interacting with the first vortex ring from the beginning of their formation and undergo large deformations.

6.6 Shear Stress

The flow features discussed in previous sections can affect the mechanical forces exerted on the blood cells. One of the main sources of these loads originates from the instantaneous viscous stresses. Similar to §5.5 and in order to reduce the second-order viscous stress tensor, a coordinate-

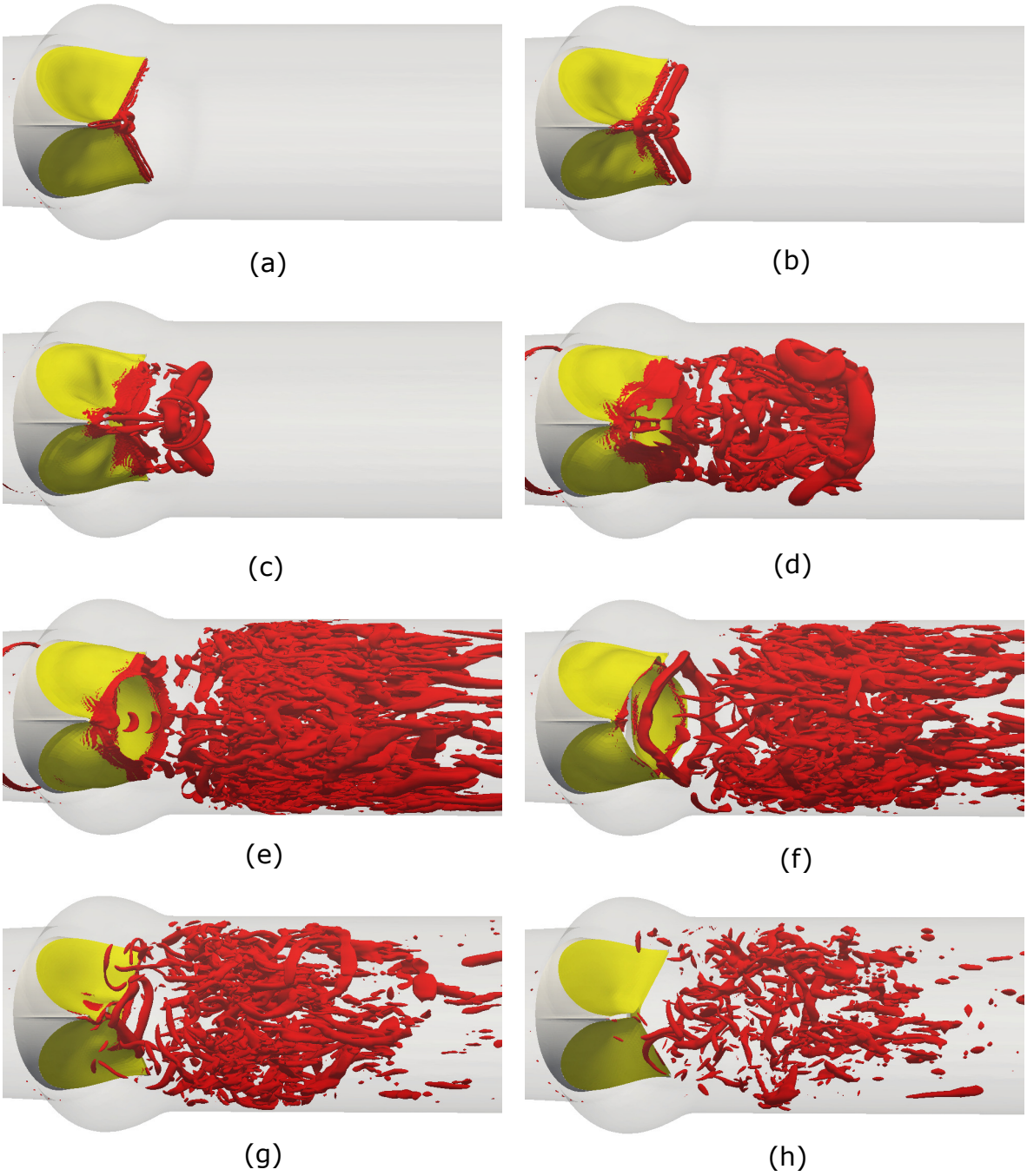

Figure 6.10: Vortical structures visualized by iso-surfaces of q-criterion at times (a) $t = 0.01s$, (b) $t = 0.02s$, (c) $t = 0.03s$, (d) $t = 0.06s$, (e) $t = 0.13s$, (f) $t = 0.25s$, (g) $t = 0.32s$, and (h) $t = 0.35s$.

independent scalar shear stress (equation 5.1) is used to show the instantaneous viscous stresses during the cycle. The contours of scalar shear stress are plotted on the y-plane at six different

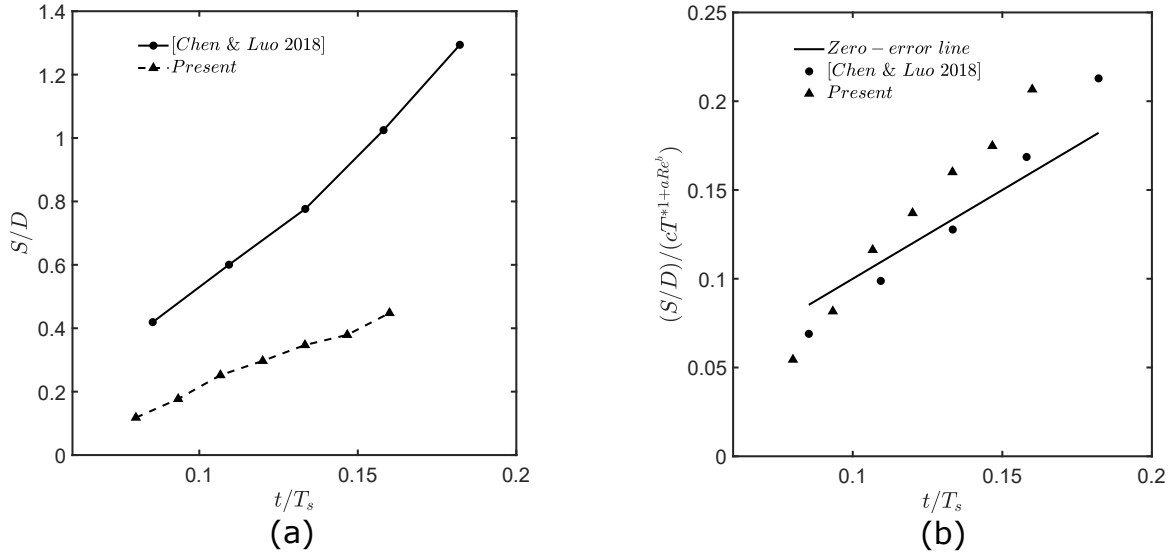

Figure 6.11: Location of the second vortex rings (a) before and (b) after scaling taken from previous [10] and present FSI simulations.

time instants during a cardiac cycle in figure 6.12. Comparing the viscous distributions in figure 6.12 with the out-of-plane vorticity in figure 6.9, illustrates that the regions with high vorticity, i.e., vortical structures and shear layer along with the aortic jet, have the highest shear stress magnitudes and hence exert higher mechanical loads on the blood cells. Additionally, Snapshots of scalar shear stress show an increasing trend in regions with high shear stress until the peak systole (figure 6.12(d)), which goes upstream with entering the diastole (figure 6.12(f)). Consequently, during the complete cardiac cycle, the sinus area does not experience values of high shear stress. This is an advantage of bio-prosthetic heart valves compared to the bi-leaflet mechanical counterparts, which was previously observed during the systole by Borazjani [48].

6.7 Platelet Activation

Similar to §5.6, two mathematical platelet activation models are used in an Eulerian framework in this section to analyze the shear-induced platelet activation for the FSI simulation of a BHV: linear level activation; and Soares model. Figure 6.13 shows the contours of platelet activation on y-plane for linear and Soares models at five time instants during a cardiac cycle on the first

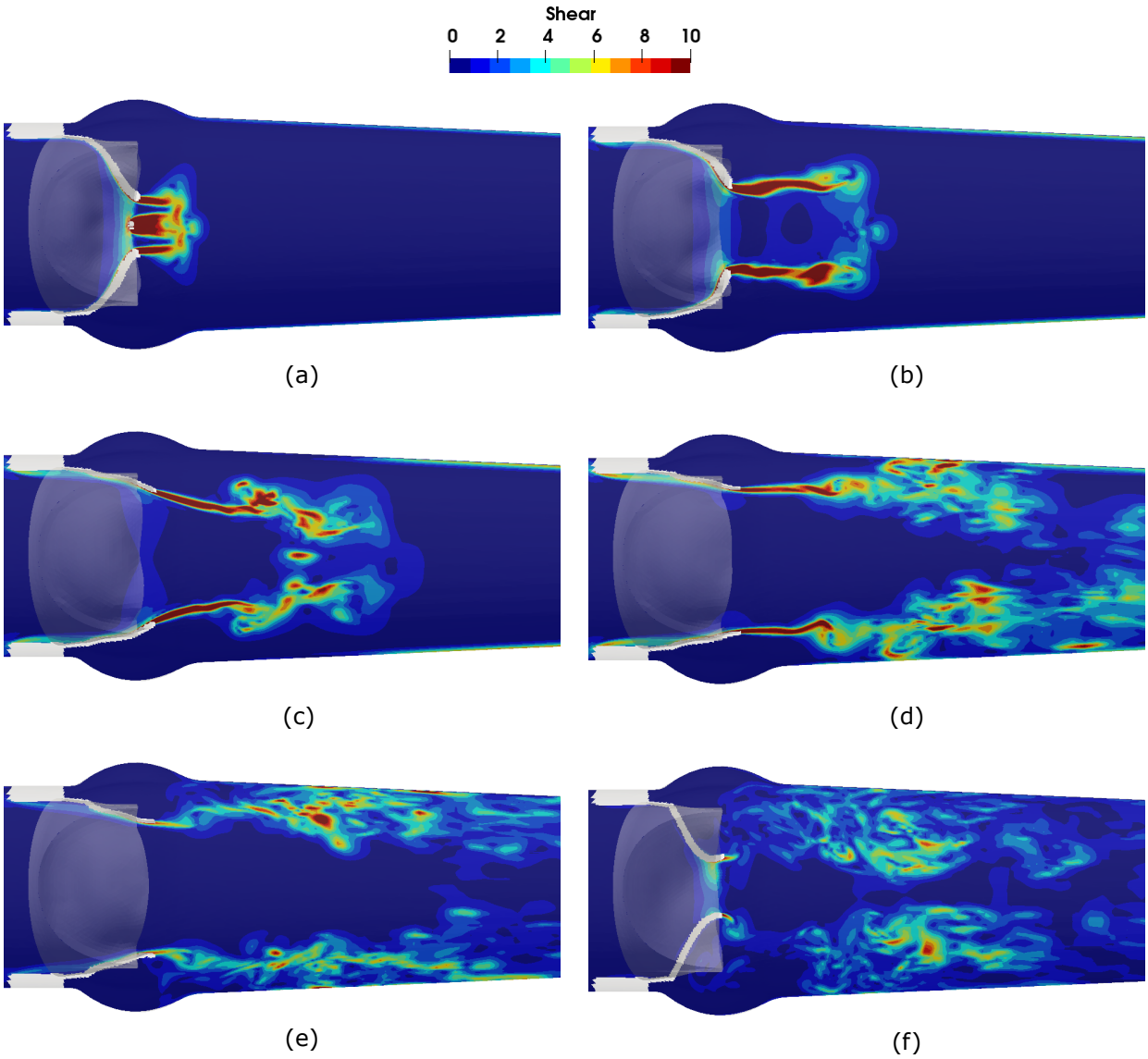

Figure 6.12: Contours of scalar shear stress on y-plane at times (a) $t = 0.02s$, (b) $t = 0.04s$, (c) $t = 0.06s$, (d) $t = 0.08s$, (e) $t = 0.25s$, and (f) $t = 0.32s$.

and second columns, respectively. It is clear that the linear model shows extremely high levels of activation during the diastole compared to systole. The main reason for these unrealistic results is that the model only considers the shear stress accumulation as a source term for the platelet activation generation; i.e., shear stress times the exposure time. Consequently, it does not account for highly dynamic stress conditions during a cardiac cycle [200, 201]. This is better illustrated in

figure 6.14 by calculating the integration of the platelet activation over the cycle for both models. The calculated activation levels are normalized by the total activation level at the end of the cycle for each model. It is clear that the activation level becomes constant after valve closure for the Soares model with a step during the closing phase, while for the linear model it continues to increase until the end of the cycle. As it is shown in figure 6.13(d,e), after the closure, the regions with high platelet activation move to the vicinity of the valve and sinus area due to the regurgitation, without further activation generation. However, for the linear model, the majority of the domain shows very high activation levels compared to diastole. This shows that while most of the platelets are activated during systole, they are convected to the valve and sinus area during the diastole.

6.8 Conclusion

In this chapter, the implemented thin shell FE framework incorporating a nonlinear anisotropic material model and the new contact handling method was coupled with CURVIB flow solver to perform the FSI simulation of a BHV for a complete cardiac cycle. Comparing the kinematics of BHV leaflets for the FSI and dynamic simulations shows significant differences in the deformation and hence strain distribution during the opening of the valve. For the FSI simulations, the deformation starts from the belly region and develops to the free edges, while for the dynamic simulations the free edges undergo deformation first. However, during the closing phase, the deformation of the leaflet for both FSI and dynamic simulations show similar behavior, which was shown to be due to a relatively uniform distribution of hydrodynamic pressure over the leaflets. The interesting difference during this phase was the opposite direction of the swirling motion of the leaflets during the rapid closure for the valves with asymmetric fiber orientation.

The visualizations of the vorticity and q-criterion showed the creation of two starting vortex rings. The first circular one is a consequence of latency of the deformation of the valve in response to the upcoming flow, while the stronger second three-lobed vortex ring was created due to the roll-up of the shear layer during the opening phase. During the mid systole, the velocity field showed a jet flipping phenomenon, which rapidly disappeared as the aortic jet becomes unstable. As we entered the declining phase of forward flow, the valve started to slowly close, which created

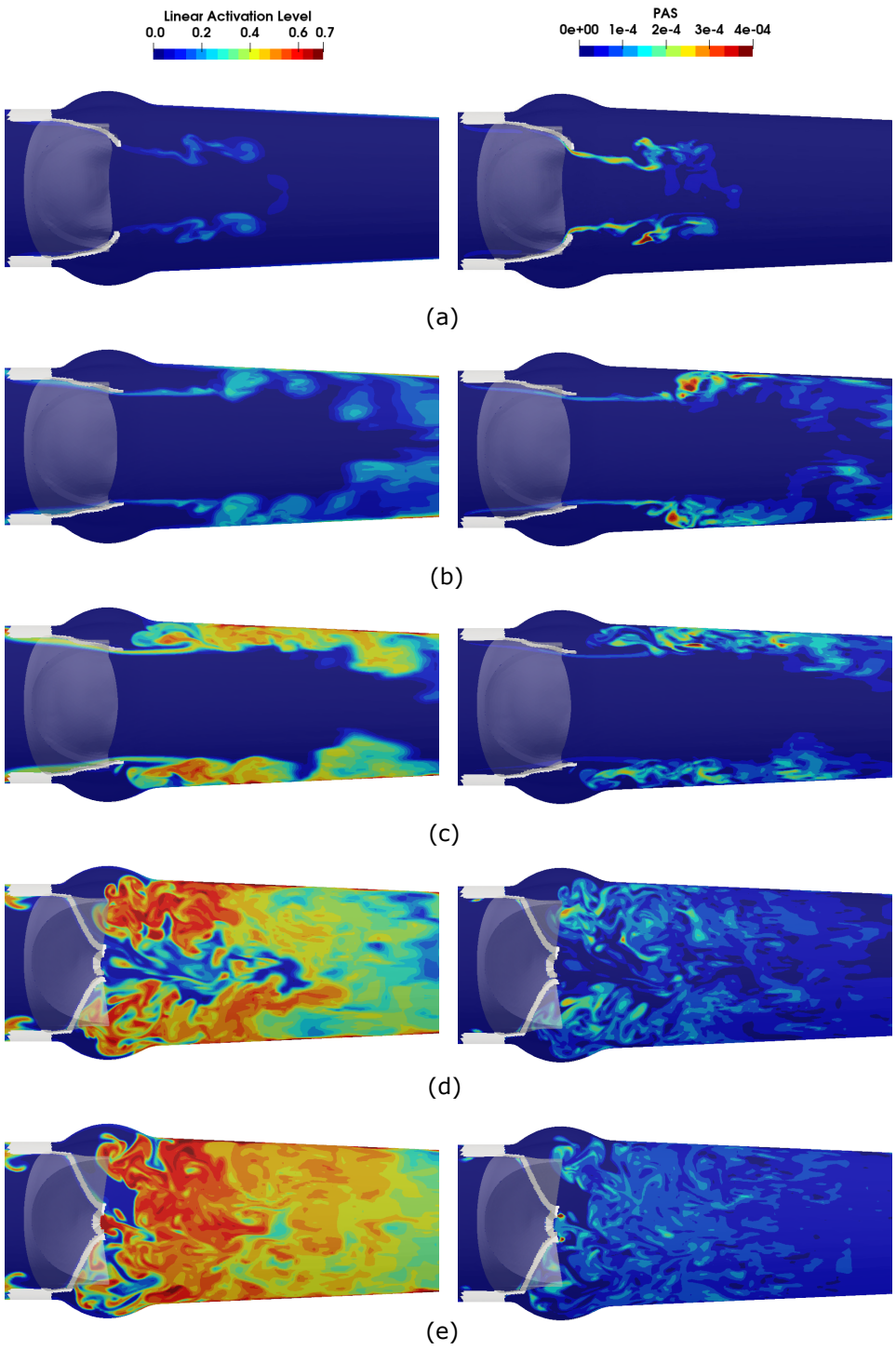

Figure 6.13: Contours of platelet activation for linear (column 1) and Soares model (column 2) on y-plane at times (a) $t = 0.05s$, (b) $t = 0.1s$, (c) $t = 0.22s$, (d) $t = 0.36s$, and (e) $t = 0.42s$.

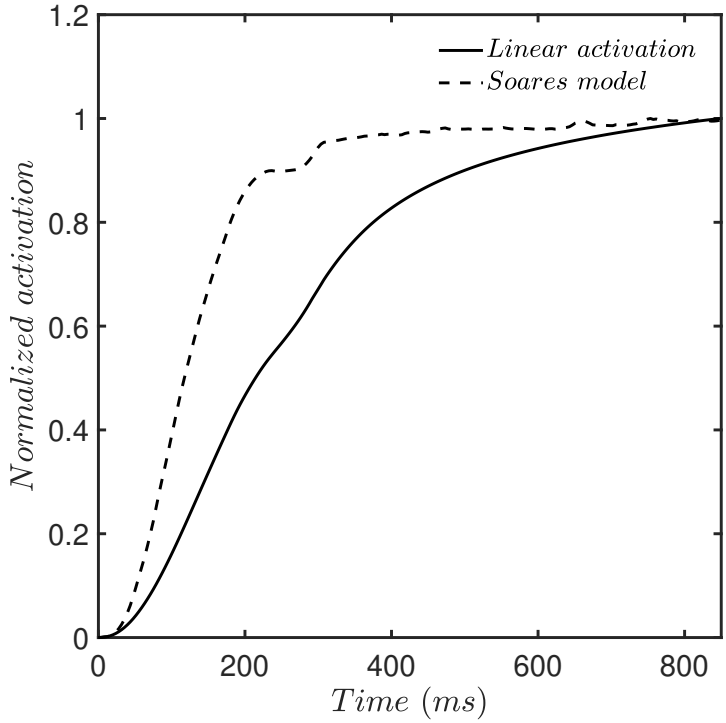

Figure 6.14: The integration of the platelet activation over the straight aorta during the cardiac cycle for linear and Soares models normalized by the end of the cycle activation level.

a circular vortex ring. The imposed backward flow caused a rapid closure, leading to the formation of a triangular vortex ring. These two vortex rings during the closing phase are illustrated for the first time to the knowledge of the author. The comparison of the scalar viscous shear stress with the vorticity field showed a correlation between regions with high vorticity and high shear stress. Additionally, the contours of platelet activation, showed more realistic results for the Soares compared to the linear platelet activation model. It showed that while most of the platelets are activated during the systole, the activated platelets are sucked back to the vicinity of the valves and remain there for most of the diastole.

7. SUMMARY AND OUTLOOK [1]

Cardiovascular diseases are the main cause of death in the US. One of the widespread types of cardiovascular disease is related to the malfunction of mitral or aortic heart valves, which in many cases require the valve to be replaced by an artificial valve. The artificial valves are far from perfect and impose non-physiological flow features different from the native heart valves, which can alter the vortical structures in the vicinity of the valve. This, in turn, can affect the hemodynamic forces acting on the blood cells that can cause thrombus generation and lead to strokes. The altered forces can also change the kinematics of the valves and possibly can lead to backward flow, increasing the heart workload. There are two main types of heart valves, i.e., bio-prosthetic heart valves (BHV) and bi-leaflet mechanical heart valves (BMHV). The BMHVs have rigid leaflets, while the BHVs leaflets are made of thin fabrics that undergo high deformations. Therefore, to study the vortex dynamics of BHVs, a finite element method (FEM) is needed to be coupled with the flow solver.

One of the dominant flow features of the artificial heart valves is the generation, propagation, and interaction of periodically generated vortex rings. Here, first, the propagation and vortex dynamics of periodic vortex rings are studied in a simplified setup. Then, the findings are discussed and contrasted for BMHV and BHV implants, separately. Additionally, the effects of vortex rings on the kinematics and thrombus generation of these heart valves are addressed.

First, the propagation of periodically-generated vortex rings (period T) is numerically investigated by imposing pulsed jets of velocity U_{jet} and duration T_s (no flow between pulses) at the inlet of a cylinder of diameter D exiting into a tank. Because of the step-like nature of pulsed jet waveforms, the average jet velocity during a cycle is $U_{ave} = U_{jet}T_s/T$. By using U_{ave} in the definition of Reynolds number ($Re = U_{ave}D/\nu$, ν: kinematic viscosity of fluid) and non-dimensional period ($T^* = TU_{ave}/D = T_sU_{jet}/D$, i.e., equivalent to formation time), based on the results, vortex ring velocity U_v/U_{jet} becomes approximately independent of the stroke ratio T_s/T. The results also

[1] Parts of this chapter have been published as "H. Asadi, H. Asgharzadeh, and I. Borazjani. "On the scaling of propagation of periodically generated vortex rings," *Journal of Fluid Mechanics*, vol. 853, pp. 150-170, 2018."

show that U_v/U_{jet} increases by reducing Re or increasing T^* (more sensitive to T^*) according to a power law of the form $U_v/U_{jet} = 0.27\ {T^*}^{1.31Re^{-0.2}}$. An empirical relation, therefore, for the location of vortex ring core centers (S) over time (t) is proposed ($S/D = 0.27\ {T^*}^{1+1.31Re^{-0.2}} t/T_s$), which collapses (scales) not only our results but also the results of experiments for non-periodic rings. This might be due to the fact that the quasi-steady vortex ring velocity was found to have a maximum of 15% difference with the initial (isolated) one. Visualizing the rings during the periodic state shows that at low $T^* \leq 2$ and high $Re \geq 1400$ here, the stopping vortices become unstable and form hairpin vortices around the leading ones. However, by increasing T^* or decreasing Re the stopping vortices remain circular. Furthermore, rings with short $T^* = 1$ show vortex pairing after about one period in the downstream, but higher $T^* \geq 2$ generates a train of vortices in the quasi-steady state.

Then, the propagation and vortex dynamics of BMHVs are studied in a realistic configuration. We have performed three-dimensional high-resolution numerical simulations of a BMHV implanted at different orientations in an anatomic left ventricle-aorta obtained from magnetic resonance imaging (MRI) of a volunteer. The thoroughly validated overset curvilinear-immersed boundary (overset-CURVIB) fluid-structure interaction (FSI) flow solver is used in which the aorta and left ventricle (LV) are discretized with boundary-conforming and non-conforming curvilinear grids, respectively. The motion of the LV wall is prescribed based on a lumped parameter model while the motion of the leaflets is calculated using a strong coupled FSI algorithm enhanced with the Aitken convergence technique. We carried out simulations for three valve orientations, which differ from each other by 45 deg, and compared the leaflet motion and flow field for multiple cycles. Our results show reproducible and relatively symmetrical opening for all valve orientations. The presence of small-scale vortical structures after peak systole causes significant cycle-to-cycle variations in valve kinematics during the closing phase for all valve orientations, which is observed in the variation of full closure time from $410ms$ to $640ms$ between two consecutive cycles for the 0 deg orientation. The proposed scaling for the propagation of vortex rings shows good agreement with the locations of core centers of the mitral vortex ring inside the LV. Furthermore, our results

show that valve orientation does not have a significant effect on the distribution of viscous shear stress in the ascending aorta. Additionally, two different mathematical activation models including the linear level of activation and Soares model are used to quantify the platelet activation in the ascending aorta. The results show that the valve orientation does not significantly affect (less than 8%) the total platelet activation in the ascending aorta.

Lastly, the vortex ring propagation and vortex dynamics of BHVs are studied. The simulation of the BHV has two main additional challenges. First, a finite element (FE) framework is required to simulate the motion of the thin deformable leaflets. Second, a robust physic-based contact handling is needed for the closing phase of the valves. A new general contact model is proposed for preventing inter-leaflet penetration of tissue heart valves at the end of the systole, which has the advantage of applying kinematic constraints directly and creating smooth leaflet free edges. At the end of each time step, the impenetrability constraints and momentum exchange between the impacting bodies are applied separately based on the coefficient of restitution. The contact method is implemented in a rotation-free, large deformation, thin shell FE framework based on Loop's subdivision surfaces. A non-linear, anisotropic material model for a BHV is employed which uses Fung-elastic constitutive laws for in-plane and bending responses, separately. The contact model is verified and validated against several benchmark problems. For a BHV-specific validation, the computed strains on different regions of a BHV under constant pressure are compared with experimentally measured data. Finally, dynamic simulations of BHV under physiological pressure waveform are performed for symmetrical and asymmetrical fiber orientations incorporating the new contact model and compared with the penalty contact method. The proposed contact model provides the coaptation area of a functioning BHV during the closing phase for both of the fiber orientations. Our results show that fiber orientation affects the dynamic of leaflets during the opening and closing phases. A swirling motion for the BHV with asymmetrical fiber orientation is observed, similar to experimental data. Finally, the validated and verified FE framework is coupled with the overset-CURVIB flow solver using a strong coupling FSI formulation augmented with under-relaxation and Aitken convergence accelerator. The coupled FSI FE-CURVIB is used

to validate the numerical results with the experimental results of an inverted flapping flag.

The dynamics of BHV leaflets for FSI and dynamic simulations have shown significant differences during the opening phase. The contours of hydrodynamic pressure on the leaflets during the opening show a non-uniform distribution, which caused the belly region to deform first and after reaching the maximum deflection in that region the free edges started to deflect. This is in direct contrast to the dynamic simulation of BHV. During the opening phase, two vortex rings were observed. The first one was more circular and was formed due to the latency of valve opening in response to the flow. The second has a three-lobed shape which constantly deformed during the propagation. Our proposed scaling law for the location of core centers of the vortex rings properly predicts the location of the three-lobed vortex ring (R-squared of 0.94). During the closing phase, the FSI and dynamic data show similar results due to the relatively uniform pressure distribution. The closure of the BHV showed two different stages; the slow closure, which began when the forward flow started to recede, and the rapid closure during the backward flow. These two stages triggered the creation of two vortex rings with circular and triangular shapes, respectively. Additionally, the swirling motion observed in dynamic simulations existed in FSI simulations, too but in a reversed direction. The time history of platelet activation illustrated that the majority of platelets are activated during the systole; however, activated platelets are convected back to the vicinity of the valve and remain there for most of the systole.

In conclusion, the vortex dynamics of the prosthetic heart valves show complicated features specifically during the late systole and diastole, when the small-scale vortical structures begin to emerge. Despite the differences in the flow features of BMHV and BHV, the proposed scaling law for the propagation of the vortex rings shows promising results for vortex rings generated in both aortic and mitral positions. The results show that the vortex rings in specific and vortical structures, in general, have significant effects on the valve kinematics, which can be due to the different geometrical and material properties. Therefore, this study and the implemented framework can be used as a platform for future patient-specific virtual surgery and a tool for optimizing the different features of prosthetic heart valves.

7.1 Future work

For future work, we plan to investigate the flow features of transcatheter heart valves in terms of vortex dynamics and platelet activation. The geometry of the leaflets of these valves resemble the BHV; however, they include stent frames, which create complex multiple contacting locations with other components. Therefore, the comparison of their vortical structures and thrombus generation could potentially open roads for further future advances. In addition, the left ventricle-aorta setup will be complemented with a valve, either BHV or MHV, in the mitral position and its effect on the vortex dynamics inside the ventricle will be assessed. These two plans are further discussed below:

A. Vortex dynamics of transcatheter heart valves

Due to the recent developments in transcatheter heart valves and their superiority for patients with high-risk surgery, they are among the popular topics in current research and development endeavors. The transcatheter heart valves include a stent frame that comes to contact with other components of the valve in many locations. The suggested efficient contact algorithm is expected to be a proper choice for numerical simulations of the transcatheter heart valves, where the contact is not limited to the free edges of the leaflets. The computed and compared shear stress distribution and platelet activation of the transcatheter and native heart valves can be used as a good measure to improve their performance. This could be extended to evaluation and optimization of the implantation process and the orientation of the valves, similar to the study in §5.

B. Vortex dynamics of left heart

As discussed in §5, the mitral valve was not included as the main focus of that study was the vortex dynamics and thrombus generation of the aortic valves. By including a BHV or MHV in mitral position along with one in the aortic positions the left heart simulations will be performed. These simulations can be used to investigate the combined effects of valves in vortex dynamics both in the left ventricle and ascending aorta. In particular, the propagation and interaction of the mitral vortex ring with the aortic backward jet is an interesting topic. Furthermore, the effects of

the mitral valve on the platelet activation in different implantation can be studied in the LV.

REFERENCES

[1] D. R. Webster and E. K. Longmire, "Vortex rings from cylinders with inclined exits," *Physics of Fluids*, vol. 10, pp. 400–416, 1998.

[2] J. Valdés and E. Oñate, "Orthotropic rotation-free basic thin shell triangle," *Computational Mechanics*, vol. 44, no. 3, pp. 363–375, 2009.

[3] R. Frisch-Fay, *Flexible bars*. Butterworths, 1962.

[4] K. Sze, X. Liu, and S. Lo, "Popular benchmark problems for geometric nonlinear analysis of shells," *Finite elements in analysis and design*, vol. 40, no. 11, pp. 1551–1569, 2004.

[5] J. Simo, M. Rifai, and D. Fox, "On a stress resultant geometrically exact shell model. part iv: Variable thickness shells with through-the-thickness stretching," *Computer methods in applied mechanics and engineering*, vol. 81, no. 1, pp. 91–126, 1990.

[6] H. Kim, J. Lu, M. S. Sacks, and K. B. Chandran, "Dynamic simulation of bioprosthetic heart valves using a stress resultant shell model," *Annals of biomedical engineering*, vol. 36, no. 2, pp. 262–275, 2008.

[7] D. Shier, J. Butler, and R. Lewis, *Hole's essentials of human anatomy & physiology*. McGraw-Hill Education New York, 2015.

[8] D. Kim, J. Cossé, C. H. Cerdeira, and M. Gharib, "Flapping dynamics of an inverted flag," *Journal of Fluid Mechanics*, vol. 736, 2013.

[9] H. JCR, A. Wray, and P. Moin, "Eddies, stream, and convergence zones in turbulent flows," *Studying Turbulence Using Numerical Simulation Databases-I1*, vol. 193, 1988.

[10] Y. Chen and H. Luo, "A computational study of the three-dimensional fluid–structure interaction of aortic valve," *Journal of Fluids and Structures*, vol. 80, pp. 332–349, 2018.

[11] S. Mendis, P. Puska, B. Norrving, W. H. Organization, *et al.*, *Global atlas on cardiovascular disease prevention and control*. Geneva: World Health Organization, 2011.

[12] E. J. Benjamin, M. J. Blaha, S. E. Chiuve, M. Cushman, S. R. Das, R. Deo, J. Floyd, M. Fornage, C. Gillespie, C. Isasi, *et al.*, "Heart disease and stroke statistics-2017 update: a report from the american heart association.," *Circulation*, vol. 135, no. 10, pp. e146–e603, 2017.

[13] P. M. Arvidsson, S. J. Kovács, J. Töger, R. Borgquist, E. Heiberg, M. Carlsson, and H. Arheden, "Vortex ring behavior provides the epigenetic blueprint for the human heart," *Scientific reports*, vol. 6, p. 22021, 2016.

[14] M. Gharib, E. Rambod, A. Kheradvar, D. J. Sahn, and J. O. Dabiri, "Optimal vortex formation as an index of cardiac health," *Proceedings of the National Academy of Sciences*, vol. 103, no. 16, pp. 6305–6308, 2006.

[15] W. G. Members, D. Lloyd-Jones, R. J. Adams, T. M. Brown, M. Carnethon, S. Dai, G. De Simone, T. B. Ferguson, E. Ford, K. Furie, *et al.*, "Executive summary: heart disease and stroke statistics—2010 update: a report from the american heart association," *Circulation*, vol. 121, no. 7, pp. 948–954, 2010.

[16] B. H. Jun, N. Saikrishnan, and A. P. Yoganathan, "Micro particle image velocimetry measurements of steady diastolic leakage flow in the hinge of a st. jude medical® regent™ mechanical heart valve," *Annals of biomedical engineering*, vol. 42, no. 3, pp. 526–540, 2014.

[17] D. Hasler, A. Landolt, and D. Obrist, "Tomographic piv behind a prosthetic heart valve," *Experiments in Fluids*, vol. 57, no. 5, p. 80, 2016.

[18] A. Aggarwal, A. M. Pouch, E. Lai, J. Lesicko, P. A. Yushkevich, J. H. Gorman III, R. C. Gorman, and M. S. Sacks, "In-vivo heterogeneous functional and residual strains in human aortic valve leaflets," *Journal of biomechanics*, vol. 49, no. 12, pp. 2481–2490, 2016.

[19] H. Hatoum and L. P. Dasi, "Reduction of pressure gradient and turbulence using vortex generators in prosthetic heart valves," *Annals of biomedical engineering*, vol. 47, no. 1, pp. 85–96, 2019.

[20] L. Ge, L. P. Dasi, F. Sotiropoulos, and A. P. Yoganathan, "Characterization of hemodynamic forces induced by mechanical heart valves: Reynolds vs. viscous stresses," *Annals of biomedical engineering*, vol. 36, no. 2, pp. 276–297, 2008.

[21] F. Sotiropoulos and I. Borazjani, "A review of state-of-the-art numerical methods for simulating flow through mechanical heart valves," *Medical & biological engineering & computing*, vol. 47, no. 3, pp. 245–256, 2009.

[22] R. Zakerzadeh, M.-C. Hsu, and M. S. Sacks, "Computational methods for the aortic heart valve and its replacements," *Expert review of medical devices*, vol. 14, no. 11, pp. 849–866, 2017.

[23] H. Stolarski, A. Gilmanov, and F. Sotiropoulos, "Nonlinear rotation-free three-node shell finite element formulation," *International journal for numerical methods in engineering*, vol. 95, no. 9, pp. 740–770, 2013.

[24] D. Kamensky, M.-C. Hsu, D. Schillinger, J. A. Evans, A. Aggarwal, Y. Bazilevs, M. S. Sacks, and T. J. Hughes, "An immersogeometric variational framework for fluid–structure interaction: Application to bioprosthetic heart valves," *Computer methods in applied mechanics and engineering*, vol. 284, pp. 1005–1053, 2015.

[25] C. Martin, W. Sun, and J. Elefteriades, "Patient-specific finite element analysis of ascending aorta aneurysms," *American Journal of Physiology-Heart and Circulatory Physiology*, vol. 308, no. 10, pp. H1306–H1316, 2015.

[26] D. A. Steinman, J. S. Milner, C. J. Norley, S. P. Lownie, and D. W. Holdsworth, "Image-based computational simulation of flow dynamics in a giant intracranial aneurysm," *American Journal of Neuroradiology*, vol. 24, no. 4, pp. 559–566, 2003.

[27] C. S. Peskin, "Numerical analysis of blood flow in the heart," *Journal of computational physics*, vol. 25, no. 3, pp. 220–252, 1977.

[28] F. Duarte, R. Gormaz, and S. Natesan, "Arbitrary lagrangian–eulerian method for navier–stokes equations with moving boundaries," *Computer Methods in Applied Mechanics and Engineering*, vol. 193, no. 45-47, pp. 4819–4836, 2004.

[29] M. Sahin and K. Mohseni, "An arbitrary lagrangian–eulerian formulation for the numerical simulation of flow patterns generated by the hydromedusa aequorea victoria," *Journal of Computational Physics*, vol. 228, no. 12, pp. 4588–4605, 2009.

[30] N. Filipovic, S. Mijailovic, A. Tsuda, and M. Kojic, "An implicit algorithm within the arbitrary lagrangian–eulerian formulation for solving incompressible fluid flow with large boundary motions," *Computer methods in applied mechanics and engineering*, vol. 195, no. 44-47, pp. 6347–6361, 2006.

[31] R. Cheng, Y. G. Lai, and K. B. Chandran, "Two-dimensional fluid-structure interaction simulation of bileaflet mechanical heart valve flow dynamics.," *The Journal of heart valve disease*, vol. 12, no. 6, pp. 772–780, 2003.

[32] F. Alauzet, A. Loseille, and G. Olivier, "Time-accurate multi-scale anisotropic mesh adaptation for unsteady flows in cfd," *Journal of Computational Physics*, vol. 373, pp. 28–63, 2018.

[33] R. Cheng, Y. G. Lai, and K. B. Chandran, "Three-dimensional fluid-structure interaction simulation of bileaflet mechanical heart valve flow dynamics," *Annals of biomedical engineering*, vol. 32, no. 11, pp. 1471–1483, 2004.

[34] D. M. Ingram, D. M. Causon, and C. G. Mingham, "Developments in cartesian cut cell methods," *Mathematics and Computers in Simulation*, vol. 61, no. 3-6, pp. 561–572, 2003.

[35] R. Glowinski, T.-W. Pan, T. I. Hesla, D. D. Joseph, and J. Periaux, "A fictitious domain approach to the direct numerical simulation of incompressible viscous flow past moving rigid bodies: application to particulate flow," *Journal of computational physics*, vol. 169, no. 2, pp. 363–426, 2001.

[36] F. P. Baaijens, "A fictitious domain/mortar element method for fluid–structure interaction," *International Journal for Numerical Methods in Fluids*, vol. 35, no. 7, pp. 743–761, 2001.

[37] M.-C. Lai and C. S. Peskin, "An immersed boundary method with formal second-order accuracy and reduced numerical viscosity," *Journal of computational Physics*, vol. 160, no. 2, pp. 705–719, 2000.

[38] W. Kim, I. Lee, and H. Choi, "A weak-coupling immersed boundary method for fluid–structure interaction with low density ratio of solid to fluid," *Journal of Computational Physics*, vol. 359, pp. 296–311, 2018.

[39] R. Mittal and G. Iaccarino, "Immersed boundary methods," *Annu. Rev. Fluid Mech.*, vol. 37, pp. 239–261, 2005.

[40] C. S. Peskin, "The immersed boundary method," *Acta numerica*, vol. 11, pp. 479–517, 2002.

[41] B. E. Griffith, R. D. Hornung, D. M. McQueen, and C. S. Peskin, "An adaptive, formally second order accurate version of the immersed boundary method," *Journal of computational physics*, vol. 223, no. 1, pp. 10–49, 2007.

[42] A. Gilmanov and F. Sotiropoulos, "A hybrid cartesian/immersed boundary method for simulating flows with 3d, geometrically complex, moving bodies," *Journal of computational physics*, vol. 207, no. 2, pp. 457–492, 2005.

[43] C. S. Peskin, "Flow patterns around heart valves: a numerical method," *Journal of computational physics*, vol. 10, no. 2, pp. 252–271, 1972.

[44] R. Mittal, H. Dong, M. Bozkurttas, F. Najjar, A. Vargas, and A. Von Loebbecke, "A versatile sharp interface immersed boundary method for incompressible flows with complex boundaries," *Journal of computational physics*, vol. 227, no. 10, pp. 4825–4852, 2008.

[45] L. Ge and F. Sotiropoulos, "A numerical method for solving the 3d unsteady incompressible navier–stokes equations in curvilinear domains with complex immersed boundaries," *Journal of computational physics*, vol. 225, no. 2, pp. 1782–1809, 2007.

[46] I. Borazjani, L. Ge, and F. Sotiropoulos, "Curvilinear immersed boundary method for simulating fluid structure interaction with complex 3d rigid bodies," *Journal of Computational physics*, vol. 227, no. 16, pp. 7587–7620, 2008.

[47] I. Borazjani, L. Ge, T. Le, and F. Sotiropoulos, "A parallel overset-curvilinear-immersed boundary framework for simulating complex 3d incompressible flows," *Computers and Fluids*, vol. 77, pp. 76–96, 2013.

[48] I. Borazjani, "Fluid-structure interaction, immersed boundary-finite element method simulations of bio-prosthetic heart valves," *Computer Methods in Applied Mechanics and Engineering*, vol. 257, no. 0, pp. 103–116, 2013.

[49] B. Iung and A. Vahanian, "Epidemiology of valvular heart disease in the adult," *Nature Reviews Cardiology*, vol. 8, no. 3, pp. 162–172, 2011.

[50] R. A. Nishimura, C. M. Otto, R. O. Bonow, B. A. Carabello, J. P. Erwin, R. A. Guyton, P. T. O'Gara, C. E. Ruiz, N. J. Skubas, P. Sorajja, *et al.*, "2014 aha/acc guideline for the management of patients with valvular heart disease: a report of the american college of cardiology/american heart association task force on practice guidelines," *Journal of the American College of Cardiology*, vol. 63, no. 22, pp. e57–e185, 2014.

[51] J. C. Sun, M. J. Davidson, A. Lamy, and J. W. Eikelboom, "Antithrombotic management of patients with prosthetic heart valves: current evidence and future trends," *The Lancet*, vol. 374, no. 9689, pp. 565–576, 2009.

[52] G. D. Dangas, J. I. Weitz, G. Giustino, R. Makkar, and R. Mehran, "Prosthetic heart valve thrombosis," *Journal of the American College of Cardiology*, vol. 68, no. 24, pp. 2670–2689, 2016.

[53] R. M. Suri and H. V. Schaff, "Selection of aortic valve prostheses: contemporary reappraisal of mechanical versus biologic valve substitutes," *Circulation*, vol. 128, no. 12, pp. 1372–1380, 2013.

[54] P. Bloomfield, "Choice of heart valve prosthesis," *Heart*, vol. 87, no. 6, pp. 583–589, 2002.

[55] T. Carrel, W. P. Dembitsky, B. de Mol, D. Obrist, G. Dreyfus, B. Meuris, B. Vennemann, D. Lapeyre, and H. Schaff, "Non-physiologic closing of bi-leaflet mechanical heart prostheses requires a new tri-leaflet valve design," *International journal of cardiology*, vol. 304, pp. 125–127, 2020.

[56] S. J. Head, M. Çelik, and A. P. Kappetein, "Mechanical versus bioprosthetic aortic valve replacement," *European heart journal*, vol. 38, no. 28, pp. 2183–2191, 2017.

[57] T. Maxworthy, "The structure and stability of vortex rings," *Journal of Fluid Mechanics*, vol. 51, no. 1, pp. 15–32, 1972.

[58] K. Mohseni, "A formulation for calculating the translational velocity of a vortex ring or pair," *Bioinspiration & biomimetics*, vol. 1, no. 4, p. S57, 2006.

[59] L. Gan and T. Nickels, "An experimental study of turbulent vortex rings during their early development," *Journal of Fluid Mechanics*, vol. 649, pp. 467–496, 2010.

[60] H. Asgharzadeh and I. Borazjani, "Effects of reynolds and womersley numbers on the hemodynamics of intracranial aneurysms," *Computational and Mathematical Methods in Medicine 7412926*, vol. 2016, 2016.

[61] I. Borazjani, L. Ge, and F. Sotiropoulos, "High-resolution fluid–structure interaction simulations of flow through a bi-leaflet mechanical heart valve in an anatomic aorta," *Annals of biomedical engineering*, vol. 38, no. 2, pp. 326–344, 2010.

[62] S. S. Abbas, M. S. Nasif, R. Al-Waked, and M. A. Meor Said, "Numerical investigation on the effect of bileaflet mechanical heart valve's implantation tilting angle and aortic root geometry on intermittent regurgitation and platelet activation," *Artificial organs*, vol. 44, no. 2, pp. E20–E39, 2020.

[63] I. Borazjani and F. Sotiropoulos, "The effect of implantation orientation of a bileaflet mechanical heart valve on kinematics and hemodynamics in an anatomic aorta," *Journal of biomechanical engineering*, vol. 132, no. 11, 2010.

[64] A. M. Calafiore, M. Mauro, S. Gallina, I. Yassin, Y. Shaheen, C. Canosa, A. Iaco, and V. Mazzei, "Surgical treatment of mitral valve regurgitation in dilated cardiomyopathy," in *Heart Surg Forum*, vol. 7, pp. 21–5, "G. D'Annunzio" University, 2004.

[65] I. Huněk, "On a penalty formulation for contact-impact problems," *Computers & structures*, vol. 48, no. 2, pp. 193–203, 1993.

[66] P. E. Hammer, M. S. Sacks, J. Pedro, and R. D. Howe, "Mass-spring model for simulation of heart valve tissue mechanical behavior," *Annals of biomedical engineering*, vol. 39, no. 6, pp. 1668–1679, 2011.

[67] J. Kiendl, M.-C. Hsu, M. C. Wu, and A. Reali, "Isogeometric kirchhoff–love shell formulations for general hyperelastic materials," *Computer Methods in Applied Mechanics and Engineering*, vol. 291, pp. 280–303, 2015.

[68] H. Asgharzadeh and I. Borazjani, "A newton–krylov method with an approximate analytical jacobian for implicit solution of navier–stokes equations on staggered overset-curvilinear grids with immersed boundaries," *Journal of computational physics*, vol. 331, pp. 227–256, 2017.

[69] F. Cirak, M. Ortiz, and P. Schröder, "Subdivision surfaces: a new paradigm for thin-shell finite-element analysis," *International Journal for Numerical Methods in Engineering*, vol. 47, no. 12, pp. 2039–2072, 2000.

[70] P. M. Naghdi, "The theory of shells and plates," in *Linear Theories of Elasticity and Thermoelasticity*, pp. 425–640, Springer, 1973.

[71] C. W. Macosko and R. G. Larson, *Rheology: principles, measurements, and applications*. Vch New York, 1994.

[72] R. Vetter, N. Stoop, T. Jenni, F. K. Wittel, and H. J. Herrmann, "Subdivision shell elements with anisotropic growth," *International journal for numerical methods in engineering*, vol. 95, no. 9, pp. 791–810, 2013.

[73] N. M. Newmark, "A method of computation for structural dynamics," *Journal of the engineering mechanics division*, vol. 85, no. 3, pp. 67–94, 1959.

[74] D. A. Knoll and D. E. Keyes, "Jacobian-free newton–krylov methods: a survey of approaches and applications," *Journal of Computational Physics*, vol. 193, no. 2, pp. 357–397, 2004.

[75] F. Cirak and M. Ortiz, "Fully c1-conforming subdivision elements for finite deformation thin-shell analysis," *International Journal for Numerical Methods in Engineering*, vol. 51, no. 7, pp. 813–833, 2001.

[76] F. Cirak and Q. Long, "Subdivision shells with exact boundary control and non-manifold geometry," *International Journal for Numerical Methods in Engineering*, vol. 88, no. 9, pp. 897–923, 2011.

[77] S. Green and G. Turkiyyah, "Second-order accurate constraint formulation for subdivision finite element simulation of thin shells," *International Journal for Numerical Methods in Engineering*, vol. 61, no. 3, pp. 380–405, 2004.

[78] I. Borazjani, "Fluid–structure interaction, immersed boundary-finite element method simulations of bio-prosthetic heart valves," *Computer Methods in Applied Mechanics and Engineering*, vol. 257, pp. 103–116, 2013.

[79] F. Cirak and M. West, "Decomposition contact response (dcr) for explicit finite element dynamics," *International Journal for Numerical Methods in Engineering*, vol. 64, no. 8, pp. 1078–1110, 2005.

[80] I. Borazjani, L. Ge, T. Le, and F. Sotiropoulos, "A parallel overset-curvilinear-immersed boundary framework for simulating complex 3d incompressible flows," *Computers & fluids*, vol. 77, pp. 76–96, 2013.

[81] Z. Song and I. Borazjani, "The role of shape and heart rate on the performance of the left ventricle," *Journal of biomechanical engineering*, vol. 137, no. 11, 2015.

[82] P. Davidson, *Turbulence: an introduction for scientists and engineers*. Oxford University Press, USA, 2015.

[83] R. R. Taveira, J. S. Diogo, D. C. Lopes, and C. B. da Silva, "Lagrangian statistics across the turbulent-nonturbulent interface in a turbulent plane jet," *Physical Review E*, vol. 88, no. 4, p. 043001, 2013.

[84] J. M. Burgers, "A mathematical model illustrating the theory of turbulence," *Advances in applied mechanics*, vol. 1, pp. 171–199, 1948.

[85] R. Jahanbakhshi, N. S. Vaghefi, and C. K. Madnia, "Baroclinic vorticity generation near the turbulent/non-turbulent interface in a compressible shear layer," *Physics of Fluids*, vol. 27, p. 105105, 2015.

[86] I. Sullivan, J. J. Niemela, R. E. Hershberger, D. Bolster, and R. J. Donnelly, "Dynamics of thin vortex rings," *J. Fluid Mech.*, vol. 609, pp. 319–347, 2008.

[87] D. J. Inman, *Engineering vibration*, vol. 3.

[88] D. Kamensky, F. Xu, C.-H. Lee, J. Yan, Y. Bazilevs, and M.-C. Hsu, "A contact formulation based on a volumetric potential: Application to isogeometric simulations of atrioventricular valves," *Computer methods in applied mechanics and engineering*, vol. 330, pp. 522–546, 2018.

[89] W. Sun, A. Abad, and M. S. Sacks, "Simulated bioprosthetic heart valve deformation under quasi-static loading," *Journal of Biomechanical Engineering*, vol. 127, pp. 905–914, 2005.

[90] P. E. Hammer, *Simulating heart valve mechanical behavior for planning surgical repair*. PhD thesis, Tufts University, Medford, MA, 2011.

[91] J. H. Lee, A. D. Rygg, E. M. Kolahdouz, S. Rossi, S. M. Retta, N. Duraiswamy, L. N. Scotten, B. A. Craven, and B. E. Griffith, "Fluid–structure interaction models of bioprosthetic heart valve dynamics in an experimental pulse duplicator," *Annals of biomedical engineering*, vol. 48, no. 5, pp. 1475–1490, 2020.

[92] A. Gilmanov, H. Stolarski, and F. Sotiropoulos, "Non-linear rotation-free shell finite-element models for aortic heart valves," *Journal of biomechanics*, vol. 50, pp. 56–62, 2017.

[93] C. Martin and W. Sun, "Comparison of transcatheter aortic valve and surgical bioprosthetic valve durability: a fatigue simulation study," *Journal of biomechanics*, vol. 48, no. 12, pp. 3026–3034, 2015.

[94] K. Pethig, A. Milz, C. Hagl, W. Harringer, and A. Haverich, "Aortic valve reimplantation in ascending aortic aneurysm: risk factors for early valve failure," *The Annals of thoracic surgery*, vol. 73, no. 1, pp. 29–33, 2002.

[95] M. Germano, U. Piomelli, P. Moin, and W. H. Cabot, "A dynamic subgrid-scale eddy viscosity model," *Physics of Fluids A: Fluid Dynamics*, vol. 3, no. 7, pp. 1760–1765, 1991.

[96] M. Wang and P. Moin, "Dynamic wall modeling for large-eddy simulation of complex turbulent flows," *Physics of Fluids*, vol. 14, no. 7, pp. 2043–2051, 2002.

[97] S. Kang, I. Borazjani, J. A. Colby, and F. Sotiropoulos, "Numerical simulation of 3d flow past a real-life marine hydrokinetic turbine," *Advances in water resources*, vol. 39, pp. 33–43, 2012.

[98] S. Kang, X. Yang, and F. Sotiropoulos, "On the onset of wake meandering for an axial flow turbine in a turbulent open channel flow," *Journal of Fluid Mechanics*, vol. 744, pp. 376–403, 2014.

[99] S. Colin and J. Costello, "Morphology, swimming performance and propulsive mode of six co-occuring hydromedusae," *The Journal of Experimental Biology*, vol. 205, pp. 427–437, 2002.

[100] J. Dabiri, S. Colin, J. Costello, and M. Gharib, "Flow patterns generated by oblate medusan jellyfish: field measurements and laboratory analysis," *The Journal of Experimental Biology*, vol. 208, pp. 1257–1265, 2005.

[101] M. Krieg and K. Mohseni, "Pressure and work analysis of unsteady, deformable, axisymmetric, jet producing cavity bodies," *J. Fluid Mech.*, vol. 769, pp. 337–368, 2015.

[102] I. Borazjani and M. Daghooghi, "The fish tail motion forms an attached leading edge vortex," *Proceedings of the Royal Society B: Biological Sciences*, vol. 280, no. 1756, p. 20122071, 2013.

[103] U. E. Ogunka, M. Daghooghi, A. M. Akbarzadeh, and I. Borazjani, "The ground effect in anguilliform swimming," *Biomimetics*, vol. 5, no. 1, p. 9, 2020.

[104] U. E. Ogunka, A. Akbarzadeh, and I. Borazjani, "Flow control with traveling-wave surface morphing at post-stall angles of attack," in *AIAA SCITECH 2022 Forum*, p. 1948, 2022.

[105] A.-V. Salsac, S. R. Sparks, J.-M. Chomaz, and J. C. Lasheras, "Evolution of the wall sheear stresses during the progressive enlargments of symmetric abdominal aortic aneurysms," *J. Fluid Mech.*, vol. 560, pp. 19–51, 2006.

[106] A. Kheradvar, H. Houle, G. Pedrizzetti, G. Tonti, T. Belcik, M. Ashraf, J. Lindner, M. Gharib, and D. Sahn, "Echocardiographic particle image velocimetry: a novel technique for quantification of left ventricle blood vorticity pattern," *Journal of American Society of Echocardiography*, vol. 23, pp. 86–94, 2010.

[107] S. S. Gopalakrishnan, B. Pier, and A. Biesheuvel, "Dynamics of pulsatile flow through model abdominal aorotic aneurysms," *J. Fluid Mech.*, vol. 758, pp. 150–179, 2014.

[108] A. Glezer, "The formation of vortex rings," *The Physics of fluids*, vol. 31, no. 12, pp. 3532–3542, 1988.

[109] M. Gharib, E. Rambod, and K. Shariff, "A universal time scale for vortex ring formation," *Journal of Fluid Mech.*, vol. 360, pp. 121–140, 1998.

[110] N. Didden, "On the formation of vortex rings: rolling-up and production of circulation," *Journal of Applied Mathematics and Physics (ZAMP)*, vol. 30, pp. 101–116, 1979.

[111] M. Nitsche and R. Krasny, "A numerical study of vortex ring formation at the edge of a circular tube," *J. Fluid Mech.*, vol. 276, pp. 139–161, 1994.

[112] S. James and C. Madnia, "Direct numerical simulation of a laminar vortex ring," *Physics of Fluids*, vol. 8, no. 9, pp. 2400–2414, 1996.

[113] M. H. I. Baird, "Velocity and momentum of vortex rings in relation to formation parameters," *The Canadian Journal of Chemical Engineering*, vol. 55, pp. 19–26, 1977.

[114] P. G. Saffman, "The velocity of viscous vortex rings," *Studies in Applied Mathematics*, vol. 49, pp. 371–380, 1970.

[115] H. Lamb, *Hydrodynamics*. Cambridge university press, 1932.

[116] Y. Fukumoto and H. Moffatt, "Motion and expansion of a viscous vortex ring. part 1. a higher-order asymptotic formula for the velocity," *Journal of Fluid Mechanics*, vol. 417, pp. 1–45, 2000.

[117] A. Anderson, "Structure and velocity of the periodic vortex-ring pattern of a primary pfeifenton (pipe tone) jet," *The Journal of the Acoustic Society of America*, vol. 27, pp. 1048–1053, 1955.

[118] E. Aydemir, N. A. Worth, and J. R. Dawson, "The formation of vortex rings in a strongly forced jet," *Exp. Fluids*, vol. 52, pp. 729–742, 2012.

[119] P. S. Krueger, "Vortex ring velocity and minimum separation in an infinite train of vortex rings generated by a fully pulsed jet," *Theor. Comput. Fluid Dyn.*, vol. 24, pp. 291–297, 2010.

[120] C. Schram and M. L. Riethmuller, "Measurement of vortex ring characteristics during pairing in a forced subsonic air jet," *Experiments in Fluids*, vol. 33, pp. 879–888, 2002.

[121] K. Zaman and A. Hussain, "Vortex pairing in a circular jet under controlled excitation. part 1. general jet response," *Journal of fluid mechanics*, vol. 101, no. 3, pp. 449–491, 1980.

[122] M. Krieg and K. Mohseni, "Thrust characterization of a bioinspired vortex ring thruster for locomotion of underwater robots," *IEEE Journal of Oceanic Engineering*, vol. 33, pp. 123–132, 2008.

[123] H. K. Moffatt, "The degree of knottedness of tangled vortex lines," *Journal of Fluid Mechanics*, vol. 35, no. 1, pp. 117–129, 1969.

[124] J. Allen and B. Auvity, "Interaction of a vortex ring with a piston vortex," *Journal of Fluid Mechanics*, vol. 465, pp. 353–378, 2002.

[125] P. Saffman, "The number of waves on unstable vortex rings," *Journal of Fluid Mechanics*, vol. 84, no. 4, pp. 625–639, 1978.

[126] J. Lawson and J. Dawson, "The formation of turbulent vortex rings by synthetic jets," *Physics of Fluids*, vol. 25, no. 10, p. 105113, 2013.

[127] K. Schlueter-Kuck and J. O. Dabiri, "Pressure evolution in the shear layer of forming vortex rings," *Physical Review Fluids*, vol. 1, no. 1, p. 012501, 2016.

[128] T. Maxworthy, "Some experimental studies of vortex rings," *Journal of Fluid Mechanics*, vol. 81, no. 3, pp. 465–495, 1977.

[129] S. S. Virani, A. Alonso, H. J. Aparicio, E. J. Benjamin, M. S. Bittencourt, C. W. Callaway, A. P. Carson, A. M. Chamberlain, S. Cheng, F. N. Delling, *et al.*, "Heart disease and stroke statistics—2021 update: a report from the american heart association," *Circulation*, vol. 143, no. 8, pp. e254–e743, 2021.

[130] S. J. Head, M. Çelik, and A. P. Kappetein, "Mechanical versus bioprosthetic aortic valve replacement," *European Heart Journal*, vol. 38, pp. 2183–2191, 04 2017.

[131] R. Diaz, D. Hernandez-Vaquero, R. Alvarez-Cabo, P. Avanzas, J. Silva, C. Moris, and I. Pascual, "Long-term outcomes of mechanical versus biological aortic valve prosthesis: Systematic review and meta-analysis," *The Journal of Thoracic and Cardiovascular Surgery*, vol. 158, no. 3, pp. 706–714.e18, 2019.

[132] J. Sheriff, D. Bluestein, G. Girdhar, and J. Jesty, "High-shear stress sensitizes platelets to subsequent low-shear conditions," *Annals of biomedical engineering*, vol. 38, no. 4, pp. 1442–1450, 2010.

[133] A. Kheradvar, E. M. Groves, A. Falahatpisheh, M. K. Mofrad, S. H. Alavi, R. Tranquillo, L. P. Dasi, C. A. Simmons, K. J. Grande-Allen, C. J. Goergen, *et al.*, "Emerging trends in heart valve engineering: Part iv. computational modeling and experimental studies," *Annals of biomedical engineering*, vol. 43, no. 10, pp. 2314–2333, 2015.

[134] I. Borazjani, "A review of fluid-structure interaction simulations of prosthetic heart valves," *Journal of long-term effects of medical implants*, vol. 25, no. 1-2, 2015.

[135] M. Hedayat, H. Asgharzadeh, and I. Borazjani, "Platelet activation of mechanical versus bioprosthetic heart valves during systole," *Journal of biomechanics*, vol. 56, pp. 111–116, 2017.

[136] M. Hedayat and I. Borazjani, "Comparison of platelet activation through hinge vs bulk flow in bileaflet mechanical heart valves," *Journal of biomechanics*, vol. 83, pp. 280–290, 2019.

[137] Q. Li, F. Hegner, and C. H. Bruecker, "Comparative study of wall-shear stress at the ascending aorta for different mechanical heart valve prostheses," *Journal of biomechanical engineering*, vol. 142, no. 1, 2020.

[138] S. S. Abbas, M. S. Nasif, and R. Al-Waked, "State-of-the-art numerical fluid–structure interaction methods for aortic and mitral heart valves simulations: A review," *Simulation*, vol. 98, no. 1, pp. 3–34, 2022.

[139] B. R. Travis, H. L. Leo, P. A. Shah, D. H. Frakes, and A. P. Yoganathan, "An analysis of turbulent shear stresses in leakage flow through a bileaflet mechanical prostheses," *J. Biomech. Eng.*, vol. 124, no. 2, pp. 155–165, 2002.

[140] H. Mächler, M. Perthel, G. Reiter, U. Reiter, M. Zink, P. Bergmann, A. Waltensdorfer, and J. Laas, "Influence of bileafletprosthetic mitral valve orientation on left ventricular flow—an experimental in vivo magnetic resonance imagingstudy," *European journal of cardio-thoracic surgery*, vol. 26, no. 4, pp. 747–753, 2004.

[141] S. Annerel, T. Claessens, L. Taelman, J. Degroote, G. Van Nooten, P. Verdonck, P. Segers, and J. Vierendeels, "Influence of valve size, orientation and downstream geometry of an

aortic bmhv on leaflet motion and clinically used valve performance parameters," *Annals of biomedical engineering*, vol. 43, no. 6, pp. 1370–1384, 2015.

[142] S. S. Abbas, M. S. Nasif, M. A. M. Said, R. Al-Waked, and S. K. Kadhim, "Numerical investigation on effect of leaflet thickness on structural stresses developed in a bileaflet mechanical heart valve for its sustainable manufacturing," in *MATEC Web of Conferences*, vol. 131, p. 04004, EDP Sciences, 2017.

[143] S. S. Abbas, M. S. Nasif, M. A. M. Said, and R. Al-Waked, "Numerical simulation of the non-newtonian blood flow through aortic bileaflet mechanical heart valve using fluid-structure interaction approach," in *AIP Conference Proceedings*, vol. 2035, p. 070003, AIP Publishing LLC, 2018.

[144] P. Kleine, M. Perthel, H. Nygaard, S. B. Hansen, P. K. Paulsen, C. Riis, and J. Laas, "Medtronic hall versus st. jude medical mechanical aortic valve: Downstream turbulences with respect to rotation in pigs," *J. Heart Valve Dis.*, vol. 7, no. 5, pp. 548–555, 1998.

[145] P. Kleine, M. Scherer, U. Abdel-Rahman, A. A. Klesius, H. Ackermann, and A. Moritz, "Effect of mechanical aortic valve orientation on coronary artery flow: comparison of tilting disc versus bileaflet prostheses in pigs," *The Journal of Thoracic and Cardiovascular Surgery*, vol. 124, no. 5, pp. 925–932, 2002.

[146] T. Akutsu, J. Saito, R. Imai, T. Suzuki, and X. D. Cao, "Dynamic particle image velocimetry study of the aortic flow field of contemporary mechanical bileaflet prostheses," *Journal of Artificial Organs*, vol. 11, no. 2, pp. 75–90, 2008.

[147] T. Akutsu, A. Matsumoto, and K. Takahashi, "In vitro study of the correlation between the aortic flow field affected by the bileaflet mechanical valves and coronary circulation," in *5th European Conference of the International Federation for Medical and Biological Engineering*, pp. 769–772, Springer, 2011.

[148] L. Haya and S. Tavoularis, "Effects of bileaflet mechanical heart valve orientation on fluid stresses and coronary flow," *Journal of Fluid Mechanics*, vol. 806, p. 129, 2016.

[149] D. de Ze´ licourt, K. Pekkan, H. Kitajima, D. Frakes, and, and A. P. Yoganathan, "Single-step stereolithography of complex anatomical models for optical flow measurements," *J. Biomech. Eng.*, vol. 127, no. 1, pp. 204–207, 2005.

[150] S. Pirola, Z. Cheng, O. Jarral, D. O'Regan, J. Pepper, T. Athanasiou, and X. Xu, "On the choice of outlet boundary conditions for patient-specific analysis of aortic flow using computational fluid dynamics," *Journal of biomechanics*, vol. 60, pp. 15–21, 2017.

[151] F. Domenichini, G. Pedrizzetti, and B. Baccani, "Three-dimensional filling flow into a model left ventricle," *Journal of Fluid Mechanics*, vol. 539, p. 179, 2005.

[152] F. Domenichini and G. Pedrizzetti, "Intraventricular vortex flow changes in the infarcted left ventricle: numerical results in an idealised 3d shape," *Computer methods in biomechanics and biomedical engineering*, vol. 14, no. 01, pp. 95–101, 2011.

[153] J. Mangual, F. Domenichini, and G. Pedrizzetti, "Describing the highly three dimensional right ventricle flow," *Annals of biomedical engineering*, vol. 40, no. 8, pp. 1790–1801, 2012.

[154] V. C. Rideout, *Mathematical and computer modeling of physiological systems*. Prentice Hall Englewood Cliffs, NJ:, 1991.

[155] S. Port, F. R. Cobb, R. E. Coleman, and R. H. Jones, "Effect of age on the response of the left ventricular ejection fraction to exercise," *New England Journal of Medicine*, vol. 303, no. 20, pp. 1133–1137, 1980.

[156] A. M. Weissler, W. S. Harris, and C. D. Schoenfeld, "Systolic time intervals in heart failure in man," *Circulation*, vol. 37, no. 2, pp. 149–159, 1968.

[157] A. M. Bavo, A. M. Pouch, J. Degroote, J. Vierendeels, J. H. Gorman, R. C. Gorman, and P. Segers, "Patient-specific cfd simulation of intraventricular haemodynamics based on 3d ultrasound imaging," *Biomedical engineering online*, vol. 15, no. 1, pp. 1–15, 2016.

[158] L. P. Dasi, H. A. Simon, P. Sucosky, and A. P. Yoganathan, "Fluid mechanics of artificial heart valves," *Clinical and experimental pharmacology and physiology*, vol. 36, no. 2, pp. 225–237, 2009.

[159] L. Dasi, L. Ge, H. Simon, F. Sotiropoulos, and A. Yoganathan, "Vorticity dynamics of a bileaflet mechanical heart valve in an axisymmetric aorta," *Physics of Fluids*, vol. 19, no. 6, p. 067105, 2007.

[160] T. B. Le and F. Sotiropoulos, "Fluid–structure interaction of an aortic heart valve prosthesis driven by an animated anatomic left ventricle," *Journal of computational physics*, vol. 244, pp. 41–62, 2013.

[161] J. Apel, R. Paul, S. Klaus, T. Siess, and H. Reul, "Assessment of hemolysis related quantities in a microaxial blood pump by computational fluid dynamics," *Artificial organs*, vol. 25, no. 5, pp. 341–347, 2001.

[162] D. Bluestein, L. Niu, R. T. Schoephoerster, and M. K. Dewanjee, "Fluid mechanics of arterial stenosis: relationship to the development of mural thrombus," *Annals of biomedical engineering*, vol. 25, no. 2, p. 344, 1997.

[163] J. S. Soares, J. Sheriff, and D. Bluestein, "A novel mathematical model of activation and sensitization of platelets subjected to dynamic stress histories," *Biomechanics and modeling in mechanobiology*, vol. 12, no. 6, pp. 1127–1141, 2013.

[164] P. Allen and R. Robertson, "The significance of intermittent regurgitation in aortic valve prostheses," *The Journal of thoracic and cardiovascular surgery*, vol. 54, no. 4, pp. 549–552, 1967.

[165] U. Gülan and M. Holzner, "The influence of bileaflet prosthetic aortic valve orientation on the blood flow patterns in the ascending aorta," *Medical engineering & physics*, vol. 60, pp. 61–69, 2018.

[166] M. Daghooghi and I. Borazjani, "A kinematics-based model for the settling of gravity-driven arbitrary-shaped particles on a surface," *Plos one*, vol. 16, no. 2, p. e0243716, 2021.

[167] D. Perić and D. Owen, "Computational model for 3-d contact problems with friction based on the penalty method," *International journal for numerical methods in engineering*, vol. 35, no. 6, pp. 1289–1309, 1992.

[168] T. A. Laursen, *Computational contact and impact mechanics: fundamentals of modeling interfacial phenomena in nonlinear finite element analysis*. Springer Science & Business Media, 2013.

[169] N. J. Carpenter, R. L. Taylor, and M. G. Katona, "Lagrange constraints for transient finite element surface contact," *International journal for numerical methods in engineering*, vol. 32, no. 1, pp. 103–128, 1991.

[170] T. Belytschko and M. O. Neal, "Contact-impact by the pinball algorithm with penalty and lagrangian methods," *International Journal for Numerical Methods in Engineering*, vol. 31, no. 3, pp. 547–572, 1991.

[171] R. C. Fetecau, J. E. Marsden, M. Ortiz, and M. West, "Nonsmooth lagrangian mechanics and variational collision integrators," *SIAM Journal on Applied Dynamical Systems*, vol. 2, no. 3, pp. 381–416, 2003.

[172] C. Martin and W. Sun, "Simulation of long-term fatigue damage in bioprosthetic heart valves: effects of leaflet and stent elastic properties," *Biomechanics and modeling in mechanobiology*, vol. 13, no. 4, pp. 759–770, 2014.

[173] R. Haj-Ali, L. P. Dasi, H.-S. Kim, J. Choi, H. Leo, and A. P. Yoganathan, "Structural simulations of prosthetic tri-leaflet aortic heart valves," *Journal of biomechanics*, vol. 41, no. 7, pp. 1510–1519, 2008.

[174] R. Gnyaneshwar, R. K. Kumar, and K. R. Balakrishnan, "Dynamic analysis of the aortic valve using a finite element model," *The Annals of thoracic surgery*, vol. 73, no. 4, pp. 1122–1129, 2002.

[175] K. H. Lim, J. H. Yeo, and C. Duran, "Three-dimensional asymmetrical modeling of the mitral valve: a finite element study with dynamic boundaries," *J Heart Valve Dis*, vol. 14, no. 3, pp. 386–392, 2005.

[176] E. Patterson, I. Howard, and M. Thornton, "A comparative study of linear and nonlinear simulations of the leaflets in a bioprosthetic heart valve during the cardiac cycle," *Journal of medical engineering & technology*, vol. 20, no. 3, pp. 95–108, 1996.

[177] G. Burriesci, I. Howard, and E. Patterson, "Influence of anisotropy on the mechanical behaviour of bioprosthetic heart valves," *Journal of medical engineering & technology*, vol. 23, no. 6, pp. 203–215, 1999.

[178] N. J. Driessen, A. Mol, C. V. Bouten, and F. P. Baaijens, "Modeling the mechanics of tissue-engineered human heart valve leaflets," *Journal of biomechanics*, vol. 40, no. 2, pp. 325–334, 2007.

[179] H. Kim, J. Lu, M. S. Sacks, and K. B. Chandran, "Dynamic simulation pericardial bioprosthetic heart valve function," 2006.

[180] A. Cataloglu, R. E. Clark, and P. L. Gould, "Stress analysis of aortic valve leaflets with smoothed geometrical data," *Journal of Biomechanics*, vol. 10, no. 3, pp. 153–158, 1977.

[181] M. Black, I. Howard, X. Huang, and E. Patterson, "A three-dimensional analysis of a bioprosthetic heart valve," *Journal of Biomechanics*, vol. 24, no. 9, pp. 793–801, 1991.

[182] A. K. Iyengar, H. Sugimoto, D. B. Smith, and M. S. Sacks, "Dynamic in vitro quantification of bioprosthetic heart valve leaflet motion using structured light projection," *Annals of biomedical engineering*, vol. 29, no. 11, pp. 963–973, 2001.

[183] A. Mirnajafi, J. Raymer, M. J. Scott, and M. S. Sacks, "The effects of collagen fiber orientation on the flexural properties of pericardial heterograft biomaterials," *Biomaterials*, vol. 26, no. 7, pp. 795–804, 2005.

[184] A. M. Bavo, G. Rocatello, F. Iannaccone, J. Degroote, J. Vierendeels, and P. Segers, "Fluid-structure interaction simulation of prosthetic aortic valves: comparison between immersed boundary and arbitrary lagrangian-eulerian techniques for the mesh representation," *PloS one*, vol. 11, no. 4, p. e0154517, 2016.

[185] J. Donea, S. Giuliani, and J.-P. Halleux, "An arbitrary lagrangian-eulerian finite element method for transient dynamic fluid-structure interactions," *Computer methods in applied mechanics and engineering*, vol. 33, no. 1-3, pp. 689–723, 1982.

[186] T. Ye, R. Mittal, H. Udaykumar, and W. Shyy, "An accurate cartesian grid method for viscous incompressible flows with complex immersed boundaries," *Journal of computational physics*, vol. 156, no. 2, pp. 209–240, 1999.

[187] Y. Chen and H. Luo, "Pressure distribution over the leaflets and effect of bending stiffness on fluid–structure interaction of the aortic valve," *Journal of Fluid Mechanics*, vol. 883, 2020.

[188] A. Gilmanov, T. B. Le, and F. Sotiropoulos, "A numerical approach for simulating fluid structure interaction of flexible thin shells undergoing arbitrarily large deformations in complex domains," *Journal of computational physics*, vol. 300, pp. 814–843, 2015.

[189] M.-C. Hsu, D. Kamensky, F. Xu, J. Kiendl, C. Wang, M. C. Wu, J. Mineroff, A. Reali, Y. Bazilevs, and M. S. Sacks, "Dynamic and fluid–structure interaction simulations of bioprosthetic heart valves using parametric design with t-splines and fung-type material models," *Computational mechanics*, vol. 55, no. 6, pp. 1211–1225, 2015.

[190] C. Carmody, G. Burriesci, I. Howard, and E. Patterson, "An approach to the simulation of fluid–structure interaction in the aortic valve," *Journal of biomechanics*, vol. 39, no. 1, pp. 158–169, 2006.

[191] R. G. Leyh, C. Schmidtke, H.-H. Sievers, and M. H. Yacoub, "Opening and closing characteristics of the aortic valve after different types of valve-preserving surgery," *Circulation*, vol. 100, no. 21, pp. 2153–2160, 1999.

[192] W. Mao, K. Li, and W. Sun, "Fluid–structure interaction study of transcatheter aortic valve dynamics using smoothed particle hydrodynamics," *Cardiovascular engineering and technology*, vol. 7, no. 4, pp. 374–388, 2016.

[193] D. Hasler and D. Obrist, "Three-dimensional flow structures past a bio-prosthetic valve in an in-vitro model of the aortic root," *PloS one*, vol. 13, no. 3, p. e0194384, 2018.

[194] M. Thubrikar, J. Heckman, and S. Nolan, "High speed cine-radiographic study of aortic valve leaflet motion.," *The Journal of heart valve disease*, vol. 2, no. 6, pp. 653–661, 1993.

[195] R. Fries, T. Graeter, D. Aicher, H. Reul, C. Schmitz, M. Böhm, and H.-J. Schäfers, "In vitro comparison of aortic valve movement after valve-preserving aortic replacement," *The Journal of Thoracic and Cardiovascular Surgery*, vol. 132, no. 1, pp. 32–37, 2006.

[196] S. Koshigoe, E. Gutmark, K. C. Schadow, and A. Tubis, "Initial development of noncircular jets leading to axis switching," *AIAA journal*, vol. 27, no. 4, pp. 411–419, 1989.

[197] E. J. Gutmark and F. F. Grinstein, "Flow control with noncircular jets," *Annual review of fluid mechanics*, vol. 31, no. 1, pp. 239–272, 1999.

[198] A. Yousefi, D. L. Bark, and L. P. Dasi, "Effect of arched leaflets and stent profile on the hemodynamics of tri-leaflet flexible polymeric heart valves," *Annals of biomedical engineering*, vol. 45, no. 2, pp. 464–475, 2017.

[199] T. New and D. Tsovolos, "Vortex behaviour and velocity characteristics of jets issuing from hybrid inclined elliptic nozzles," *Flow, turbulence and combustion*, vol. 89, no. 4, pp. 601–625, 2012.

[200] M. Grigioni, U. Morbiducci, G. D'Avenio, G. Di Benedetto, and C. Del Gaudio, "A novel formulation for blood trauma prediction by a modified power-law mathematical model," *Biomechanics and Modeling in Mechanobiology*, vol. 4, no. 4, pp. 249–260, 2005.

[201] J. Sheriff, J. S. Soares, M. Xenos, J. Jesty, and D. Bluestein, "Evaluation of shear-induced platelet activation models under constant and dynamic shear stress loading conditions relevant to devices," *Annals of biomedical engineering*, vol. 41, no. 6, pp. 1279–1296, 2013.